1

Eingereicht am: 09 Juni 2005

Thermodynamic Characterization of Heavy Fermion Systems and Low Dimensional Quantum Magnets Near a Quantum Critical Point

DISSERTATION

zur Erlangung des akademischen Grades

Doctor rerum naturalium

(Dr. rer. nat.)

genehmigt

durch die Fakultät Mathematik und Naturwissenschaften

der Technischen Universität Dresden

von

Maria Teodora Radu

geboren am 04.09.1976 in Tirlisua / Rumänien

Max-Planck-Institut für Chemische Physik fester Stoffe, Dresden 2005

Contents

1 Introduction

The standard model of conduction electrons in metals presumes that the interaction among electrons can be described by a few parameters such as the effective mass, which differs from the free-electron mass. This renormalisation leads to effectively independent quasiparticles that can be treated within the framework of Landau-Fermi-liquid (LFL) theory. Even heavy-fermion (HF) systems - metals with a high concentration of rare–earth or actinide elements such as Ce, Yb, or U - can be regarded as LFLs. The strong interactions between electrons in these materials lead to a very large effective mass, derived from the huge linear specific-heat coefficient $\gamma = C/T$, and a correspondingly large Pauli susceptibility χ, with $C/T \sim \chi = const$ at sufficiently low temperatures T. However, a wide body of measurements suggests that the LFL description fails when a system is tuned to a zero–temperature magnetic instability, or "quantum–critical–point" (QCP). Here, strong quantum fluctuations develop in the magnetization which influence the quasiparticle excitation spectrum. It is believed that these fluctuations even affect the normal–state properties of high–temperature superconductors which explains the current interest in quantum critical behavior.

Strong correlations between electrons (e.g., the interaction of conduction electrons with almost localised magnetic moments of 4f and 5f elements) can cause a number of outstanding and exciting low–temperature features like unconventional superconductivity ("HF superconductivity"), insulating ground states ("Kondo insulator"), intermediate valence or magnetic ordering with significantly reduced magnetic moments.

The overwhelming number of these phenomena is found in Ce-, Yb- and U–based

compounds and alloys and may be referred to instabilities of the electronic configuration in the ground state. The principal interaction in such systems is, beside the Ruderman–Kittel–Kasuya–Yosida (RKKY) interaction, the Kondo effect which tends to quench the local magnetic moments. For temperatures well below a characteristic temperature of the system (the "Kondo temperature", T_K) the physical properties can successfully be accounted for in terms of the LFL model.

A number of control parameters like alloying, pressure, or magnetic field allows the relevant interactions and thus the ground state of such systems to be changed. A variation of the hybridization strength J between the f and the conduction electrons can drive the system from a magnetic towards a non-magnetic state, thereby passing a critical value of J where long–range magnetic order is just suppressed to zero. At that critical value of the parameter J, pronounced deviations from predictions of the LFL behaviour occur. The most prominent are a logarithmic temperature dependence of the specific heat and deviations of the temperature–dependent resistivity from a quadratic power law. One refers to these deviations as non–Fermi–liquid behaviour (NFL).

Two different theoretical models have been proposed to describe the NFL properties: a spin–density–wave (SDW) and a localized–moment (LM) scenario. In the former model magnetism develops by the spin polarization of the Fermi surface. NFL behavior results from the scattering of electrons off quantum–critical spin fluctuations in the magnetization. The latter model explicitly takes into account that the heavy quasiparticle is a composite bound state formed between the local magnetic moments and the conduction electrons via the Kondo effect. At the QCP the quasiparticle will disintegrate into its localized spin and delocalized charge degrees of freedom. This break up of the heavy electrons is responsible for the NFL behavior.

It is also worth noting that the dimensionality of the critical spin fluctuations plays an important role in NFL behavior. Different behaviours in thermodynamic and transport properties have been postulated in the case of two–dimensional (2D) or three–dimensional (3D) spin fluctuations. Throughout the variety of compounds showing NFL behaviour in the vicinity of a magnetic QCP most of them have either tetrago-

nal or orthorhombic structure, hence an intrinsic crystalline anisotropy. The absence of crystalline anisotropy in cubic structures avoids a preferential orientation of the spin fluctuations. Therefore, thermodynamic experiments on cubic systems might shed light on the correlation between the symmetry of the crystal lattice, the dimensionality of the fluctuations and the nature of the QCP. Presently, no specific–heat experiments on a cubic system in the vicinity of the QCP have been reported. In this context $CeIn_{3-x}Sn_x$ provides a cubic reference material for investigation of the QCP.

In order to approach the QCP in HF compounds, we used chemical substitution as well as magnetic field. The latter method is of particular interest as it allows one to fine tune the system continuously and hence, to follow the evolution from NFL to LFL behavior in great detail.

In low–dimensional spin systems the critical behavior related to the suppression of the magnetic order with magnetic field is also a subject of profound theoretical and experimental research. One of the most striking effects is the dependence of magnetic properties of quasi–one–dimensional antiferromagnets with anisotropic exchange interactions on the direction of the applied magnetic field. The basic model of such type of magnets is the anisotropic Heisenberg chain, the so–called XXZ model. It is therefore important to study the dependence of the properties of the XXZ chain on the field direction. There are two studied cases of the field direction. The first is the XXZ model in the uniform longitudinal magnetic field (along the Z axis) where the longitudinal field commutes with the XXZ Hamiltonian. In this case the model is exactly solved by the Bethe ansatz and has been studied in great details [1]. In the second case the field is applied in the transverse direction and the exact integrability is lost. Thus, the behavior of the XXZ model in the symmetry–breaking transverse field (noncommuting field) [2] is essentially different from the case of the longitudinal field applied along the anisotropy axis. In particular, such noncommuting terms introduce quantum fluctuations into the zero–temperature ground state which, for large enough fields, can completely disorder the system. Such a scenario has been observed in the three–dimensional Ising ferromagnet $LiHoF_4$ [3]. Nevertheless, due to its high dimensionality, the system behaves in a

mean–field–like way. In this work we consider a quasi–one–dimensional antiferromagnet, Cs_2CoCl_4, and the effects of noncommuting applied field on its ground state. Neutron–scattering measurements [4] suggested that in high fields a transition occurs to a phase with no long–range order proposed to be a spin–liquid phase with a finite fluctuating spin moment. This opens the possibility to check experimentally the existence of a spin–liquid state, proposed long time ago theoretically but not observed experimentally up to now.

Spins in frustrated geometries are believed to behave in much more unconventional ways. Frustration increases the degeneracy of the ground state, giving rise to large phase space for fluctuations. Low dimensionality and frustration lead to unique phase diagrams with multicritical points and novel critical phenomena. In particular, spin–1/2 AFM triangular–lattice systems present a good example for investigating fully the quantum–mechanical effects of frustration. Cs_2CuCl_4 is a quasi–two–dimensional spin–1/2 AFM on a frustrated triangular lattice so that the quantum fluctuations are strong and also enhanced by the low dimensionality. In a quantum AFM a fully spin–polarized state can be reached at high magnetic field B exceeding a saturation field B_c. In this state spin excitations are gapped FM magnons. With decreasing B and passing through B_c, an AFM long–range order of the transverse spin component develops. Provided the symmetry of the spin Hamiltonian is such that the rotational invariance around the applied field is preserved, the transverse spin–component ordering can be regarded as a Bose–Einstein condensation (BEC) in a dilute gas of magnons. The theoretical concept of the magnon Bose–Einstein condensation (BEC) was introduced in [5] and developed further by several authors [6, 7]. This concept has been applied successfully to explain the field–induced magnetic ordering near the first critical field B_{c1}, $B \geq B_{c1} \simeq 5.4$ T in the Heisenberg AFM $TlCuCl_3$ [8, 9, 10]. In this compound the spins 1/2 form a network of weakly coupled dimers having an excitation gap Δ between the singlet ground state and the triplet excited state. An applied magnetic field B leads to a Zeeman splitting of the triplet states with the lowest mode crossing the ground state at the first critical field $B_{c1} = \Delta/g\mu_B$. The ground state for $B > B_{c1}$ is regarded to be a Bose-Einstein

condensate of this bosonic mode. There is a second critical field, the saturation field $B_{c2} = B_{sat}$, near which the magnon BEC transition is also expected. In TlCuCl$_3$, like in most of the other AFMs, the saturation field is rather high ($B_{sat} \sim 100$ T) and cannot be achieved at present. An exceptionally low and easily accessible saturation field of $B_c \simeq 8.5$ T, however, is needed in the quantum spin–1/2 AFM Cs$_2$CuCl$_4$ system which is investigated here.

The critical phenomena presented so far show that the combination of magnetic field and low temperatures is necessary to obtain detailed information of the physics in the vicinity of the QCP. In order to achieve the required measurement conditions the first task was to develop a new set–up for measuring specific heat. This achievement is described in detail in this work. After a general introduction to the basic theories in Chapter 2, which serve for the analysis of the experimental results, Chapter 3 describes the experimental technique and the apparatus used. The experimental results related to the issue of 2D and 3D fluctuations in the HF alloys YbRh$_2$(Si$_{0.95}$Ge$_{0.05}$)$_2$, Yb$_{1-y}$La$_y$Rh$_2$Si$_2$ ($y = 0.05, 0.1$), YbIr$_2$Si$_2$, and CeIn$_{3-x}$Sn$_x$, respectively are presented in Chapter 4. Chapter 5 deals with the low–dimensional spin systems Cs$_2$CuCl$_4$ and Cs$_2$CoCl$_4$ with special emphasis on the field–induced suppression of the AFM order. The obtained $B - T$ phase diagrams are presented and discussed as well. Finally, concluding remarks are given in Chapter 6.

2 Theoretical concepts

In this chapter, some basic theoretical concepts are presented which are related to the experimental results shown in chapter 4 and 5.

2.1 Specific heat

In thermodynamics, the specific heat of a system depends on the temperature at which it is measured, and on the changes that are allowed to take place during the rise of temperature. If the quantities $P, V, ...$ (P: pressure, V: volume), are held constant when a heat input δQ changes the temperature of a unit mass of the substance by δT, then

$$C_{P,V,..} = \lim_{\delta T \to 0} (\frac{\delta Q}{\delta T})_{P,V,..} \tag{2.1}$$

Generally, during the measurement of specific heat the pressure is kept constant ($P \cong 0$, hence the sample is in vacuum during the measurement) and only C_V is of importance. While thermodynamics is powerful in specifying the general laws governing a phenomenon it does not give any clue about the detailed behavior. To explain a variety of effects observed in the behavior of specific heats statistical mechanics is needed. The specific heat at constant volume can be written in terms of the free energy, F,

$$C_V = T \left(\frac{\partial^2 F}{\partial T^2} \right)_V , \tag{2.2}$$

with $F(T,V) = E - TS = -k_B T \cdot \ln Z$, where E is the energy of the quasiparticles, S is the entropy, k_B the Boltzmann constant, and Z the partition function which for a

canonical system, with g_n the degenerancy of the energy levels E_n, is

$$Z = \sum_n g_n E_n e^{-\frac{E_n}{k_B T}}. \tag{2.3}$$

In quantum statistical mechanics, the specific heat is given by

$$C_V = \frac{\partial}{\partial T} \int_0^\infty E \cdot D(E) \cdot f(E, T) \, dE, \tag{2.4}$$

with $D(E)$ the density of states and $f(E, T)$ the distribution function,

$$f(E, T) = \frac{1}{e^{-\frac{E-\mu}{k_B T}} \pm 1}, \tag{2.5}$$

with "+" for a Fermi-Dirac distribution (fermions) "−" for a Bose-Einstein distribution (bosons).

2.2 Contributions to the specific heat in solids

At low temperatures there are different contributions to the specific heat which are described here.

2.2.1 Phonons and electrons

The contribution of the phonons to the specific heat of a crystal is called the lattice specific heat. The thermal energy of the crystal lattice may be written as the sum of the energies over all phonons modes which describe the oscillation state of the crystal. Because the angular frequencies of the lattice oscillators are spaced very closely, one can replace the sum by an integration, obtaining the specific heat eq. (2.4). The density of states, $D(\omega)$ can be calculated using the Debye approximation [11, 12]. Here the Debye temperature is defined as, $\hbar\omega_D = k_B\theta_D$ with ω_D (Debye boundary frequency), the frequency above which there is no oscillation state. At low temperatures, $T < \theta_D/10$, one obtains the T^3–Debye law,

$$C_V = \frac{12}{4}\pi^4 R(\frac{T}{\theta_D})^3 \simeq 1944(\frac{T}{\theta_D})^3 \text{J/molK}, \tag{2.6}$$

with the gas constant $R = 8.314$ J/molK. θ_D is a measure of the temperature below which the phonons begin to "freeze out".

The electronic contribution to the specific heat can be easily estimated quantitatively via eq. (2.4). The density of states for a 3D electron system is given by

$$D(E) = \frac{V}{2\pi}(\frac{2m}{\hbar^2})^{\frac{3}{2}}\sqrt{E_F}, \tag{2.7}$$

with m the electron mass and $\hbar = h/2\pi$, with h the Planck constant.

At the Fermi boundary, the derivative of the Fermi–Dirac distribution deviates considerably from zero. Therefore, it is a good approximation to calculate the density of states at E_F,

$$D(E_F) = \frac{3N}{2E_F} = \frac{3N}{2k_B T_F}. \tag{2.8}$$

Using the total number of electrons per unit cell, n_e, the electronic specific heat is obtained as

$$C_{el} = \frac{\pi^2}{2}n_e k_B(\frac{T}{T_F}) = \gamma T. \tag{2.9}$$

At very low temperatures, far below the Fermi and Debye temperature the specific heat for a metal can be written as

$$C = \gamma T + \beta T^3. \tag{2.10}$$

Usually, above about 4 K the lattice part dominates the specific heat, while below that temperature the electronic part remains significant.

2.2.2 Nuclear excitations

The orbiting $4f$ electrons in the rare earths (RE) can produce a large effective magnetic field, B_{eff} at the nucleus (several 100 T). In addition, other, but small, contributions from the Fermi contact term, the dipolar interactions and the orbital motion contribute to B_{eff} [13, 14].

The interaction between the effective magnetic field and the nuclear magnetic moment of the nucleus, $\vec{\mu} = g_N \mu_N \vec{I}$ (with μ_N the nuclear magneton, g_N a quantity corresponding

to the g-value (of order unity) and I the nuclear spin) and that between the quadrupole moment and the electric field gradient (EFG) are called the hyperfine interactions (hf). The hamiltonian for the hf is written as

$$\hat{H}_{hf} = aI_z + p[I_z^2 - \frac{1}{3}I(I+1)], \tag{2.11}$$

with

$$a = \frac{1}{k_B}\frac{\mu_I}{I}B_{eff} = \frac{1}{k_B}(\frac{\sigma}{2\pi})B_{eff}, \tag{2.12}$$

$$p = \frac{3\mid e\mid Q}{4I(2I-1)k_B}V'', \tag{2.13}$$

where a is the magnetic dipole and p the electric quadrupole parameter in units of K, I_z the z component of the nuclear spin I, and the z axis is taken along the ionic angular momentum $< J >$. The parameter σ is the gyromagnetic ratio. The values of $\sigma/(2\pi) = \nu_{NMR}$ are characteristic for each isotope. In the equation (2.13), e is the electronic charge, q the electric quadrupol moment at the nucleus, $V'' = eq$ the EFG present at the nucleus and Q the nuclear quadrupole moment. The eigenvalues of eq. (2.11) are,

$$\epsilon_m = am + p[m^2 - I(I+1)/3], \tag{2.14}$$

with m the eigenvalue of the operator I_z, which runs from $-I$ to $+I$. Without quadrupole interaction, i.e., $p = 0$, the energy levels are equally spaced. The magnetic dipole parameter varies as $< J_z >$ and p as $< 3J_z^2 - J(J+1) >$. For FM and AFM at low temperature $< J_z >= J$. Therefore, the magnetic–dipole parameter is proportional to J and $p \propto J(2J-1)$. Both parameters are temperature independent and are the only unknown parameters to fit the specific heat. Since the energy separation of the nuclear levels is very small, specific–heat measurements are often performed well above T_m, the maximum of the Schottky peak and detect only the high–temperature part of the Schottky anomaly, with $C_n = c_2T^{-2}$. The coefficient c_2 is obtained from an expansion of C_n in a power series for $T \ll T_m$

$$C_n = c_2T^{-2} + c_3T^{-3} + c_4T^{-4} + ..., \tag{2.15}$$

with the coefficients

$$c_2 = R(\frac{a^2}{3}I(I+1) + \frac{p^2}{45}I(I+1)(2I-1)(2I+3) \tag{2.16}$$

$$c_3 = -R(\frac{a^2}{15}pI(I+1)(2I-1)(2I+3) \tag{2.17}$$

$$c_4 = -R(\frac{a^4}{30}I(I+1)(2I^2+2I+1) \tag{2.18}$$

For the cubic symmetry and a perfectly spherically symmetrical nuclear–charge distribution $p = 0$. Otherwise, in zero field, the specific heat due to the nuclear quadrupolar splitting is $C_Q = \alpha_Q/T^2$, where α_Q is given by the term c_2 for $a = 0$ and isotopes with $I > 1/2$.

In an external magnetic field B, a Zeeman splitting of the nuclear levels occurs. This yields an additional α_Z term in the nuclear specific heat. Thus, the nuclear specific heat can be decomposed into a quadrupolar, α_Q and Zeeman part, α_Z:

$$C_{hf} = (\alpha_Q + \alpha_Z)/T^2. \tag{2.19}$$

In this notation it is convenient to write,

$$\alpha_Q = \frac{R}{3}(\frac{e^2qQ}{k_B})^2 \frac{(I+1)(2I+3)}{I(2I-1)} \tag{2.20}$$

$$\alpha_Z = 6.3835 \times 10^{-7} I(I+1)\nu_{NMR}^2 B_{eff}^2 \tag{2.21}$$

where ν_{NMR} is the NMR frequency–characteristic for each isotope in kHz/Gauss and B_{eff} in Tesla [15].

2.2.3 Spin waves

Similar to lattice vibrations, the spin–wave energies are quantized [12]. The basic unit is known as magnon and obeys Bose–Einstein statistics eq. (2.5).

The spin–wave theory gives the magnon dispersion relation, $\omega(k)$ for a three–dimensional ferromagnetic crystal at long wavelengths, $ka \ll 1$ [12],

$$\omega_k = \frac{2J_0Sa^2}{\hbar}k^2, \tag{2.22}$$

where J_0 is the nearest–neighbor exchange integral assumed to be constant, k the wave vector while a is the distance between the spins. Thus, for small deviations of the spin from the ground–state configuration, the spin–wave frequencies depend quadratically on the wave vector. In contrast to a FM, where the ground state is well–defined, for an AFM the situation is quite complicated. The complete antiparallel alignment of the spins is not even an eigenstate of the Hamiltonian [12] and the degeneracy complicates the situation still further. Despite this, the computations for AFM magnons have shown that, in the long–wavelength limit, the frequency of a magnon in an isotropic AFM varies linearly with k, so that spin–wave theory for a cubic crystal gives

$$\omega_k = F_a \frac{2J'Sa}{\hbar} k, \tag{2.23}$$

where J' is the magnitude of the exchange constant and F_a is a constant that depends on the details of the crystal structure.

Ferromagnetic magnons have a single polarization direction for each value of k. For the density of states one has

$$D(\omega) = \frac{V}{4\pi^2} \left(\frac{\hbar}{2JSa^2F_f}\right)^{3/2} \omega^{1/2}, \tag{2.24}$$

with ω given by eq. (2.22). Using eq. (2.4) one obtains

$$C_M = s_f R \left(\frac{k_b T}{2JS}\right)^{3/2} \tag{2.25}$$

for the heat capacity in zero field, where s_f is a quantity that depends on the type of lattice under consideration. Thus, at low temperatures, the magnon contribution to the specific heat is of the form $T^{3/2}$. Generalizing, for a FM, the gapless modes give a low–temperature heat capacity which is a power law and when the space dimension is D, $C(T)_{T \to 0} \propto T^{D/2}$ [16]. An energy gap, E_g, in the 3D spin–wave dispersion causes an exponential term to appear in the magnon specific heat, i.e.:

$$C_M \propto T^{3/2} \exp(-E_g/k_B T). \tag{2.26}$$

The calculations for an AFM follow the same steps as for the FM. The heat capacities of a $3D$ AFM may be expressed as:

$$C_M = s_a f R \left(\frac{k_B T}{2J'S}\right)^3, \tag{2.27}$$

where s_{af} is a constant that depends on the crystal structure and has been calculated for several types of lattice [11, 12]. Thus, the temperature dependence of the specific heat of a $3D$ AFM is quite distinct from that of a $3D$ FM and is of the same form as the low–temperature lattice specific heat in the Debye model. For this reason it is difficult to separate the lattice and magnetic term correctly. For AFM, too, when there is a gap in the magnon dispersion relation, eq. (2.27) is expanded by an exponential term:

$$C_M \propto T^3 \exp(-E_g/k_B T). \tag{2.28}$$

In the case when the space dimension is 2, the specific heat of the magnons becomes $C(T) \propto T^2$. Similar calculations for the one–dimensional case leads to

$$C \propto T. \tag{2.29}$$

Generalizing it, we can write for the low–temperature behavior for a gapless AFM, $C(T)_{T \to 0} \propto T^D$ [16].

2.2.4 Anisotropic XY model

The XY model is one of the basic models in the branch of statistical mechanics. Moreover, the 1D XY model can be exactly solved by the Bethe ansatz. We consider the anisotropic case of the XY model with the Hamiltonian given by

$$H = \sum_{j=1}^{N} J_x S_j^x S_{j+1}^x + J_y S_j^y S_{j+1}^y - h \sum_{j=1}^{N} S_j^z. \tag{2.30}$$

It can be diagonalized [17, 18] as

$$H = \sum_q \omega(q)(\eta_q^\dagger \eta_q - 1/2), \tag{2.31}$$

with

$$\omega(k) = [(t \cos k - h)^2 + \Delta^2 \sin^2 k]^{1/2}, \tag{2.32}$$

where

$$\Delta = \frac{J_x - J_y}{2}, \tag{2.33}$$

$$t = \frac{J_x + J_y}{2}, \tag{2.34}$$

and $h = g\mu_B B$. Here, $q = 2\pi n/N$, with n–integer and N is the number of sites. The free energy per site, $f = F/R$ is

$$f = -2T \int_0^\pi \frac{dk}{2\pi} \ln \cosh \frac{\omega(k)}{2T}. \tag{2.35}$$

The specific heat becomes [19]

$$C = -T\frac{\partial^2 f}{\partial T^2} = \frac{1}{2\pi} \int_0^\pi \frac{dk}{2\pi} \frac{\omega^2(k)}{\cosh^2 \frac{\omega(k)}{2\pi}}. \tag{2.36}$$

Assuming k_0 as the point at which $\omega(k)$ has a minimum in the interval $(0, \pi)$, and expanding eq. (2.32) around it, the specific heat becomes

$$C = \frac{2}{T^2} \int_{-\infty}^\infty \frac{dk}{2\pi} [\Delta_g^2 2D\Delta_g (k - k_0)^2 + O((k-k_0)^3)]e^{-\Delta_g/T - Dk^2/T} + O(e^{-2\Delta_g/T}), \tag{2.37}$$

with the defined real positive parameters $\Delta_g = \omega(k_0)$ and

$$D = \frac{1}{2}\frac{\partial^2 \omega(k)}{\partial k^2}k_0. \tag{2.38}$$

Rescaling k by $\sqrt{T/D}$ and calculating the integrals yields

$$C = \frac{\Delta_g^2}{\sqrt{\pi D}}\frac{e^{-\Delta_g/T}}{T^{3/2}}[1 + \frac{T}{\Delta_g} + O(\frac{T^{3/2}}{\Delta_g^{3/2}})] + O(e^{-2\Delta_g/T}). \tag{2.39}$$

If one reintroduces scattering between the excitations (as needed for the XXZ model in a transverse field) on the one hand, one can expect to possibly get another exponent for T. On the other hand, this $T^{3/2}$ temperature dependence could be quite robust. For example, for a Heisenberg-Ising chain (XXZ with anisotropy $|\Delta| > 1$) or for an XXZ chain in a longitudinal field above the critical field, the same temperature dependence of the specific heat can be recovered from the Bethe Ansatz [2].

2.3 The Fermi-liquid state

The low-temperature properties of most normal metals, i.e., non-magnetic and non-superconducting conductors, are qualitatively similar and can be well described by the

LFL theory [20]. By introducing the so-called 'quasiparticles', which illustrate the electrons 'dressed' by clouds of other excitations such as the lattice distortion and the magnetic spin fluctuation, the strongly interacting electron states can be mapped to the non-interacting states with a one-to-one correspondence. Since the quasiparticles only have a sufficiently long lifetime in the immediate vicinity of the Fermi surface ($\sim k_{\mathrm{B}}T \ll E_{\mathrm{F}}$), the concept of quasiparticles makes sense only in this region. In other words, the LFL theory is only valid for $T \ll T_F$.

Two factors are responsible for the long mean-free path of electron-electron collisions in strongly correlated electron systems:

(i) The Pauli exclusion principle severely reduces the phase space for scattering quasiparticles close to the Fermi surface.

(ii) Screening limits the range of Coulomb interaction to the order of a lattice spacing.

The main effect of the electronic interactions is to renormalize the effective mass m^* of the electrons. In simple metals, m^* is of the order of the bare-electron mass m_e, whereas in heavy-fermion systems m^* can reach values up to $10^3 \, m_e$ due to the strong interactions. According to LFL theory, one has

$$\frac{m^*}{m_e} = 1 + \frac{F_1^s}{3},\tag{2.40}$$

where F_1^s is a symmetric Landau parameter.

The thermodynamic and transport properties of a normal FL are shown to be directly related to the effective mass m^*. The following properties are predicted by LFL theory for $T \to 0$.

The density of states at the Fermi energy is given by

$$N(E_F) = \frac{m^* k_F}{\pi^2 \hbar^2}.\tag{2.41}$$

The temperature–independent Pauli susceptibility χ has the form

$$\chi = \frac{\mu_0 \mu_B^2 m^* k_F}{\pi^2 \hbar^2} \frac{1}{1 + F_0^a},\tag{2.42}$$

where F_0^a is the antisymmetric Landau parameter. In comparison with the case of a non-interacting Fermi gas, χ is enhanced by a factor of $m^*/m_e(1 + F_0^a)$.

The specific heat follows

$$\frac{C}{T} = \gamma = \frac{m^* k_F k_B^2}{3\hbar^2},$$

(2.43)

Therefore, the measurements of specific heat should provide direct information on the effective mass m^*. Stewart [21] has chosen $\gamma > 400$ mJ/mol K^2 to define a compound as heavy-fermion system.

2.4 Kondo effect and RKKY interaction

The Kondo effect describes the exchange interaction between a magnetic impurity (with a spin $\mathbf{S}$) and a conduction electron (with a spin $\mathbf{s}$), given by the Hamiltonian

$$H = -J\mathbf{S} \cdot \mathbf{s}.$$

(2.44)

For a negative coupling J, the impurity spin is completely compensated by conduction electrons at low temperature, leading to the formation of a Kondo singlet. As a result, the resistivity follows -ln(T/T_K). The binding energy of a Kondo singlet is determined by

$$k_B T_K \sim \frac{1}{N(E_F)} e^{-\frac{1}{JN(E_F)}}.$$

(2.45)

The HF compounds may be considered as a Kondo lattice composed of a periodic array of magnetic 'impurities'. The main features of a Kondo lattice at low temperature include: (i) As $T \to 0$, the γ coefficient of the specific heat and the magnetic susceptibility tend to constants, but with largely enhanced values; (ii) The scattering at low temperature develops coherently, resulting in a drop of resistivity. For $T \ll T_K$, $\rho = \rho_0 + AT^2$ with a large coefficient A, characterizing a FL behavior. In such a case, the compensation of the magnetic moments of the f electrons by the Kondo effect leads to a non-magnetic ground state. On the other hand, the f electrons can interact with each other via the conduction electrons, i.e., via the so-called Ruderman-Kittel-Kasuya-Yosida (RKKY) interaction. This interaction tends to form a magnetic state. The energy associated with the RKKY interaction is

$$k_B T_{RKKY} \sim J^2 N(E_F).$$

(2.46)
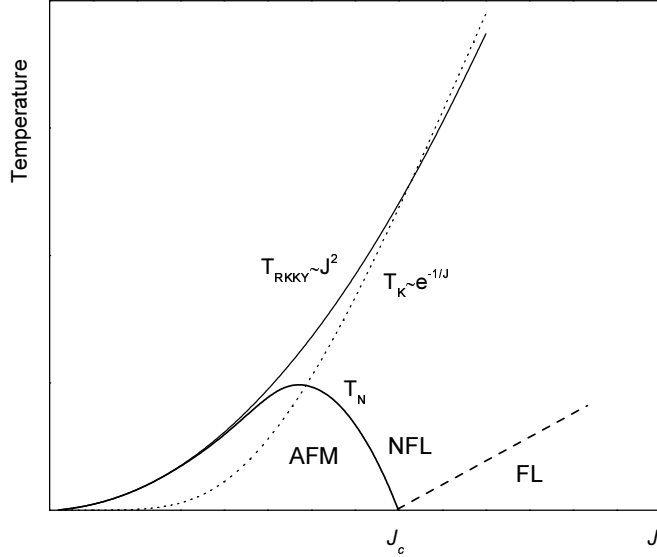
Figure 2.1: *Doniach phase diagram for antiferromagnetic heavy-fermion systems. For small J, $T_{RKKY} \gg T_K$ and the system orders antiferromagnetically below T_N. For large J, $T_{RKKY} \ll T_K$ and the ground state is non-magnetic.*

In the HF systems, the ground states are determined by the competition between the Kondo effect and the RKKY interaction (see the Doniach diagram in Fig. 2.1) [22]. When the RKKY interaction dominates (for small J), the system orders magnetically. When the Kondo interaction is stronger, the system is non-magnetic and usually follows the LFL theory at low temperatures. At the QCP, NFL behavior is usually observed (see next section). The coupling constant J can be tuned by pressure, chemical substitution or magnetic field.

2.5 Non-Fermi-liquid behavior

In recent years, NFL behavior has been widely observed in the HF systems, high-T_c superconductors, d–transition-metal compounds and one-dimensional (1D) systems (see, e.g. recent reviews [23, 24, 25]). The main features related to NFL behavior ($T \rightarrow 0$) include: (i) non-quadratic temperature dependence of the electrical resistivity ($\rho \sim T^n, n < 2$); (ii) strongly temperature–dependent specific-heat coeffi-

cient γ ($\gamma \sim -\log(T/T_0)$ or $\gamma \sim \gamma_0 - aT^{1/2}$); (iii) divergent magnetic susceptibility ($\chi \sim -\log(T/T_0)$ or $\chi \sim bT^{\beta}$). The divergence of the effective mass (γ) indicates that LFL theory breaks down in these situations. To understand these unusual physical properties, various theoretical models have been proposed: (1) scenario of quantum critical point; (2) multichannel Kondo model; (3) Kondo–disorder model; (4) the Griffiths–phase model and (5) the Luttinger–liquid model. In this section, we briefly overview the models which are considered to be relevant to the heavy-fermion systems investigated in this work.

2.5.1 The single-impurity multichannel Kondo model

The multichannel Kondo model for a single impurity, which was first introduced by Nozières and Blandin [26], can be described starting from the Hamiltonian:

$$H = \sum_{k,\sigma,m} \epsilon_k n_{k,\sigma,m} + J\mathbf{S} \cdot \sum_{i}^{m} \mathbf{s}_i, \qquad (2.47)$$

where $\mathbf{S}$ and $\mathbf{s}$ are the spin operators of the magnetic impurity and of the conduction electrons, respectively. The i labels the orbital channels or the degrees of freedom of conduction electrons. The spins of conduction electrons near the magnetic impurity are bound together to partially or completely compensate the impurity spins, which fall into the following three scenarios:

(1) $m = 2S$: The impurity spin is just compensated by the conduction-electron spins to form a singlet state. This gives rise to the normal Fermi-liquid behavior.

(2) $m < 2S$: The impurity spin is not fully compensated by the conduction electrons.

(3) $m > 2S$: In this case, the conduction-electron spins overcompensate the impurity spin and the magnetic ion can no longer make the usual non-magnetic singlet state. But the new magnetic state can still undergo further Kondo scattering. The resulting ground state bears no resemblance to the non-interacting gas of electrons and is a local non-Fermi-liquid.

The single-impurity multichannel Kondo model can be solved exactly and NFL behavior was found to exist only in the case of $m > 2S$. For the two-channel model

$(m = 2, S = 1/2)$, the specific-heat coefficient and the magnetic susceptibility diverge as $T \to 0$, following

$$\frac{C}{T} = -\frac{1}{T_K} \ln \frac{T}{b_1 T_K} \tag{2.48}$$

$$\chi \sim -\frac{1}{T_K} \ln \frac{T}{b_2 T_K}, \tag{2.49}$$

where b_1 and b_2 are constants. The electrical resistivity shows

$$\rho \sim \rho_0 - A(\frac{T}{T_K})^{1/2}. \tag{2.50}$$

It should be noted that, while the logarithmic divergence of C/T and χ appears for $T < 0.5T_K$, $\rho \sim -AT^{1/2}$ is observable only for $T < 0.05T_K$. In the intermediate temperature range, $\rho \sim -AT$.

2.5.2 Disordered Kondo model

As stated above, Fermi-liquid behavior is observed in the Kondo lattices for $T \ll T_K$, at which the impurity spin is screened by the conduction electrons. If some process takes place in a system to depress T_K, then the NFL behavior is extended to lower temperature. Disorder can play such a role. Since T_K is determined by the local-moment conduction-electron coupling J and the density of states $N(E_F)$ at the Fermi surface, disorder may cause a distribution of T_K. Averaging over such a distribution can produce thermodynamic and transport properties beyond the Fermi-liquid theory [27]. Essentially, the unquenched moments contribute to the NFL behavior. This model can interpret well the NMR results of $UCu_{5-x}Pd_x$ ($x = 1, 1.5$) [28], which exhibit a broad distribution of internal fields. Predictions for specific heat, susceptibility and resistivity are given by:

$$C/T \sim -\ln(T/T_0) \tag{2.51}$$

$$\chi \sim -\ln(T/T_0) \tag{2.52}$$

$$\rho = \rho_0 - AT. \tag{2.53}$$

2.5.3 Quantum critical-point theories

In the heavy-fermion compounds, NFL behavior usually occurs around a magnetic quantum critical point (QCP), at which the magnetic transition temperature is continuously tuned towards zero by an external parameter δ (e.g. pressure, magnetic field, or doping). Similar to the classic phase transition at a finite temperature, the quantum phase transition is also characterized by a divergent correlation length ξ and correlation time τ, but resulting from quantum fluctuations instead of thermal ones. A D-dimensional quantum system can be viewed as a $D + z$-dimensional classic system, where z is the dynamical critical exponent and takes a value of 2 for antiferromagnetic and 3 for ferromagnetic fluctuations.

By utilizing the renormalization-group method, Hertz [29] and Millis [30] investigated the quantum critical phenomena in the itinerant–fermion systems. Fig. 2.2 illustrates such a phase diagram for a D–dimensional system ($D + z > 4$) [30]. Different regions of behavior are separated by the crossover lines T_I and T_{II} which depend on the choice of d and z. In the disordered phase of region I the fluctuations on the scale ξ have an energy much larger than $k_B T$ and therefore are of quantum nature. Fermi-liquid behavior is expected to exist at the lowest temperature in this region. Region II is a quantum-classical crossover region, in which the fluctuation modes at the scale of ξ have energies less than $k_B T$ but ξ is still determined by $\xi^2 \sim |\delta - \delta_c|$. In region III, ξ is controlled by temperature rather than $|\delta - \delta_c|$. Experimentally, there is no visible difference between region II and region III. NFL behavior of the specific heat, susceptibility, and resistivity are predicted in these two regions (see Table 2.1).

Similar results were also derived within the phenomenological self-consistent renormalization (SCR) model by Moriya *et al.* [31], which took into account the coupling among different modes of spin fluctuations in a self-consistent fashion. In comparison with the model studied by Millis and Hertz, more systematic treatment of the mode-mode coupling was considered in the SCR theory. Initially, the SCR theory was developed for the d-electron systems, however the behavior of many heavy-fermion compounds is also tentatively explainable within this theory.
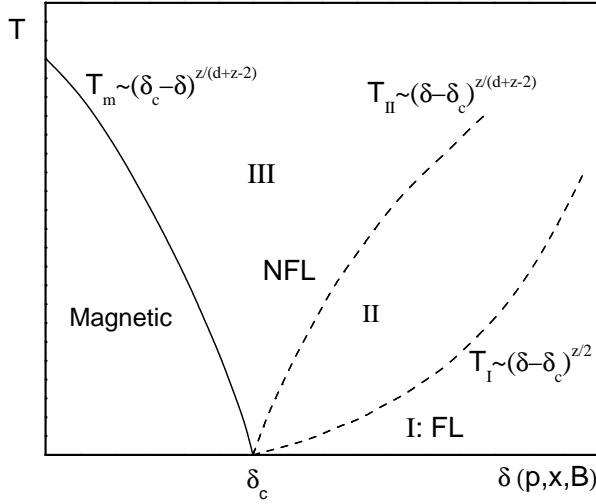
Figure 2.2: *A qualitative phase diagram for the quantum phase transition. The various regions (I, II, III) are discussed in the text. The magnetic transition at T_m may be suppressed by applying pressure (p), doping (x), or magnetic field (B). NFL behavior occurs in both regions II and III (after [30]).*

Theories	Physical quantities	AFM, $z=2$ $d=3$	AFM, $z=2$ $d=2$	FM, $z=3$ $d=3$	FM, $z=3$ $d=2$
(a)	C/T	$\gamma_0 - aT^{1/2}$	$\log(T_0/T)$	$\log(T_0/T)$	$T^{-1/3}$
	$\Delta\chi$	$T^{3/2}$	$\chi_0 - dT$	/	/
	$\Delta\rho$	$T^{3/2}$	T	T	/
(b)	C/T	$\gamma_0 - aT^{1/2}$	$\log(T_0/T)$	$\log(T_0/T)$	$T^{-1/3}$
	χ_Q	$T^{-3/2}$	$-(\log T)/T$	$T^{-4/3}$	$-1/T\log T$
	$\Delta\rho$	$T^{3/2}$	T	$T^{5/3}$	$T^{4/3}$
(c)	C/T	$\gamma_0 + T^{1/2}$	/	$\log(T_0/T)$	$T^{-1/3}$
	$\Delta\chi$	$T^{-3/2}$	/	$T^{-4/3}$	T^{-1}
	ρ	$T^{3/2}$	/	$T^{5/3}$	$T^{4/3}$

Table 2.1: *Temperature dependence of the specific heat (C/T), susceptibility (χ), and electrical resistivity (ρ) at a QCP derived from the spin-fluctuation theories by (a) Millis/Hertz; (b) Moriya et al.; (c) Lonzarich (after [23]).*

In addition to the above theories, Lonzarich also presented a phenomenological theory of spin fluctuations at a QCP [32]. In all these models, the spontaneous spin fluctuations slow down, grow in magnitude and range, and become strongly temperature dependent as the system approaches a magnetic QCP, leading to the divergence of the dynamic susceptibility. This indicates that the concept of quasiparticles might break down at the magnetic QCP and therefore non-Fermi-liquid behavior occurs.

Recently, Rosch studied the interplay of disorder and spin fluctuation at the quantum critical point and found that $\rho = \rho_0 + AT^n$ [33]. The exponent n is limited in the range of $1 \leq n \leq 1.5$ depending on the amount of disorder. For perfectly clean systems, one has $n = 2$. A small quantity of disorder may change the exponent n from $n = 2$ to $n = 1$ at the lowest temperatures, followed by a "bump"-like rise and fall of n at higher temperatures. However, n tends to 1.5 as $T \to 0$ in the dirty limit.

In Table 2.1, the main predictions of the above spin-fluctuation theories are summarized for various systems. Generally, different methods gave consistent results. Many of the experimental observations at the magnetic QCP (especially in the Ce-based compounds) could be described within the spin-fluctuation theory.

The theories shown above are built on the itinerant-fermion system. Recently, it was found that $CeCu_{6-x}Au_x$ [34, 35] and $YbRh_2(Si_{1-x}Ge_x)_2$ [36, 37] display unusual properties at the quantum critical points, i.e., the E/T and H/T scaling, the divergence of the effective mass, and the constant Kadowaki–Woods ratio in magnetic fields, which are difficult to be explained within the quantum spin–density–wave (SDW) scenario. To understand these new phenomena, Si *et al.* [38] and Coleman *et al.* [35, 39] proposed another type of quantum critical scenario, namely the local quantum phase transition. In this theory, vestiges of local moments remain as local critical modes which coexist with the long-wavelength critical fluctuations of the order parameter at the QCP. The dynamic susceptibility $\chi(q, \omega, T)$ displays an anomalous frequency and temperature dependence everywhere in the Brillouin zone:

$$\chi(q, \omega, T) = \frac{1}{f(q) + A\omega^\alpha M(\omega/T)}, \tag{2.54}$$

where $f(q)$ is a non-zero smooth function and $M(\omega/T)$ is a scaling function. The static

uniform (q=0) spin susceptibility has a modified Curie-Weiss form

$$\chi(T) = \frac{1}{\Theta + BT^\alpha}.$$

(2.55)

Reflecting on experiments, one has $\chi^{-1} - \chi_0^{-1} \sim T^\alpha$ ($\alpha < 1$), which has been observed in some heavy-fermion systems such as $CeCu_{5.9}Au_{0.1}$ [35, 40] and $YbRh_2Si_2$ [41, 42]. It was shown that 2D spin fluctuations favor such type of QCP.

3 Experimental method

In this chapter the technique used for measuring heat capacities ($C_{\min} \approx 1~\mu\text{J/K}$ at 0.1 K) of small solid samples at low temperatures ($0.03~\text{K} < T < 6~\text{K}$) and in high magnetic fields ($B < 12~\text{T}$) is described. The thermal losses, in this compensated heat–pulse technique, are compensated through a background heating. A detailed analysis of the heat flow takes the heat input and losses into account. This technique provides a versatile calorimeter for a wide range of heat capacities which achieves its main performance if several sample platforms are mounted and one sample is measured while the other may cool down.

3.1 Introduction

In any practical attempt to study low-temperature phenomena, the question of specific heats crops up immediately. The knowledge of specific heats forms a powerful tool in many areas, such as lattice vibrations, electronic distributions, energy levels in magnetic materials, and order-disorder phenomena. The commercially available calorimeters provide a fast and convenient way to obtain the specific heat over a wide temperature range. Temperatures below about 0.3 K, however, still require the construction of a calorimeter for the particular needs of the user. The techniques reported in literature are based on the very accurate heat-pulse method [43], the continuous warming technique with a rapid data collection [44] or the highly sensitive ac-technique [45]. They are mostly employed to meet special requirements, like high magnetic fields, samples with high

thermal conductivity or tiny samples at high pressure. For more details the interested reader is referred to review articles covering low-temperature calorimetry [46, 47, 48, 49]. The demand of a fast and sensitive low-temperature calorimeter ($T < 0.3$ K) for small samples (1 mg $< m <$ 50 mg) in magnetic fields ($B < 12$ T) has led to the realization of an improved relaxation-time technique. The set–up described here is optimized for temperatures in the range 0.03 K $< T < 6$ K and is based on the semi–adiabatic heat–pulse method used by N. E. Phillips' group at Berkeley. A first description of the method was given in the article by R. A. Fisher and coworkers [50]. The calorimeter described in the following can be used to much lower temperatures ($T \approx 30$ mK) than that used so far [51, 52]. The actual set–up compensates the inevitable heat losses during the measurement with an adjustable background heating. This compensation makes a rapid data acquisition possible. It is much faster than the conventional relaxation-time method since the time consuming tracking and stabilization of the calorimeter's temperature is not needed. This benefit is not obtained on the expense of accuracy and sensitivity: The quality of the specific–heat data is as high as that of the relaxation-time method.

In the following we describe the principle of the measurement, measuring procedure, experimental realization, and test measurements using tin and the heavy fermion (HF) $YbRh_2(Si_{0.95}Ge_{0.05})_2$ to demonstrate the use of the new method.

3.2 Principle of Measurement

The principle of the measurement is based on the definition of the heat capacity, eq.(2.1) in Sec. 2.1. It implies that an increase of the sample temperature by ΔT, caused by a supplied heat ΔQ, was achieved adiabatically. A low–temperature calorimeter ($T < 4$ K) has to have a thermal link between sample and surrounding to cool the sample. One possibility is to install a heat switch. Mechanical or superconducting switches are often cumbersome or not suitable in high magnetic fields. In the present calorimeter the thermal conductance of the mounting threads and electrical leads for the heater and thermometer was a compromise between the time necessary to cool the sample

to ≈ 30 mK and the capability to compensate the heat losses during the measurement. The thermal conductance of the selected threads allowed the heat capacity of the sample on the platform to be measured up to 6 K while the heat sink remains at the base temperature of the cryostat.
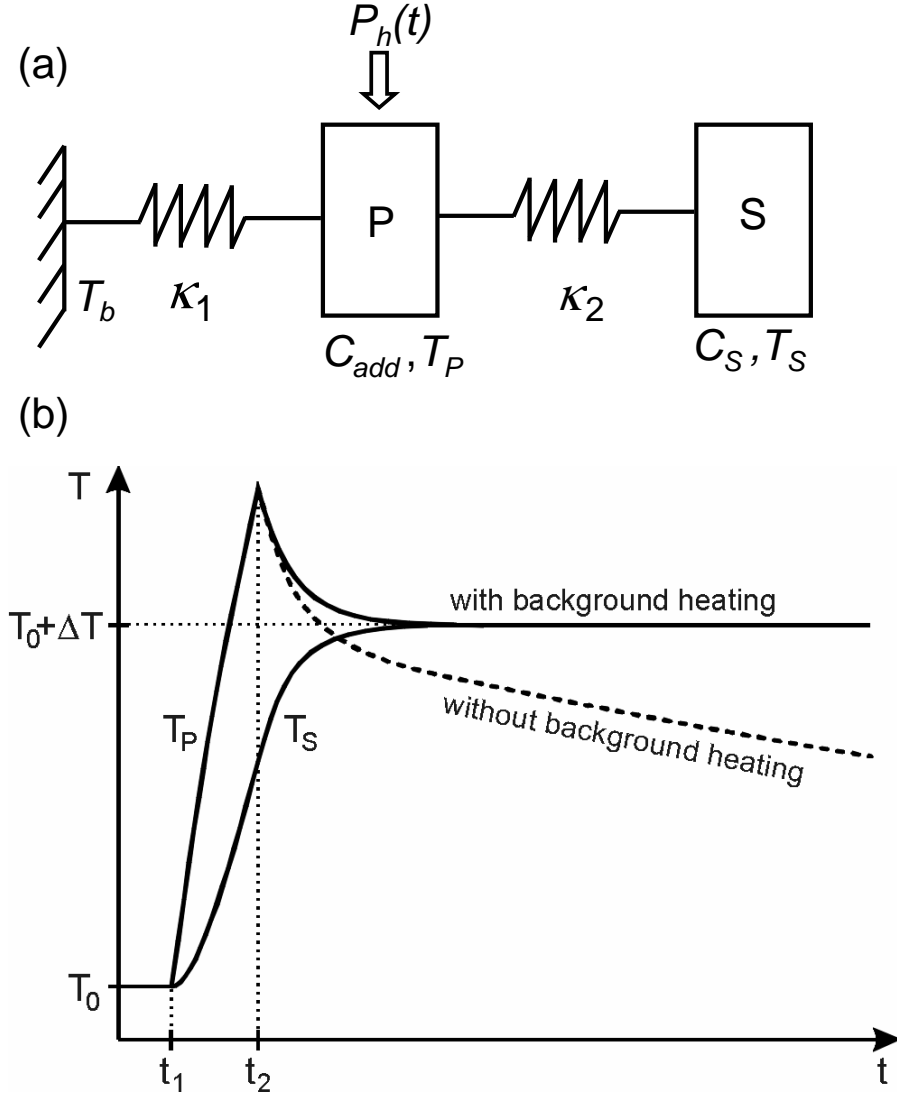
Figure 3.1(a) shows the heat–flow scheme of the sample/platform assembly. A weak thermal link, with thermal conductance K_1, establishes the connection between the platform and the thermal bath. The model takes the thermal conductance K_2 ($K_2 \gg K_1$) between platform and sample explicitly into account. In the steady state and at a constant heat–sink temperature (T_b) an appropriately chosen background heating power supplies the constant electrical power P_b into the heater. It compensates the heat loss through the thermal link and ensures a constant temperature of sample (T_S) and platform (T_P), i.e., $T_P = T_S \equiv T_0$ (see Fig. 3.1(b)). A heat pulse P_h of duration Δt_h adds the heat $\Delta Q_h = P_h \Delta t_h$ to the platform and T_P increases. After the heat–pulse power is switched off, the sample temperature relaxes towards the steady–state temperature $T_0 + \Delta T$, if the new background heating power was correctly adjusted. For a measuring cycle (of duration Δt) the average heat capacity C_S of the sample (at the mean temperature $T_0 + \frac{1}{2}\Delta T$) is given by the ratio of the *effectively* deposited heat $\Delta Q = \Delta Q_h - \Delta P_b \Delta t$ to the achieved temperature increase ΔT. This qualitative description of the compensated heat–pulse technique can be put into a mathematical model. In the following it is shown that the measured heat capacity is correct up to the order of $K_1/K_2 \ll 1$.

The total power, $P_P(t)$, deposited on the platform is given by the heat–flow scheme of Fig. 3.1(a):

$$P_P(t) = P_h - K_1(T_P - T_0) - K_2(T_P - T_S) . \tag{3.1}$$

As a consequence, the platform temperature increases from its initial value $T_P(t = t_1) = T_0 := T_{P,0}$ to

$$T_S(t) = T_{S,0} + \int_{t_1}^{t_2} \frac{P_S}{C_S} dt , \tag{3.2}$$

Figure 3.1: *(a) Heat–flow scheme of the compensated heat–pulse technique. The thermal conductances κ_1 between thermal bath (T_b) and platform (P) and κ_2 between sample (S) and platform are explicitly taken into account. The thermal bath remains at $T_b \leq$ 30 mK while the supplied heating power P_h increases the temperature of sample (T_S) and platform (T_P) up to 6 K. C_P and C_S denote the heat capacities of platform and sample, respectively. (b) Time dependence of T_S and T_P. A heat pulse during $\Delta t_h = t_2 - t_1$ delivers the heat ΔQ_h to the platform and yields a temperature increase by ΔT. An adjustable background heating compensates the heat losses through the thermal link and maintains a constant ΔT for $t > t_2$. Without additional background heating the temperature would exponentially approach T_0 (dashed line).*

with C_S the heat capacity of the sample and

$$P_S(t) = K_2(T_P - T_S) \ , \tag{3.3}$$

the power arriving at the sample. These equations yield the time dependence of $T_P(t)$ described by:

$$\frac{C_S C_P}{K_1 K_2}\ddot{T} + \left(\frac{C_S + C_P}{K_1} + \frac{C_S}{K_2}\right)\dot{T} + T = \frac{P_h}{K_1} + T_0 \ . \tag{3.4}$$

The general solution for $T_P(t)$ is

$$T_P(t) = A_1 e^{-t/\tau_1} + A_2 e^{-t/\tau_2} + \frac{P_h}{K_1} + T_0 \ . \tag{3.5}$$

A similar differential equation for $T_S(t)$ leads to

$$T_S(t) = B_1 e^{-t/\tau_1} + B_2 e^{-t/\tau_2} + \frac{P_h}{K_1} + T_0 \ . \tag{3.6}$$

In eqs. (3.5) and (3.6) the time constants τ_1 and τ_2 refer to the positive and negative signs, respectively, in the expression

$$\tau_{1,2} = \frac{1}{2K_1 K_2}\Big[(C_S + C_P)K_2 + C_S K_1 \pm \tag{3.7}$$
$$\pm \sqrt{[(C_S + C_P)K_2 + C_S K_1]^2 - 4C_S C_P K_1 K_2}\Big] \ .$$

The coefficients A_1, A_2, B_1, and B_2 are given by the starting conditions at $t = 0$:

$$A_{1,2} = \frac{1}{\tau_{1,2} - \tau_{2,1}}\bigg\{\frac{C_S}{K_1}(T_{S,0} - T_{P,0}) + \tag{3.8}$$
$$+ \left[\frac{C_S}{K_2} - \tau_{1,2}\right]\left[\frac{P_h}{K_1} + T_b - T_{P,0}\right]\bigg\}$$
$$B_{1,2} = \left\{1 + \frac{K_1}{K_2} - \frac{C_P}{K_2 \tau_{1,2}}\right\} A_{1,2} \ . \tag{3.9}$$

The aim of the present set–up is to maintain the increase of sample and platform temperature by ΔT. To achieve this, the heat losses have to be compensated by an

additional background heating P_h. A constant ΔT implies that $T_\mathrm{P}(t)$ and $T_\mathrm{S}(t)$ are independent of τ_1 since the heat losses occur through the weak link (described by K_1 and τ_1). This requires that $A_1 = 0$ in eq. (3.5). Using this boundary condition in eq. (3.8) and defining

$$\Delta T = T_\mathrm{P}(t \gg t_2) - T_\mathrm{P}(t_1) \ , \tag{3.10}$$

the temperature of the platform and sample has increased by

$$\Delta T = \frac{\Delta P}{K_1}(1 - e^{-\Delta t_\mathrm{h}/\tau_1}) \ , \tag{3.11}$$

where $\Delta P := P_\mathrm{h} - P_\mathrm{b}$ is the effectively added power to the platform. For a weak thermal link between platform and temperature reservoir, the condition $\tau_1 \gg \Delta t_\mathrm{h}$ is fulfilled and eq. (3.11) simplifies to

$$\frac{\Delta P}{\Delta T}\Delta t_\mathrm{h} = K_1 \tau_1 \ . \tag{3.12}$$

The right hand side of eq. (3.12) follows from eqs. (3.5)–(3.7) for $t = 0$ and can be written as

$$K_1 \tau_1 \approx (C_\mathrm{S} + C_\mathrm{P}) \left(1 + \frac{K_1}{K_2}\frac{C_\mathrm{S}}{C_\mathrm{S} + C_\mathrm{P}}\right) \ . \tag{3.13}$$

In the limit $K_1/K_2 \ll 1$ the total heat capacity $C = C_\mathrm{S} + C_\mathrm{P}$ of the sample/platform assembly according to eq. (3.13) is then determined by the measured quantities of eq. (3.12). In the present set–up $K_1/K_2 \ll 1$ is fulfilled over a wide temperature range. An exact number, however, is difficult to state since K_2 strongly depends on the shape and the internal thermal conductivity of the measured sample.

3.3 Measuring procedure

The computer–controlled measuring routine performs for each cycle k the determination of the heat capacity C^k, the adjustment of the background heating P_b^{k+1}, and the

estimation of the new heat–pulse power P_h^{k+1}. In order to clarify the procedure, the time variation of the *sample* temperature and the supplied power to the platform is sketched in Fig. 3.2. In the course of time the background heating as well as the power of the heat pulse increase to compensate the temperature dependent heat leak and to achieve the desired increase of the sample temperature, respectively. The heat capacity of the sample, $C(T_S^k)$, during the measuring cycle k at the mean sample temperature

$$T_S^k = \frac{1}{2}(T_{lo}^k + T_{hi}^k) \tag{3.14}$$

is given by

$$C^k := C(T_S^k) \simeq P\frac{\Delta t}{\Delta T} = (P_{in}^k - P_{out}^k)\frac{\Delta t_h}{T_{hi}^k - T_{lo}^k} . \tag{3.15}$$

The incoming power P_{in}^k is equal to P_h^k whereas the heat flow P_{out}^k to the temperature bath is taken as the average of the out flowing heat $P_{out,lo}^k$ immediately before the heat pulse

$$P_{out,lo}^k = P_b^{k-1} - C_{lo}^k \dot{T}_{lo}^k \tag{3.16}$$

and immediately after the heat pulse

$$P_{out,hi}^k = P_b^k - C_{hi}^k \dot{T}_{hi}^k . \tag{3.17}$$

Here, $\dot{T}_{hi}^k$ and $\dot{T}_{lo}^k$ are the temperature drifts at T_{hi}^k and T_{lo}^k, respectively (see Fig. 3.2).

In order to eliminate C_{lo}^k and C_{hi}^k in eq. (3.16) and eq. (3.17), respectively, a linear temperature dependence of C^k is assumed. Then, using eq. (3.15) the heat capacity C^k is determined by

$$C^k \approx \frac{2P_h^k - (P_b^{k-1} + P_b^k) + \left[(1 - f_{lo}^k)\dot{T}_{lo}^k + (1 - f_{hi}^k)\dot{T}_{hi}^k\right] C^{k-1}}{2(T_{hi}^k - T_{lo}^k)/\Delta t_h - (f_{lo}^k\dot{T}_{lo}^k + f_{hi}^k\dot{T}_{hi}^k)}, \tag{3.18}$$

with the coefficients f_{lo}^k and f_{hi}^k defined as

$$f_{lo}^k = \frac{T_{lo}^k - T_S^{k-1}}{T_S^k - T_S^{k-1}} \tag{3.19}$$
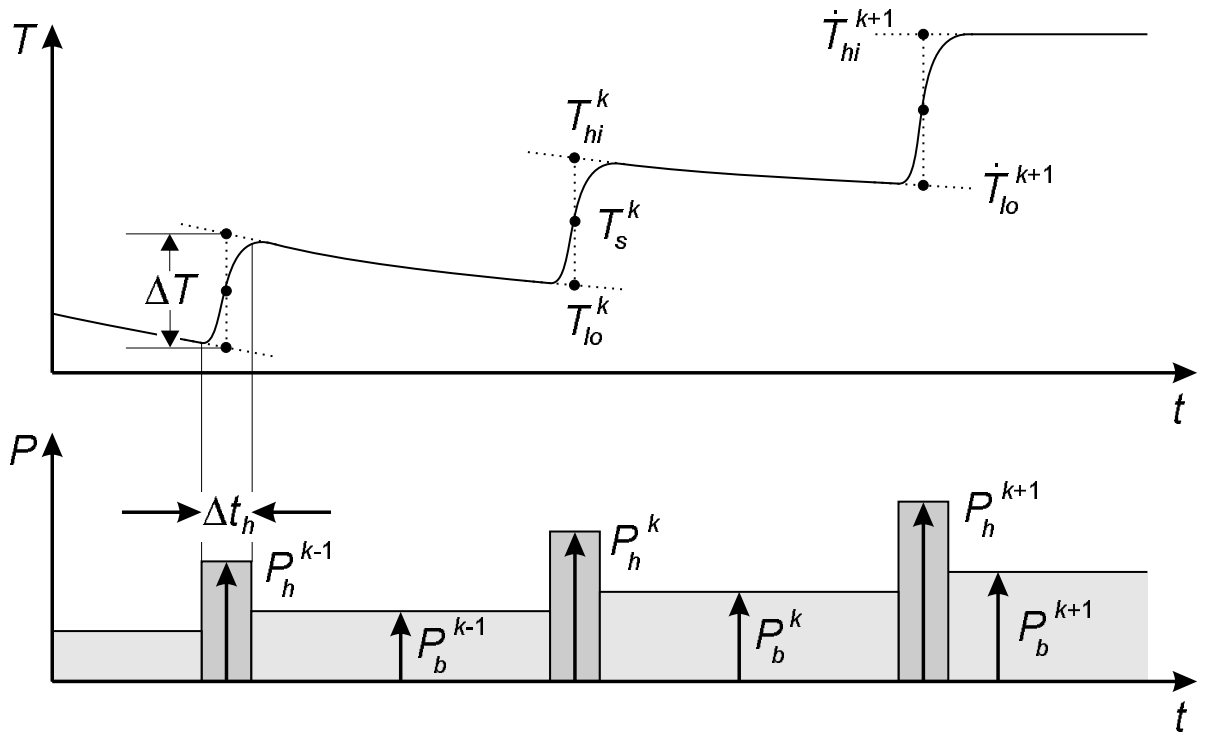
Figure 3.2: *Time dependence of the sample temperature T_S, the power of the heat pulse P_h, and the background heating P_b for several measuring cycles. In cycle k a heat pulse supplies the electrical power P_h^k to the platform. It increases the sample temperature by $\Delta T = T_{hi}^k - T_{lo}^k$. The determination of the heat capacity C^k at T_S^k takes the temperature drifts $\dot{T}_{lo}^{k+1}$ and $\dot{T}_{hi}^{k+1}$ into account (see text). The background heating P_b^k is adjusted for each cycle.*

and

$$f_{\text{hi}}^k = \frac{T_{\text{hi}}^k - T_{\text{S}}^{k-1}}{T_{\text{S}}^k - T_{\text{S}}^{k-1}} \ . \tag{3.20}$$

Due to the temperature dependence of the thermal conductances K_1 and K_2 the heat losses increase with increasing temperature. This requires to adjust the background heating after each heat pulse. Such an adjustment will never be ideal and results in a temperature drift $\dot{T}_{\text{hi}}^k \neq 0$ during the measuring cycle k. Thus, the chosen background heating P_{b}^k has to be corrected by,

$$P_{\text{corr}}^k = -C_{\text{hi}}^k \dot{T}_{\text{hi}}^k \approx - \left[f_{\text{hi}}^k C^k + (1 - f_{\text{hi}}^k)C^{k-1} \right] \dot{T}_{\text{hi}}^k \ . \tag{3.21}$$

This can be extrapolated to obtain an optimized background heating for the next step:

$$\begin{aligned} P_{\text{b}}^{k+1} \ \approx \ & P_{\text{b}}^{k-1} + P_{\text{corr}}^{k-1} + && (3.22) \\ & + \ \frac{T_{\text{hi}}^{k+1} - T_{\text{hi}}^{k-1}}{T_{\text{hi}}^k - T_{\text{hi}}^{k-1}} \left[(P_{\text{b}}^k + P_{\text{corr}}^k) - (P_{\text{b}}^{k-1} + P_{\text{corr}}^{k-1}) \right] \ . \end{aligned}$$

The heat capacity of the sample in the next cycle might be different and therefore, the power of the heat pulse has to be re–estimated. It has to be ensured that the desired temperature increase $\Delta T = T_{\text{hi}}^{k+1} - T_{\text{lo}}^{k+1}$ is achieved. Thus, the power for the new heat pulse is according to eq. (3.15) approximated by

$$P_{\text{h}}^{k+1} = P_{\text{in}}^{k+1} \approx C^{k+1} \frac{T_{\text{hi}}^{k+1} - T_{\text{lo}}^{k+1}}{\Delta t_{\text{h}}} + P_{\text{out}}^{k+1}. \tag{3.23}$$

This approximation depends on an estimate of the expected heat capacity and heat loss in the following measuring cycle. An estimation of C^{k+1} can be obtained by a linear extrapolation of the two preceding heat capacities:

$$C^{k+1} \approx f_{\text{S}}^{k+1} C^k + (1 - f_{\text{S}}^{k+1})C^{k-1}. \tag{3.24}$$

The heat flow P_{out}^{k+1} to the bath is according to eq. (3.22), with the requirement $\dot{T}_{\text{hi}}^{k+1} \equiv 0$, given by

$$\begin{aligned} P_{\text{out}}^{k+1} \ \approx \ & (P_{\text{b}}^{k+1} + P_{\text{b}}^k)/2 - && (3.25) \\ & - \ \left[g_{\text{lo}}^{k+1} C^k + (1 - g_{\text{lo}}^{k+1})C^{k-1} \right] \dot{T}_{\text{lo}}^{k+1}/2 \ , \end{aligned}$$

using the coefficient

$$g_{\text{lo}}^{k+1} = \frac{T_{\text{lo}}^{k+1} - T_{\text{S}}^{k-1}}{T_{\text{S}}^{k} - T_{\text{S}}^{k-1}} \; . \tag{3.26}$$

With eq. (3.24) and eq. (3.25) the new heat pulse P_{h}^{k+1} eventually results to

$$
\begin{aligned}
P_{\text{h}}^{k+1} \quad \approx \quad & (P_{\text{b}}^{k+1} + P_{\text{b}}^{k})/2 + \\
+ \quad & \left[f_{\text{S}}^{k+1} \frac{T_{\text{hi}}^{k+1} - T_{\text{lo}}^{k+1}}{\Delta t_{\text{h}}} - \frac{g_{\text{lo}}^{k+1}}{2} \dot{T}_{\text{lo}}^{k+1} \right] C^{k} \\
+ \quad & \left[(1 - f_{\text{S}}^{k+1}) \frac{T_{\text{hi}}^{k+1} - T_{\text{lo}}^{k+1}}{\Delta t_{\text{h}}} - \frac{1 - g_{\text{lo}}^{k+1}}{2} \dot{T}_{\text{lo}}^{k+1} \right] C^{k-1} \; ,
\end{aligned}
\tag{3.27}
$$

using the definition

$$f_{\text{S}}^{k+1} = \frac{T_{\text{S}}^{k+1} - T_{\text{S}}^{k-1}}{T_{\text{S}}^{k} - T_{\text{S}}^{k-1}} \; . \tag{3.28}$$

The computer–controlled routine needs as input parameter the desired temperature increase ΔT and the temperature range. The measurement runs automatically as long as no sharp feature in $C(T)$ occurs. Even in the case of a first–order phase transition the extrapolations in eqs. (3.24)–(3.27) yield a good estimate and the computer–controlled sequence runs without problems.

3.4 Experimental realization

A sketch of the sample platform is shown in Fig. 3.3. The platform is a thin silver plate ($4 \times 3 \times 0.4 \text{ mm}^3$), with a RuO_2–chip temperature sensor ($m = 0.8$ mg, $R_0 \approx 2$ kΩ at room temperature) and a resistive heater (10 kΩ film resistor, $m = 2.4$ mg). To realise a low thermal conduction between sample platform and environment the platform is mounted with two thin nylon threads ($\phi = 80\ \mu$m) on a silver ring ($\phi = 25$ mm). Furthermore, manganin leads ($\phi = 30\ \mu$m, length ≈ 10 cm) are used to connect the heater and thermometer to a plug placed on the ring. A tiny amount of apiezon N grease is used for sample adhesion to prevent the domination of grease in heat capacity. Apiezon N grease is often used as a bonding agent for samples in specific–heat measurements because it can be easily removed.
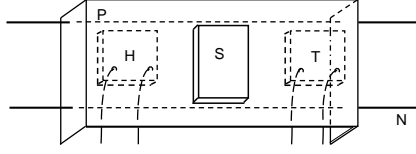
Figure 3.3: *Schematic view of the platform. P: silver platform, N: nylon thread, S: sample, T: RuO_2–chip temperature sensor, H: heater.*

For this configuration the thermal conductance K_1 varies between 1×10^{-9} W/K at 0.1 K and 1×10^{-7} W/K at 4.2 K. The minimum temperature is limited by K_1 and the residual thermal leak. It comprises the heat input caused by mechanical vibrations of the cryostat, but other sources for energy dissipation, like high–frequency noise cannot be ruled out. The residual power is much less than 10 pW and limits the platform temperature to about 30 mK. An additional heat input of the same order of magnitude is produced at the highest magnetic fields and prevents the platform temperature to be less than ≈ 50 mK.

The present configuration contains two platforms with the configuration described above and a third platform which has an "L" shape which allow us to measure the specific heat along and perpendicular to the field direction.

One of the severest problems in low–temperature specific–heat measurements in quasi-adiabatic conditions is the selection of the lead wires. Because the wires also provide a thermal connection to the isothermal ring, the thermal conductivity of the wires is very important in order to maintain quasi-adiabatic conditions for the specific–heat measurements. We decided to use manganin wires for electrical contacts because of their low thermal conductivity and small temperature dependence of their electrical resistivity. In order to improve the thermal isolation of the sample we used 5-6 cm long coiled wires.

First we tried to use different kinds of wires: stainless steel, various superconducting wires, NbTi with a Cu matrix, but unsuccessfully. In all cases thermal relaxation was too fast. In the case of NbTi we removed the Cu coating with concentrated HNO_3.

The principal disadvantages of this is that the resulting joints tend to be mechanically quite fragile. To improve the mechanical stability of the platform we replaced the nylon threads by two thin lead taken from pencils. The advantage is that the system is less sensitive to mechanical vibrations but the sample holder is too fragile.

The RuO_2–chip temperature sensor was calibrated in the temperature range 15 mK $<$ $T <$ 200 mK against a fixed–point device (SRM 768 of the former National Bureau of Standards, USA) and against a commercially calibrated RuO_2 thermometer in the temperature range 50 mK $< T <$ 6 K. The RuO_2 thermometer, RX–102-AA–M, was calibrated by the manufacturer, Lake Shore Cryotronics, Inc., using the ITS–90 temperature scale. The resistance values of the RuO_2–chip sensor, R, were converted to temperature using $\log T = \sum_{n=0}^{4} a_n[\log(R - R_0)]^n$, with the fitting parameters a_n. Any strong deviation from a straight line in a $\log(T)$ vs. $\log(R - R_0)$ plot immediately reveals self heating of the sensor during calibration. Temperature sweeps were performed in various (constant) magnetic fields to obtain a sensor calibration at these particular fields. The RuO_2 chip was fixed on the platform (which was thermally anchored to the silver ring) while a calibrated thermometer mounted in the field–compensated region of the cryostat was used as a reference. For each field, a $T(R)$ function as given above was used to describe the data. The entire set of $T(R, B)$ data can be used to calculate a calibration for any field value needed during the experiment. In this procedure, particular attention was payed to magnetic field effects on R. The resistance of the RuO_2 sensor is $R \approx$ 30 kΩ at 30 mK and its sensitivity, i.e. $\partial \ln R/\partial \ln T$, increases almost linearly from -0.4 at 0.9 K to -0.54 at 30 mK (if R measured in kΩ and T in mK). At the lowest temperatures such an order of magnitude of R is well suited for an ac–bridge technique.

In order to determine the addenda of the platform, i.e., the specific heat of the heater, thermometer, wires, GE varnish used to attach the heater and resistor and grease (Apiezon N), the heat capacity of silver ($m =$ 92.6 mg, purity: 99.99+%) was measured in zero field and several fields up to 10 T. The heat capacity for the addenda was determined by subtracting the silver–reference equation, from the results and the contribution of the 0.13×10^{-3} g grease by the specific–heat data reported by H.J. Schink

and von Löhneysen [53]. The addenda in zero field is less than 0.2 μJ/K at 0.1 K and below 0.4 μJ/K at 1 K. No influence of the magnetic field on the addenda could be resolved.

The specific–heat measurements have been performed in a He^3/He^4 commercial dilution refrigerator ($T_{\min} \simeq 15$ mK) with a superconducting magnet ($B_{\max} \simeq 12$ T). The principle of cooling can be found in a number of books on low temperature physics, such as Refs. [15, 54]. In this cryostat the mixing chamber (MC) is placed 40 cm above the center of the magnet. The sample holder, with three different platforms is attached to the bottom of the MC. The MC is located at the center of the field-compensated area to avoid the heating effects due to induced eddy currents when sweeping the magnetic field. Standard digital dc sources and multimeters were used to supply the heating current and to read the voltage drop across the heater. An ac–resistance bridge measures the resistance of the RuO$_2$–chip sensor. As soon as the starting parameters are entered the necessary values like heat–pulse and background–heating current are calculated (see Appendix). Typical values for the applied power are above 10 nW in order to achieve a temperature increase $\Delta T/T_0$ of up to 3%. The duration of the heat pulses are less than 10 s and one measuring cycle can last up to 1000 s. Effects related to τ_2, i.e., a weak coupling of the sample to the platform or a low thermal conductivity of the sample can be detected during the experiment. Then the sample temperature has a characteristic time dependence as depicted in Fig. 3.1(b). A careful examination of the data clarifies whether the so–called τ_2 effect is negligible or the criterion $\kappa_1/\kappa_2 \ll 1$ is violated. In the latter case, the correction term in eq. (3.13) has to explicitly taken into account. Since the determination of K_2 is not straightforward, the concerned data are discarded.

3.5 Test measurements

A first test of the set–up was done with the measurement of the heat capacity of tin. A tin sample ($m = 165$ mg, purity: 99.999%) was attached with Apiezon N to the platform and data were recorded from 0.5 K to 6 K. The coefficient of the phonon contribution,

βT^3, to the heat capacity is calculated to $\beta = 0.28(1)$ mJ mol^{-1} K^{-4}. The heat capacity in the superconducting phase ($T_c = 3.72$ K) can be described by $C_{sc} = a\gamma T_c e^{(-bTc/T)}$ with $a = 6.0(1)$, $b = 1.8(1)$, and $\gamma = 1.94(1)$ mJ mol^{-1}K^{-2}. These values are in good agreement with literature data [55]. This test measurement revealed one drawback related to the weak thermal coupling. The mounting of the platform with the thin nylon threads is not suited for samples with masses larger than ≈ 50 mg. In this case the platform captures vibrations of the cryostat and the performance of the technique is considerably limited for $T < 0.3$ K. A better mounting, i.e., thicker threads or even a rigid connection of the platform to the silver ring, increases the thermal link. Then, the background heating is not able to compensate the heat losses at high temperature and the method can be used only in a small temperature range. If the sample has an adequate mass and $K_1/K_2 \ll 1$ is fulfilled, then a minimum heat capacity of about 1μJ/K at 0.1 K can be measured.

To test the performance of the compensated heat–pulse method in high magnetic fields the strongly correlated electron system YbRh$_2$(Si$_{0.95}$Ge$_{0.05}$)$_2$ was chosen. The temperature dependence of the specific heat was first carefully measured with a relaxation technique [56] in magnetic fields up to 6 T, while the present set–up allowed the field range to be extended up to 11.5 T. A complete discussion of the field dependence of the specific heat of YbRh$_2$(Si$_{0.95}$Ge$_{0.05}$)$_2$ in more details is given in Sec. 4.2.1. Here, we focus on the comparison of the specific heat of YbRh$_2$(Si$_{0.95}$Ge$_{0.05}$)$_2$ obtained with the two techniques, on the same sample ($m = 21$ mg). This comparison revealed that the values agree within 2% in zero field as well as in applied magnetic field [57]. Thus, we concluded that the compensated heat–pulse method can be used to measure the heat capacity in a wide temperature range and applied magnetic fields.

4 Heavy Fermion systems tuned to a QCP

4.1 Introduction

The transition from a magnetically ordered ground state to a non–magnetic ground state by tuning a non–thermal control parameter is presently a subject of strong interest within solid state physics. In systems such as $CeCu_{6-x}Au_x$ [34], $U_{1-x}Th_xNi_2Al_3$ [58], $CeIn_3$ [59], $CeCu_2Ge_2$ [60], $CePd_2Si_2$ [61], and UPt_3 [62] it is even suggested that the antiferromagnetic ordering temperature T_N as a function of external pressure (p), chemical doping (x), or magnetic field (B) continuously decreases down to $T_N = 0$ leading to a quantum critical point (QCP). In contrast to a classical phase transition, which takes place at finite temperature, $T > 0$, a QCP occurs at $T = 0$ and therefore is driven by a control parameter, $\delta(x, p, B)$, other than temperature [63].

HF systems, intermetallic compounds mostly based on Ce, Yb, or U, are ideal materials for the study of these phenomena, because these elements have an unstable f shell which can easily be tuned from a magnetic to a nonmagnetic configuration by alloying or applying pressure. Increasing the hybridization between the localized f and the conduction electrons leads to a weakening of the magnetic order, which eventually disappears. Thus, these materials can be tuned continuously from an antiferromagnetic (AFM) to a paramagnetic (PM) Fermi–liquid (FL) state or vice versa by the variation of a single

39

parameter, i.e., the hybridization strength J between f and conduction electrons, which determines both the characteristic energies T_K and T_{RKKY} for the Kondo effect and the RKKY interaction, respectively [22]. Close to the critical value J_c at which $T_N \rightarrow 0$, pronounced deviations from Landau–Fermi–liquid (LFL) behavior take place. While a huge number of Ce- and U-based HF systems have been discovered and thoroughly investigated up to now, much less Yb–based HF systems are presently known. Only very few of them are located close to the QCP on the magnetically ordered side, and there has been no example for an Yb system close to the QCP located on the non-ordered side at $p = 0$. Further on, we do not yet know of any Yb-based HF superconductor. These facts motivated us to look for new Yb–based systems situated close to the borderline of long–range magnetic order.

It is also worth noting that the dimensionality of the critical spin fluctuations plays an important role in NFL behavior. Therefore, in this work we have investigated the thermodynamic properties of tetragonal $Yb_{1-y}La_yRh_2(Si_{1-x}Ge_x)_2$ ($x = 0.05, y = 0.05, 0.1$), $YbIr_2Si_2$ and cubic $CeIn_{3-x}Sn_x$ systems, located close to the QCP. In order to approach the QCP we tuned these systems not only by substitution but also by magnetic field, as an alternative way. The results obtained will be discussed in the framework of two different scenarios: the localized moment (LM) scenario [35, 64, 65, 66] and the spin–density–wave (SDW) scenario [29, 30, 67, 68].

In the first scenario for the QCP, proposed by Si. et al [69], it was suggested that a key feature for the existence of the new type of QCP is that the magnetic fluctuations show a strongly anisotropic spectrum. In the model of Q. Si [69] it is assumed that the LM scenario takes place when the spin fluctuations are of 2D nature as observed experimentally in the case of orthorhombic $CeCu_{5.9}Au_{0.1}$ [70]. In this scenario it was shown that in the case of 2D spin fluctuations the system has its ordering transition precisely at the point where the local–moment problem also becomes critical. Therefore, at the QCP two kinds of fluctuations coexist; long–wavelength fluctuations from the nearby AFM phase (RKKY interaction) and local fluctuations originating from the local moments. Until now, the intermetallic alloys $CeCu_{6-x}M_x$ with $M = Au$ and Ag [35, 71]

favor this scenario. For YbRh$_2$Si$_2$ doped with Ge [56], 2D critical spin fluctuations can not be excluded either, since inelastic neutron–scattering measurements are still not available.

Unlike the local–moment scenario, in the SDW model the local moments are completely screened by the Kondo effect at $T = 0$ in the PM state and at the QCP. Different behaviors in thermodynamic and transport properties have been postulated in the case of two–dimensional (2D) or three–dimensional (3D) spin fluctuations (see chapter 2). Recently, R. Küchler et al. [72] showed that both the thermal–expansion and the specific–heat results in the tetragonal CeNi$_2$Ge$_2$ can be fitted by the respective expression for a 3D–AF–SDW theory. However, most systems which have been investigated in the past, are either tetragonal or orthorhombic such as CeCu$_2$Si$_2$ [73, 74], CePd$_2$Ge$_2$, CeNi$_2$Ge$_2$ [61, 72], or CeCu$_{6-x}$Au$_x$ [34] and hence have an intrinsic crystalline anisotropy. The lower crystallographic symmetry might result in fluctuations with reduced dimensionality. However, in the tetragonal CeNi$_2$Ge$_2$ evidences for the existence of 3D spin fluctuations were reported [75]. Thus, a direct explicit connection between the crystal structure and the observed NFL behavior is questionable.

Given these experimental and theoretical developments, thermodynamic experiments on cubic systems are very important to shed light on the correlation between the symmetry of the crystal lattice, the dimensionality of the fluctuations and the nature of the QCP, as a preferential orientation of the spin fluctuations due to crystal–lattice structure appears unlikely. It is believed that those systems, if at all, are (well) described by spin–fluctuation theory. So far, no specific–heat experiments on a cubic system in the vicinity of the QCP have been reported. In this context CeIn$_{3-x}$Sn$_x$ provides a cubic reference material for investigation of the QCP. The second section in this chapter will deal with low–temperature ($0.03 \leq T \leq 6$ K) and high magnetic field ($B \leq 11.5$ T) specific–heat measurements on single–crystal samples of CeIn$_{3-x}$Sn$_x$, ($0.55 \leq x \leq 0.8$).

4.2 Yb–based compounds with ThCr$_2$Si$_2$ structure

The compound YbRh$_2$Si$_2$ attracted much attention as this system is a clean, stoichiometric Yb–based compound which at ambient pressure (p) undergoes a weak AF phase transition at a Néel temperature as low as 0.07 K [76]. By applying a small magnetic field, $B_c \simeq 0.06$ T ($B \perp c$, i.e., within the easy magnetic plane), one can suppress the magnetic order and tune the material to a ("field-induced") QCP [37]. Upon further increasing the field one enters a heavy LFL phase at sufficiently low temperatures. NFL phenomena are observed in the close vicinity of B_c down to the lowest accessible temperature (≈ 20 mK) and, in addition, relatively far away from B_c at surprisingly high temperatures ($T \leq 10$ K). The observed NFL effects, have been related to the proximity of a magnetic instability. This was inferred from the observation of the extraordinarily low antiferromagnetic (AFM) ordering temperature (~ 70 mK). The AFM transition is of second order [37] and the ordering temperature, T_N, is the lowest among all undoped HF systems at ambient pressure. Therefore, this system is highly suited to study the quantum critical phenomena.

The application of pressure to YbRh$_2$Si$_2$ increases T_N [76] since the ionic radius of the nonmagnetic $4f^{14}$ Yb^{2+} configuration exceeds that of the magnetic $4f^{13}$ Yb^{3+} one. Therefore, "demagnetization" of Yb, opposite to the case of Ce, requires the application of "negative pressure". The evolution of the antiferromagnetic transition temperature with pressure, denoted by $T_N(p)$, can be traced over more than one order of magnitude. The extrapolation of $T_N(p) \to 0$ yields a negative critical pressure $p_c = -0.3 \pm 0.1$ GPa [77, 78], reflecting that a small expansion of the unit–cell volume tunes $T_N \to 0$. This can be achieved by substitution of Si by the isoelectronic, but larger Ge [79]. In fact, in the case of a slightly doped YbRh$_2$(Si$_{1-x}$Ge$_x$)$_2$ single crystal with a nominal Ge concentration of $x = 0.05$, the Néel temperature was found to be as low as $T_N = 20$ mK [56]. Consequently, the critical field to drive the system towards the QCP is substantially lower than for the undoped compound ($B_c = 0.027$ T, $B \perp c$).

For this system, the Sommerfeld coefficient $\gamma(T)$ of the electronic specific heat and, thus,

the effective quasiparticle mass m_{eff} diverges logarithmically within one and a half orders of magnitude in temperature, i.e., for 0.3 K$< T <$ 10 K. In the same temperature window, the resistivity depends linearly on T, $\Delta\rho \propto T$. This is equivalent to an effective quasiparticle–quasiparticle scattering cross section, proportional to $A = \Delta\rho/T^2$ which diverges as $1/T$. These unique temperature dependences of $\gamma(T)$ and $\Delta\rho(T)$ indicate that at the QCP, both m_{eff} and the scattering cross section are becoming singular on the whole Fermi surface, i.e., in a way predicted by the SDW scenario assuming strictly two–dimensional spin fluctuations [29, 30, 80]. Inelastic neutron–scattering experiments apt to check the existence of such 2D fluctuations are presently under preparation. At temperatures $T < 0.3$ K, $\gamma(T)$ shows a stronger than logarithmic divergence, $\gamma(T) \propto T^{-\eta}$, $\eta \simeq 0.4$, while $\Delta\rho$ keeps following the linear T dependence to the lowest accessible temperature of ~ 10 mK [56]. This apparent disparity between the T dependences of the thermodynamic quantity $\gamma(T)$ and the transport property $\Delta\rho(T)$ was taken as evidence of a break up of the "composite fermions" on the approach to the ($B = 0$) QCP [56]. For $B = 0$, the QCP is expected to occur at a slightly higher Ge concentration. Ge doping, which would allow tuning YbRh$_2$Si$_2$ through the QCP, cannot achieve a complete suppression of T_N due to great difficulties in growing single crystals. An alternative route to suppress the AFM order is the partial substitution of Yb by nonmagnetic La in Yb$_{1-y}$La$_y$Rh$_2$Si$_2$ since La doping provides a further possibility for expanding the lattice and inducing a negative chemical pressure. In this work we performed specific–heat measurements at low temperatures, 0.03 K$\leq T \leq$ 6 K, and high fields (up to 12 T) to investigate the quantum critical behavior in Yb$_{1-y}$La$_y$Rh$_2$(Si$_{1-x}$Ge$_x$)$_2$ ($x = 0.05, y = 0.05, 0.1$). Moreover, we present results on YbIr$_2$Si$_2$, which was recently proposed as one of the cleanest Yb–based HF systems located on the nonmagnetic side of a QCP.

4.2.1 YbRh$_2$(Si$_{1-x}$Ge$_x$)$_2$ – a HF system close to a QCP

This system is ideally suited to study an AFM QCP since it is located very near to the magnetic instability ($T_N = 0.02$ K for $x = 0.05$) and since the effect of disorder

is minimized in these high-quality single crystals with low residual resistivities. The residual resistivity of the Ge–doped crystal is 5 $\mu\Omega$cm, only a factor of five larger than that of undoped $YbRh_2Si_2$. $YbRh_2(Si_{1-x}Ge_x)_2$ with a nominal Ge concentration of $x = 0.05$ was grown from In flux as described earlier [41]. $YbRh_2(Si_{0.95}Ge_{0.05})_2$ crystallizes in the tetragonal $ThCr_2Si_2$ structure. Recently [56] it was shown that the application of an external magnetic field tunes $YbRh_2(Si_{0.95}Ge_{0.05})_2$ through a quantum critical point into a LFL state at high field. In this work the heat capacity was carefully measured with a relaxation technique in magnetic fields up to 6 T (Ref. [56]) while the present setup allowed the field range to be extended up to 11.5 T. In these measurements, magnetic fields were applied perpendicular to the crystallographic c axis, within the easy magnetic plane.

Figure 4.1 shows the low–temperature dependence ($0.03\,\mathrm{K} \leq T \leq 5\,\mathrm{K}$) of the electronic specific heat divided by temperature, $\Delta C(T)/T$, in various magnetic fields. $\Delta C = C - C_{nuc}$ is obtained by subtracting the nuclear contribution C_{nuc} from the total specific heat C as described below while the phonon part can be safely ignored in this temperature range. At fields above 0.2 T, $\Delta C(T)/T$ is very weakly temperature dependent, as expected in a LFL. A weak maximum is observed in $B = 0.2$ T at $T_{max} = 0.2$ K below which the field-induced LFL state is observed. As the field is increased the LFL region extends towards high temperatures and T_{max} increases linearly with B indicating that entropy is transferred from the low-temperature upturn to the NFL regime above T_{max} by the application of field.

The total specific heat, $C(T)$, is depicted in the inset of Fig. 4.1 for different magnetic fields. The field–independent quadrupolar contribution $C_Q = \alpha_Q/T^2$ has to be subtracted from the raw data below about 0.1 K. α_Q/T^2 represents the high–temperature part of the nuclear–Schottky anomaly and α_Q was estimated to $\alpha_Q = 5.68 \times 10^{-6}$ JKmol^{-1} by Mössbauer experiments probing the electrical quadrupole splitting [81] of the nuclear spin $I = 5/2$ of ^{173}Yb (natural abundance of 0.162). The field–induced part to the heat capacity, i.e., the nuclear Zeeman contribution $C_{hf} = \alpha(B)/T^2$, was obtained by fitting CT^2 vs T^3 with the eq. $CT^2 = \alpha + \gamma T^3$ where $\alpha(B)$ is the $T = 0$ intercept and the slope
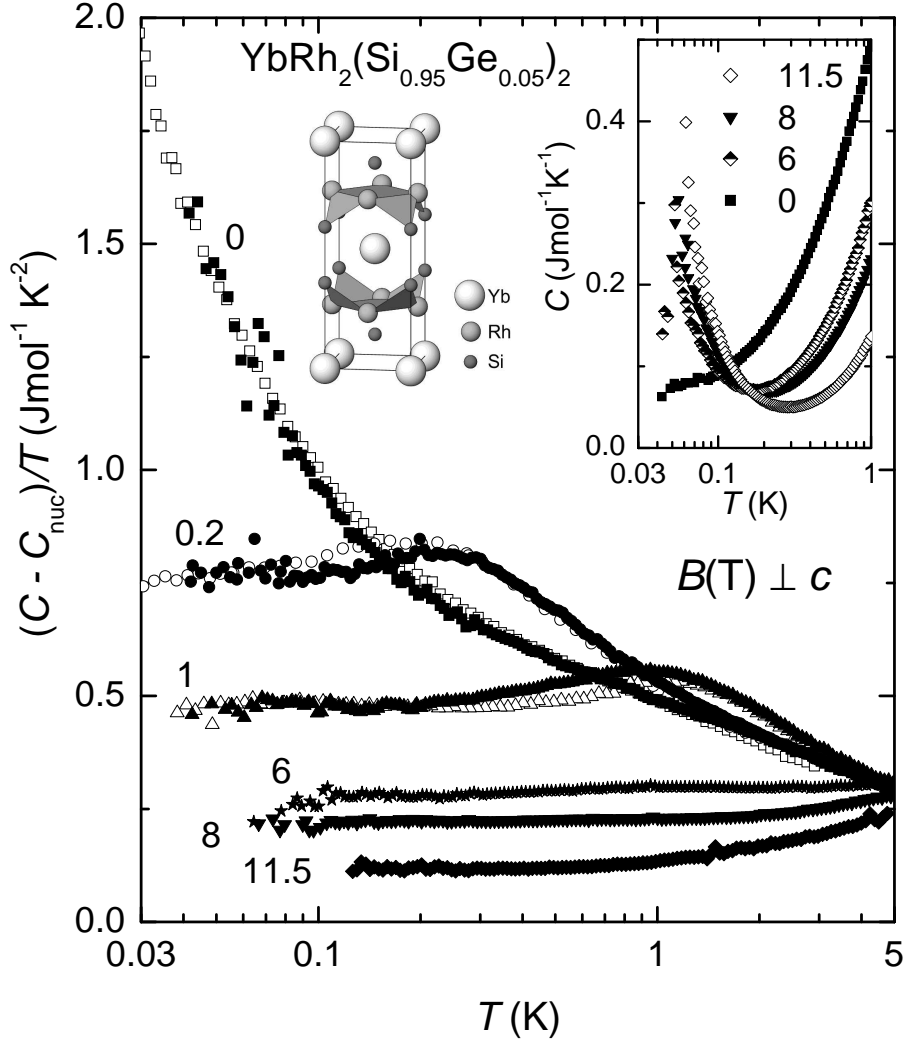
Figure 4.1: *Temperature dependence of the electronic heat capacity divided by temper-*
ature, $\Delta C/T = (C - C_{nuc})/T$, of YbRh$_2$(Si$_{0.95}Ge_{0.05}$)$_2$ in various magnetic fields B
applied perpendicular to the crystallographic c axis. The nuclear contributions C_{nuc}
to the heat capacity have been subtracted from the raw data. Solid and open symbols
represent data obtained with the compensated heat–pulse and relaxation [56] method,
respectively. Inset: Low–temperature part of the raw data, C vs T. The strong up-
turn at low temperature is due to the nuclear–Zeeman contribution to the total heat
capacity.

represents the Sommerfeld coefficient γ. We have also determined α_Q for $B = 0$ using this method and the value obtained ($\alpha_Q = 4.88 \times 10^{-6}$ JKmol^{-1}) agrees well with the Mössbauer experiments [81].

The obtained Sommerfeld coefficient, $\gamma(B)$, is plotted in Fig. 4.2 together with the data of Ref. [56] vs. $B - B_c$ where $B_c = 0.027$ T is the critical field. The reliability of the determination of $\alpha(B)$ can be checked by calculating the field dependence of the magnetisation, $M(B)$, from the specific–heat data. It can be calculated by using the eq., $M(B) = (B_{hf} - B)/A_{Yb}$, with A_{Yb} the hyperfine coupling constant and the hyperfine field $B_{hf} = \sqrt{(\alpha(B) - \alpha_Q)/\alpha_{dip}}$. The gyromagnetic ratio $\alpha_{dip} = 0.076 \times 10^{-6}$ JKmol^{-1}T^{-2} is known from NMR data [82]. The magnetisation estimated from the heat capacity can be matched to the measured $M(B)$ curve when $A_{Yb} = 120$ T/μ_B is assumed (see inset to Fig. 4.2). The diverging γ value on approaching B_c, stronger than logarithmic ($\gamma \propto (B - B_c)^{-0.33}$), was a strong argument for the conclusion in Ref. [56] that the composite fermions breakup in the approach to the QCP. This idea has been put forward by Coleman et al. [64, 65, 83]. On the other hand, the data reported in Ref. [56] (open symbols in Fig. 4.2) above $B - B_c = 0.3$ T were described by $\gamma = a \ln[b/(B - B_c)]$, with $a = 0.126(4)$ Jmol^{-1}K^{-2} and $b = 59(7)$ T, as predicted in a 2D spin–density–wave scenario (dashed line in Fig. 4.2) (see Sec. Theory).

As shown in Fig. 4.2, the deviation of $\gamma(B)$ from the extrapolated 2D spin–density–wave scenario occurs above B^* indicating that the quasiparticle mass, measured by γ, is reduced above B^*. At a field value $B^* \approx 8.5$ T the $M(B)$ curve (solid line in the inset of Fig. 4.2) starts to change the slope. In this context, very relevant are recent DC magnetization results on YbRh$_2$Si$_2$ [84] at low temperatures, down to 0.04 K, high magnetic field $B \leq 11.5$ T and under hydrostatic pressure $P \leq 1.3$ GPa. A kink at $B^\star = 9.9$ T at ambient pressure was observed in magnetization measurements accompanied by an abrupt decrease of γ which was interpreted as localization of $4f$ electrons and suppression of the heavy–fermion state at magnetic fields above B^*. Thus, we can conclude that the features observed in $\gamma(B)$ and $M(B)$ at $B^\star$ for the YbRh$_2$(Si$_{0.95}$Ge$_{0.05}$)$_2$ system originate from the above–mentioned localization of the 4f holes.
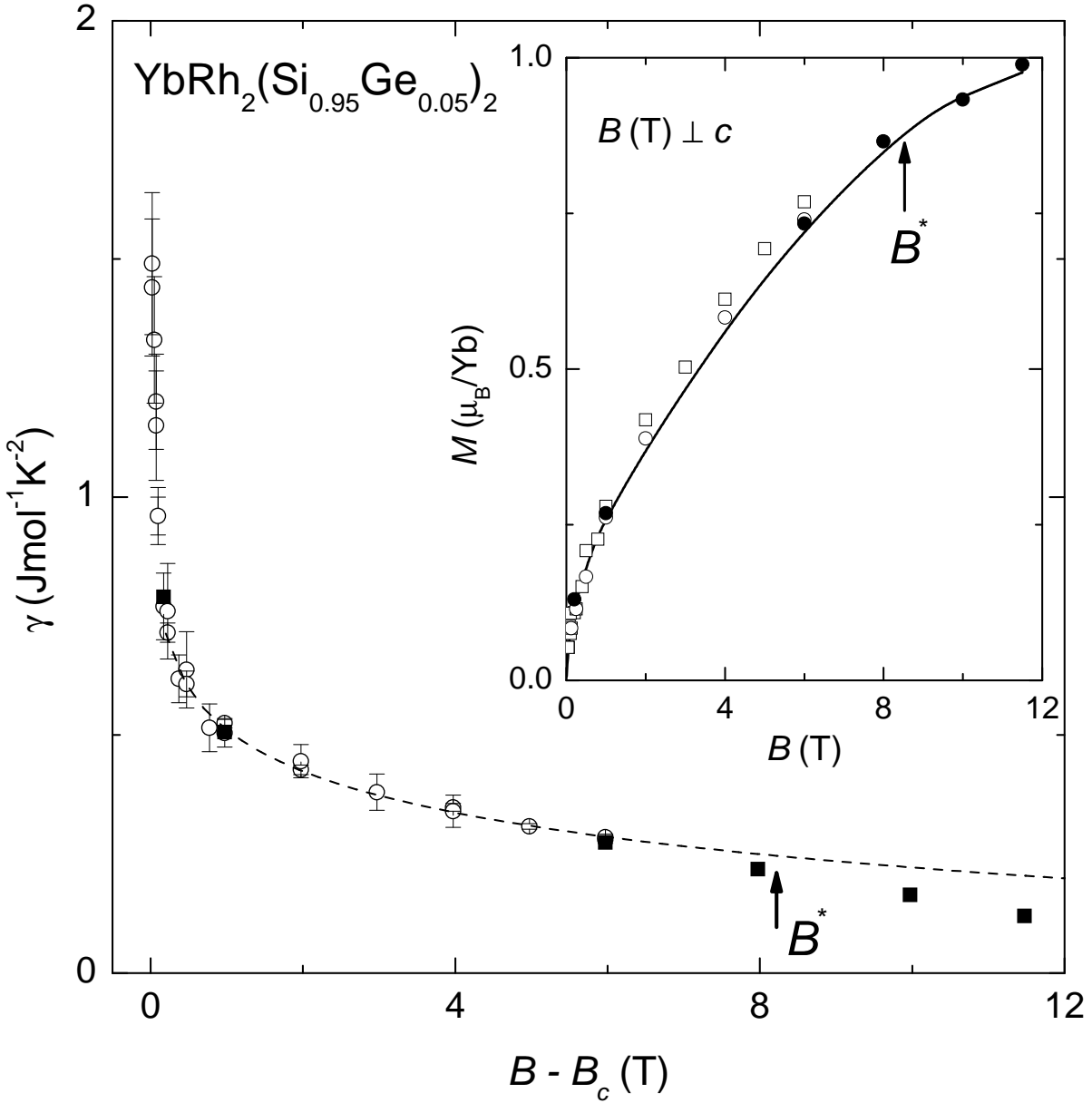
Figure 4.2: *Magnetic–field dependence of* $\gamma = \Delta C(T)/T$ *for* $T \rightarrow 0$ *of* $YbRh_2(Si_{0.95}Ge_{0.05})_2$. $B_c = 0.027$ *T is the critical field. Data depicted as open symbols are taken from Ref. [56]. Inset: Field dependence of calculated (open symbols [56]) and measured magnetisation (solid line [56]) at 40 mK. The slope of* $M(B)$ *changes at* $B^* \approx 8.5$ *T.*

4.2.2 Yb$_{1-y}$La$_y$Rh$_2$Si$_2$ ($y = 0.05, 0.1$)–"field" and "substitution–induced" LFL behavior

The single–crystalline platelets were grown from In flux, using the sealed Ta-crucible technique [85]. X–ray powder–diffraction patterns showed single–phase samples with the proper ThCr$_2$Si$_2$ tetragonal structure (space group $I4/mmm$). Of particular interest are the low substitution contents $y = 0.05$ and 0.1 with the residual resistivities 7.6 and 12 $\mu\Omega$cm, respectively. The lattice parameters are presented in table 4.1. Here presented are the results of specific heat on samples of this nominal stoichiometry with masses $m = 3.28$ mg and 6.79 mg, respectively. A microprobe analysis yields that these samples contain an effective La content slightly larger than the (nominal) starting concentration [85]. In the following, however, we use the nominal concentration for the presentation of the results.

compound	content	a (Å)	c (Å)	V (Å^3)
Yb$_{1-y}$La$_y$Rh$_2$Si$_2$	$y = 0$	4.007(5)	9.858(5)	158.4(4)
	$y = 0.05$	4.012(5)	9.863(5)	158.7(5)
	$y = 0.1$	4.013(5)	9.875(5)	159.1(5)
YbIr$_2$Si$_2$		4.032(5)	9.826(5)	159.741(5)

Table 4.1: *Lattice parameters for Yb$_{1-y}$La$_y$Rh$_2$Si$_2$ ($y = 0, 0.05, 0.1$) and YbIr$_2$Si$_2$ [85, 86].*

The specific–heat results in zero field below 2 K (normalized to Yb-moles) on a logarithmic T scale are plotted in Fig. 4.3. $\Delta C(T)/T = (C - C_{nuc})/T$ represents the specific–heat after subtraction of the nuclear quadrupol contribution, with $\alpha_Q = 20 \times 10^{-6}$ JKmol^{-1} and $\alpha_Q = 55 \times 10^{-6}$ JKmol^{-1} for y = 0.05 and y = 0.1, respectively. α_Q is obtained graphically as described in the previous section. The specific heat of LuRh$_2$Si$_2$ (see inset of Fig. 4.3) is less than 3% below 5 K. Therefore, in the following we neglect the contribution of phonons in our data. No evidence of AFM order was

observed for both compounds down to 0.03 K.

The zero-field properties of the two Yb$_{1-y}$La$_y$Rh$_2$Si$_2$ compounds (Fig. 4.3) are essentially identical to those of YbRh$_2$(Si$_{0.95}$Ge$_{0.05}$)$_2$. Below 2 K $\Delta C(T)/T$ exhibits a logarithmic increase down to 0.25 K (dashed lines in Fig. 4.3), with only a minor increase (~ 0.1 J/molK^2) of the normalized values at low temperature for the sample with 10% La. Similar to YbRh$_2$(Si$_{0.95}$Ge$_{0.05}$)$_2$ this logarithmic increase follows the relation $\Delta C/T \propto \gamma_0 \ln(T_0/T)$ with $\gamma_0 = 0.116$ J/molK^2 and $T_0 = 20$ K for $y = 0.05$ and $\gamma_0 = 0.131$ J/molK^2 and $T_0 = 22$ K for $y = 0.1$, respectively. Below $T = 0.25$ K the data show a stronger than logarithmic quasiparticle mass divergence. A power–law fit $\Delta C(T)/T \propto T^{-n}$ through the experimental data for 0.05 K $\leq T \leq 0.2$ K yields $n = -0.51 \pm 0.06$ and $n = -0.40 \pm 0.05$ for $y = 0.05$ and 0.1, respectively (solid lines in Fig.4.3). For the sample with 10% La the exponent has a smaller absolute value, but the fitting range is also smaller, 0.07 K $\leq T \leq 0.2$ K, since the LFL behavior is already observed below 65 mK. For $y = 0.05$ our measurements show that saturation takes place at very low temperatures in $\Delta C(T)/T$, below ~ 0.04 K, which suggest that the LFL behavior occurs below this temperature. Recent resistivity measurements [87] on this system, show a slight deviation from the linear temperature dependence in the same temperature range, but no T^2 behavior like expected for a LFL state was observed.

The low-temperature specific heat divided by temperature saturates for both compounds and the Sommerfeld coefficient decreases rapidly with increasing La content, indicating that the quasiparticle mass decreases with increasing La content in the LFL state. To estimate the evolution of $T_K(y)$ the magnetic entropy was used, as shown in the inset of Fig. 4.3, obtained by integrating our magnetic specific–heat data. The high–temperature specific–heat measurements are reported in Ref. [85]. With the assumption that 50% of Rln 2 is reached at about one half of the Kondo temperature [88] we found that $T_K(y = 0.05) \approx 20$ K and $T_K(y = 0.1) \approx 22$ K. Thus, the Kondo temperature T_K increases as expected since the increase of the volume leads to an evolution of the Yb from a trivalent towards a valence–fluctuating state [85].

Small magnetic fields have a strong influence on the low–temperature $\Delta C/T$ vs T be-
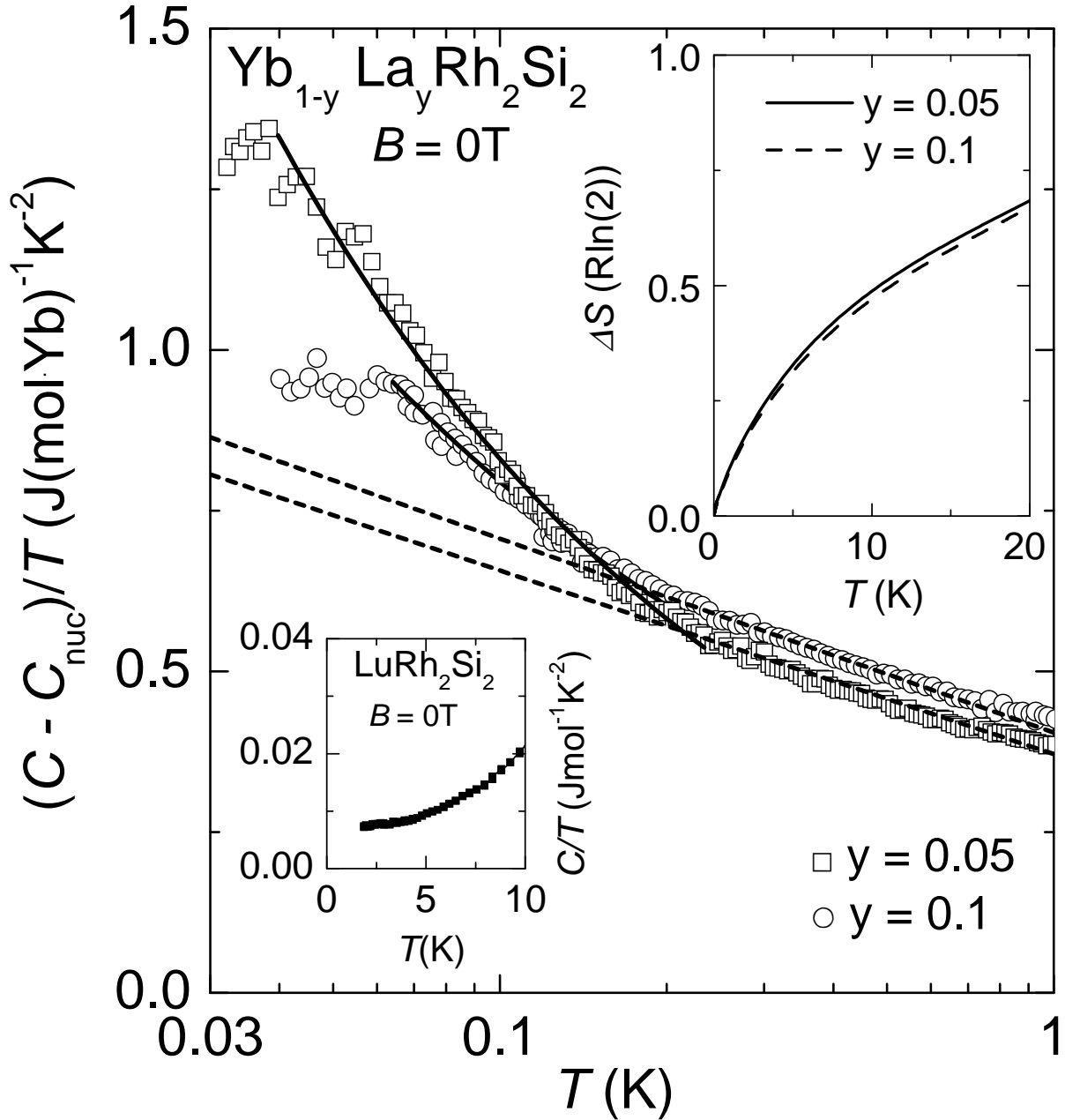
Figure 4.3: *Comparison of the low-temperature $B = 0$ T electronic specific heat of $Yb_{1-y}La_yRh_2Si_2$ single crystals with $y = 0.05$ (open squares) and 0.1 (open circles). The solid lines are power–law fits through the data. The dashed lines separate the logarithmic from the "upturn" region in $\Delta C/T = (C - C_{nuc})/T$. Inset–top shows the normalized electronic entropy ΔS employed to calculate the single–impurity Kondo temperature (see text); inset–bottom: $C(T)/T$ of $LuRh_2Si_2$ to estimate the phonon contribution.*
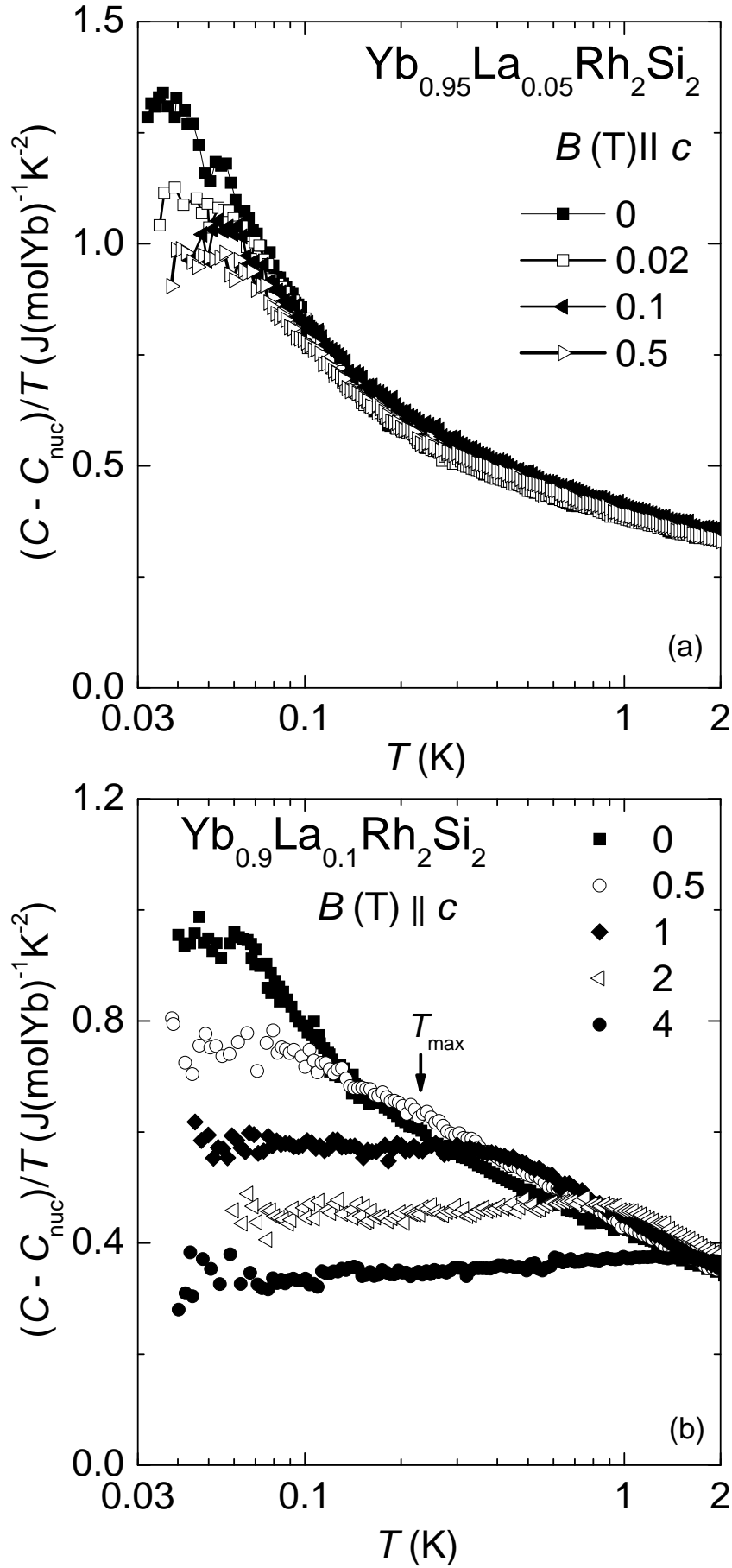
Figure 4.4: *Electronic specific heat of Yb$_{1-y}$La$_y$Rh$_2$Si$_2$ divided by temperature in various magnetic fields parallel to the c axis for y = 0.05* **(a)** *and y = 0.1***(b)***.*

havior (Fig. 4.4). The graphically determined $\alpha(B)$ values used to subtract the Zeemann contribution from the measured specific heat are listed in Table 4.3 presented in the appendix of this chapter. In the following we focus only on the obtained low–temperature electronic specific heat.

For the $y = 0.05$ data (Fig. 4.4 (a)) the saturation is clearly visible below ~ 0.05 K in a field as small as 20 mT. When increasing the field to $B = 0.5$ T the establishment of a LFL phase is observed, i.e., the data show $\Delta C(T)/T \simeq$ const below 0.07 K. The zero–field data for $y = 0.1$ already show similar LFL behavior below 0.07 K (Figure 4.4 (b)). The extension of the LFL region increases with further increasing the field. Similar to $YbRh_2(Si_{0.95}Ge_{0.05})_2$, a weak maximum emerges in $\Delta C(T)/T$ which broadens and shifts to higher temperature upon raising field (Fig. 4.4 (b)). This indicates that entropy is transferred from the low–temperature increment to higher temperatures by the application of field. The LFL state forms for temperatures well below this maximum.

4.2.3 $YbIr_2Si_2$–a new nonmagnetic HF system

Depending on synthesis conditions, $YbIr_2Si_2$ crystallizes either in the body-centered $ThCr_2Si_2$ structure (I–type) or primitive tetragonal $CaBe_2Ge_2$ structure (P–type). Both are ordered variants of the $BaAl_4$ structure type differing by the interchange of one Ir– and one Si–layer. Both types of crystals were grown by slightly changing the Yb content in the starting composition. A slight excess (10%) of Yb favors the primitive structure while a stoichiometric starting composition produces the body–centered structure. The occurrence of these two different structures in RIr_2Si_2 is well documented for other rare–earth elements R [89]. Measurements reported here were performed on a high–quality single crystal of I–type $YbIr_2Si_2$, with a typical residual resistivity $\rho_0 \sim 0.5$ $\mu\Omega$cm and $RRR > 200$.

Recent results on the new Yb–based HF compound $YbIr_2Si_2$ [86] suggested that I–type $YbIr_2Si_2$ has a nonmagnetic ground-state being thus on the paramagnetic side of the QCP. Ir is located just below Rh in the periodic table, has thus the same chemical valence but is slightly larger. This makes I–type $YbIr_2Si_2$ an ideal complement of $YbRh_2Si_2$ for

the investigation of the QCP. A magnetically non-ordered Fermi-liquid ground state is also supported by the results of specific heat and susceptibility at low temperatures. In Fig. 4.5 the electronic specific heat of YbIr$_2$Si$_2$ is plotted as $\Delta C/T$ versus $\log T$ in various magnetic fields. $\Delta C(T)$ is obtained by subtracting $C(T)$ of LuIr$_2$Si$_2$ and a nuclear contribution $C_Q = \alpha_Q/T^2$ with $\alpha_Q = 80 \times 10^{-6}$ JKmol^{-1} below 200 mK.

The graphically determined $\alpha(B)$ values are listed in Table 4.3 in the appendix. Down to 0.4 K, $\Delta C/T$ increases logarithmically with decreasing temperature, following a relation $\Delta C/T \propto \gamma_0 \ln(T_0/T)$ with $\gamma_0 = 0.082$J/molK^2 and the characteristic temperature $T_0 = 44$ K. This is quite similar to the behavior observed in YbRh$_2$Si$_2$, where the logarithmic increase leads to a $\Delta C/T$ value at 0.4 K twice as large as in the Ir–based compound and a much lower T_0 (24 K). However, in contrast to the temperature dependence observed in YbRh$_2$Si$_2$ where the increase in $\Delta C/T$ gets more pronounced below 0.3 K, ending up in a sharp and large peak at $T_N = 70$ mK, we observe in YbIr$_2$Si$_2$ a saturation of $\Delta C/T$ below 0.4 K, at a Sommerfeld coefficient $\gamma = 0.37$ J/molK^2. The crossover from the NFL logarithmic increase above 0.4 K to the LFL behavior below 0.4 K is quite abrupt. Such a crossover from a NFL-logarithmic increase to a constant C/T value has been observed in YbRh$_2$Si$_2$ in a magnetic field large enough to suppress the AF state. The magnetic entropy reaches 0.5Rln 2 at 20 K, giving a first estimate for the Kondo temperature, $T_K = 40$ K. This is in surprisingly good agreement with the value for the spin–fluctuation temperature $T_0 = 44$ K and almost twice the value deduced for YbRh$_2$Si$_2$. The extension of the LFL region increases upon applying fields.

The inset of Fig. 4.5 shows the temperature dependence of the magnetization M [90] taken at $B = 1$ T and at low temperatures, down to 50 mK. $\chi(T) = M/B$ continues to increase down to 0.4 K, but the increase amounts only to 15%, i.e., much less than in YbRh$_2$Si$_2$. Below 0.4 K, the susceptibility shows a tendency to saturate, a further signature of LFL behavior. Compared to the specific–heat results, the crossover from an increasing $\chi(T)$ to the almost constant value $\chi_0 = 5.25 \times 10^{-2}$ emu/mol is rather smooth. This crossover, which in the specific heat is more sudden than in typical Ce–based HF systems such as CeRu$_2$Si$_2$, might be an intrinsic property of Yb systems
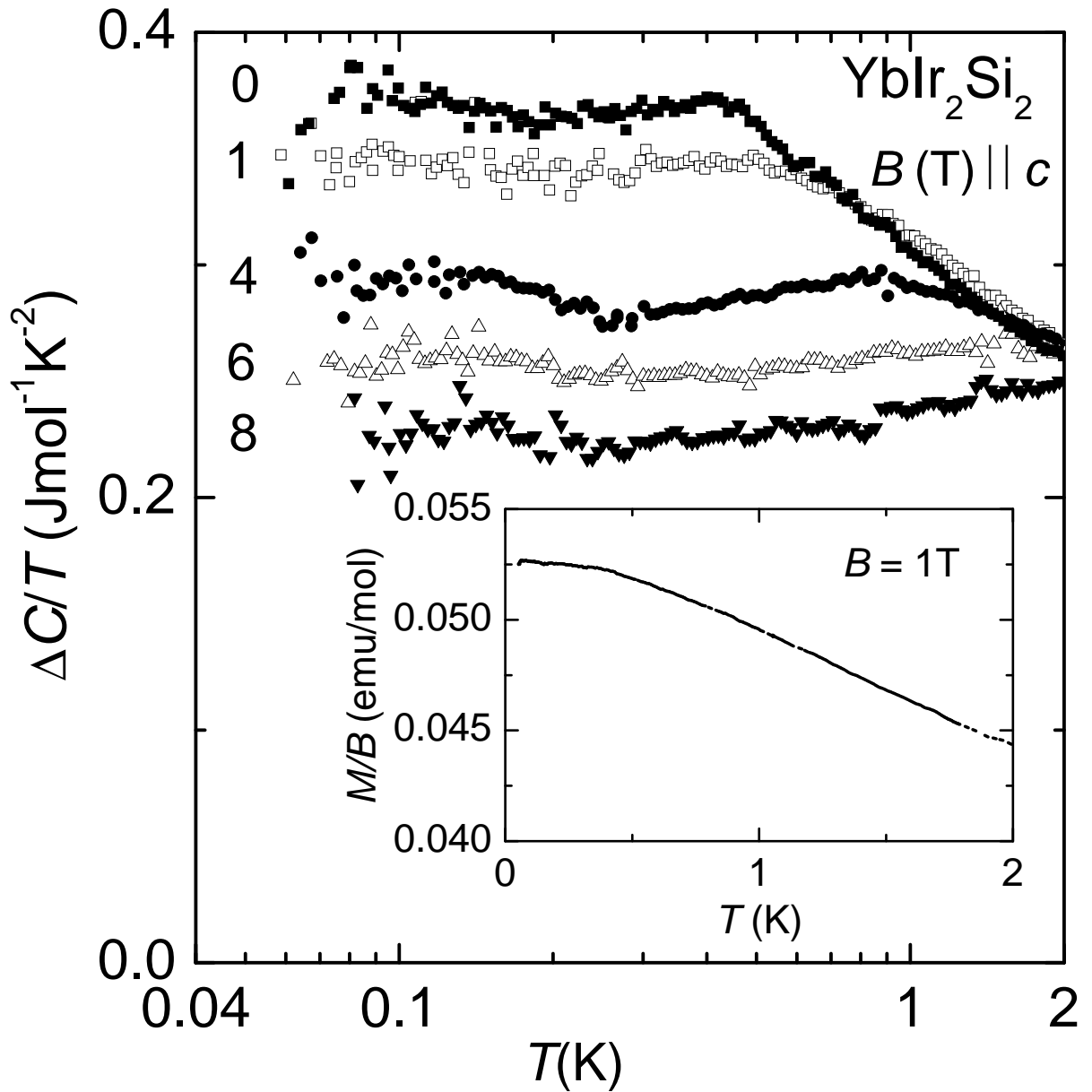
Figure 4.5: *Electronic specific heat divided by temperature, $\Delta C/T$, in various magnetic fields parallel to the c axis. Inset: Magnetic susceptibility at low temperatures [90]. Note the tendency to saturation below 400 mK.*

connected with the smaller extent of the f–wave function in Yb and thus a more localized character. However, we cannot exclude the possibility that the broad kink in $C(T)$ is due to a very small amount of P–type phase with a broadened magnetic transition around 0.4 K. We can exclude this broad kink to originate from an intrinsic magnetic transition in I-type YbIr$_2$Si$_2$, because with such a high RRR one expects to observe a sharp transition, sharper than that observed in YbRh$_2$Si$_2$ with an RRR of 30–60. Furthermore, no anomaly was observed in $\rho(T)$ [86].

4.2.4 Discussion

First we discuss the results of the specific–heat measurements of the Yb compounds in zero field. Fig. 4.6 shows $\Delta C(T)/T$ vs. T on a semilogarithmic plot below 3 K for the above–mentioned compounds. The stoichiometric HF compound YbRh$_2$Si$_2$ orders antiferomagnetically at $T_N = 0.07$ K. Above $T \simeq 0.1$ K, the anomalous behavior with respect to the LFL theory was observed in a wide temperature range. It was shown that these NFL effects are attributed to strong quantum–critical fluctuations which originate from a nearby zero–temperature magnetic instability and are not caused by disorder effects.

For YbRh$_2$(Si$_{0.95}$Ge$_{0.05}$)$_2$ an AFM transition occurs at $T_N \approx 20$ mK (Fig. 4.6) [56]. However, in La–substituted systems no AFM transition was found down to the lowest accessible temperature in agreement with resistivity measurements [87]. Moreover, the 5% La–doped YbRh$_2$Si$_2$ already shows a tendency to saturation in $\Delta C(T)/T$ below 40 mK at a Sommerfeld coefficient $\gamma \simeq 1.35$ JK^{-2}mol^{-1}, one of the highest values among magnetically non–ordered Yb systems, suggestive of a LFL ground state in this compound. Furthermore, for 10% La–doped YbRh$_2$Si$_2$ we observe below 70 mK saturation of $\Delta C/T$ indicating clearly a LFL state for this concentration. For YbIr$_2$Si$_2$, $\Delta C(T)/T$ saturates below ~ 0.5 K upon cooling to a value of $\gamma = 0.372$ JK^{-2}mol^{-1}. Thus, I–type YbIr$_2$Si$_2$ is found to be placed on the nonmagnetic site of the QCP, in contrast to its Rh–homologue which is just on the magnetically ordered side.

It is worth noting that more than a log–T increase upon decreasing temperature, ($T <$

0.250 K), is observed in the specific heat for $YbRh_2(Si_{1-x}Ge_x)_2$ and $Yb_{1-y}La_yRh_2Si_2$. This is one of the hallmarks of the NFL behavior in pure $YbRh_2Si_2$ where a continuous increase of $C(T)/T$ below 10 K was reported, with a logarithmic temperature dependence between 10 K and 0.2 K followed by a much stronger increase at lower temperature [37].

The substitution with La corresponds to a relative change of the unit-cell volume $\Delta V/V(y = 0.05) = 0.34 \pm 0.08$ % and $\Delta V/V(y = 0.1) = 0.49 \pm 0.07$ % with $V(y = 0) = 158.4 \pm 0.2$ Å at room temperature. This expansion of the unit-cell volume of $YbRh_2Si_2$ drives the system through the QCP already to the non-magnetic site as shown in our specific–heat data.

The unit–cell volume dependence of the $\Delta C(T)/T|_{T=0.04\ K}$ for the Yb–compounds discussed here is shown in Fig. 4.7 for $B = 0$. Starting from the AFM side, for $YbRh_2(Si_{0.95}Ge_{0.05})_2$ $\Delta C/T$ at $T = 0.04$ K has a slightly smaller value than that observed in the pure sample. With further increasing V, for $Yb_{1-y}La_yRh_2Si_2$, the AFM order is absent and the systems are situated in the vicinity of the QCP on the nonmagnetic side. The values of $\Delta C(T)/T|_{T=0.04\ K}$ decrease with increasing unit–cell volume indicating that the quasiparticle mass decreases with increasing La content in the LFL state consistent with the increase in T_K. $YbIr_2Si_2$ has a nonmagnetic ground state being thus on the nonmagnetic side of the QCP. For this system γ is smaller than for $Yb_{0.9}La_{0.1}Rh_2Si_2$ ($T_K \simeq 44$ K). With increasing V, the behavior of $\Delta C/T(V)$ for $YbRh_2(Si_{1-x}Ge_x)_2$ can be correlated with what we would expect to have in $\Delta C/T(V)$ at the QCP, specially in the case of the LM scenario. With the control parameter lattice volume, V, $\Delta C/T(V)$ is expected to diverge at a critical volume. Fig. 4.7 indeed shows that $\Delta C/T(V)$ increases upon approaching the QCP from the AFM side and above a critical volume, V_c decreases rapidly with further increasing V.

Figure 4.8 shows the electronic specific–heat coefficient γ versus magnetic field B for all the compounds discussed in this section. To fit $\gamma(B)$ of $Yb_{0.95}La_{0.05}Rh_2Si_2$ with a power law, $\gamma \propto 1/(B - B_c)^\alpha$, one has to assume a negative critical field $B_c = -0.03$ T. This yields $\alpha = -0.050 \pm 0.01$ which does not correspond to the value obtained from
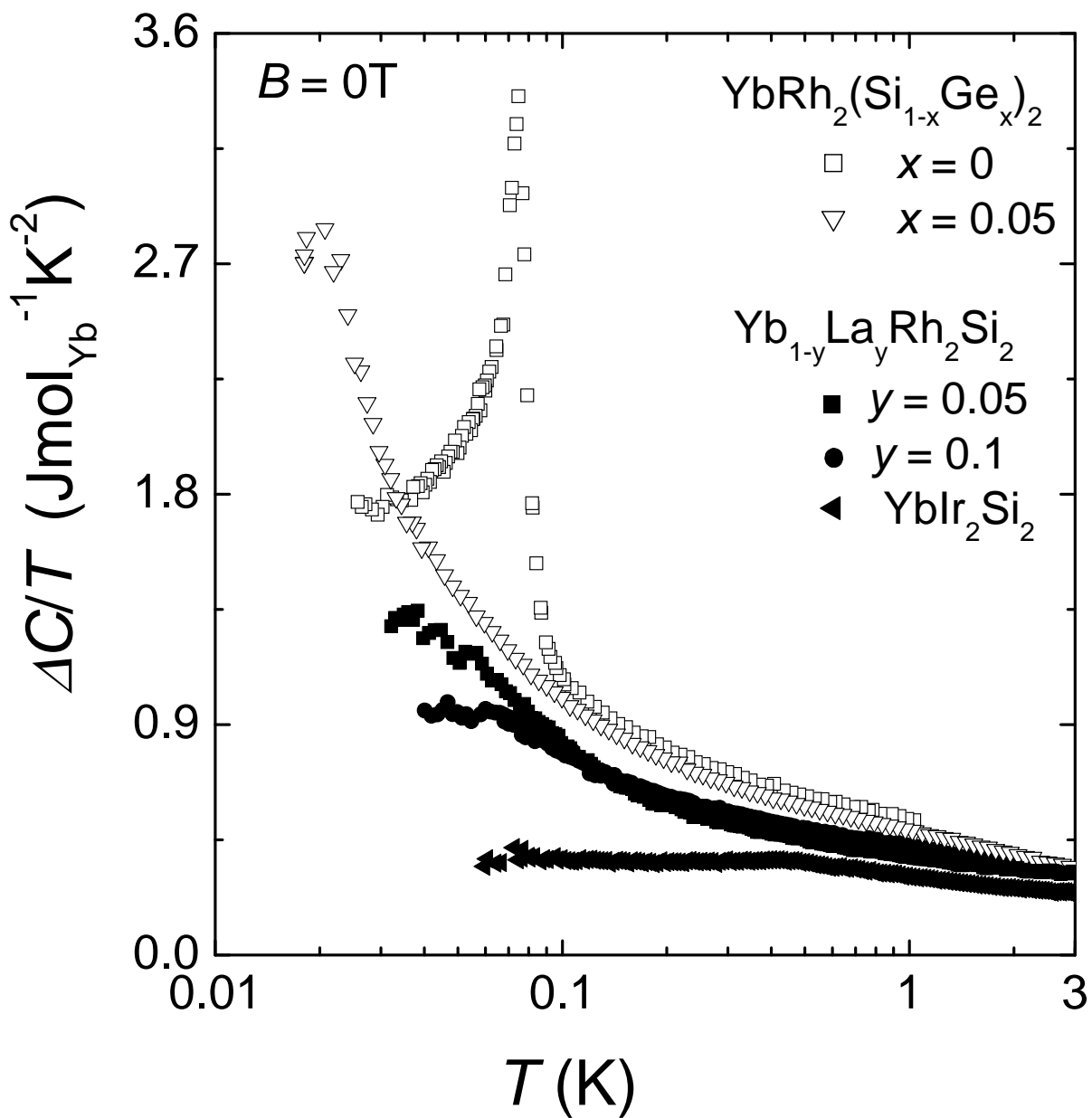
**Figure 4.6:** *Temperature dependence of the electronic specific heat of YbRh$_2$(Si$_{1-x}$Ge$_x$)$_2$ [91], Yb$_{1-y}$La$_y$Rh$_2$Si$_2$, and YbIr$_2$Si$_2$ normalized to the Yb content plotted as $\Delta C/T$ vs T in a semilogarithmic scale.*
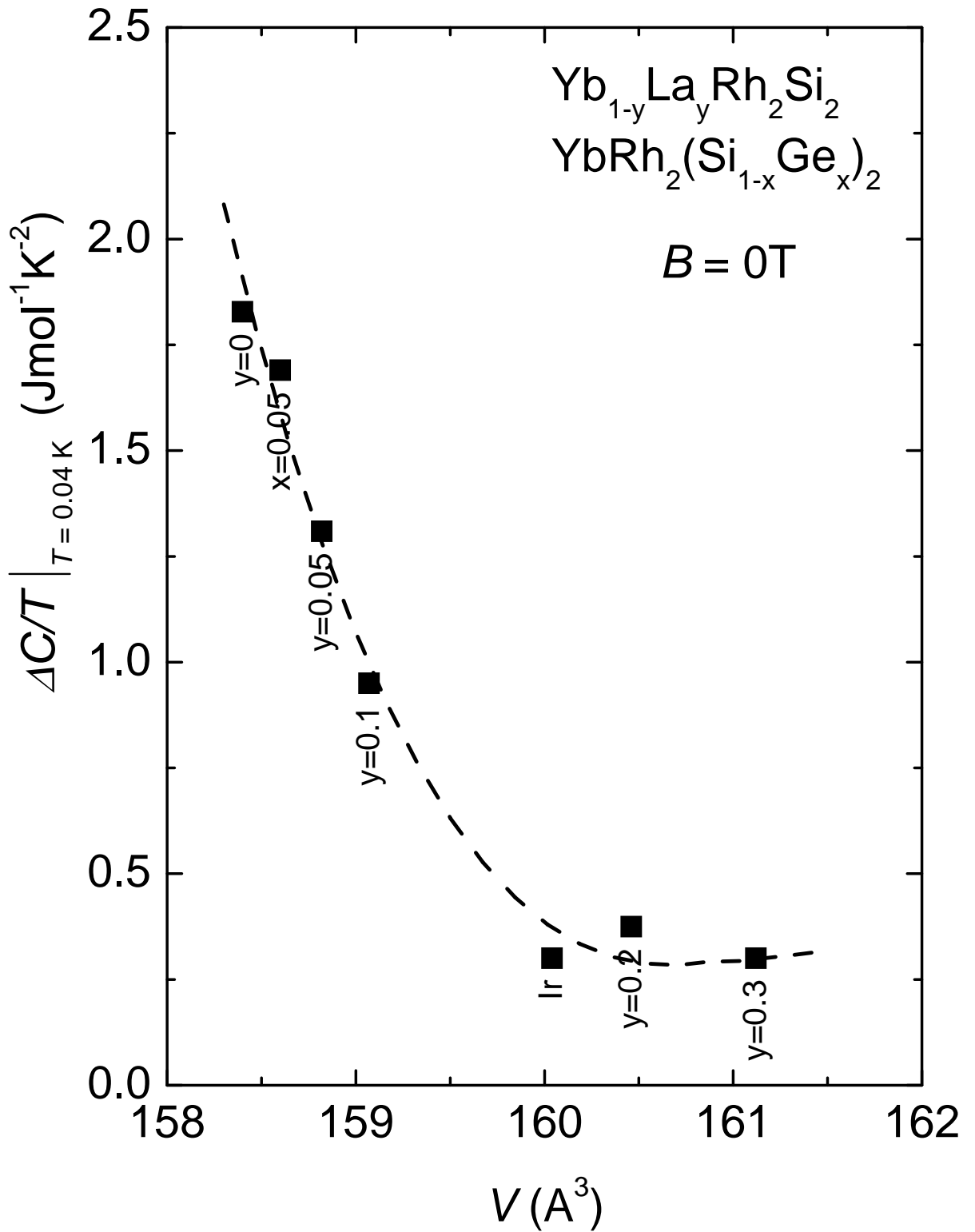
Figure 4.7: *The values of the electronic specific–heat, $\Delta C/T$, at $T = 0.04$ K for $Yb_{1-y}La_yRh_2Si_2$, $YbRh_2(Si_{0.95}Ge_{0.05})_2$, and $YbIr_2Si_2$ from the data plotted in Fig. 4.6 for $B = 0$ T versus unit–cell volume. To complete the picture additional data for $y = 0.2$ and 0.3 were included [85]. The dashed lines are guides to the eye.*
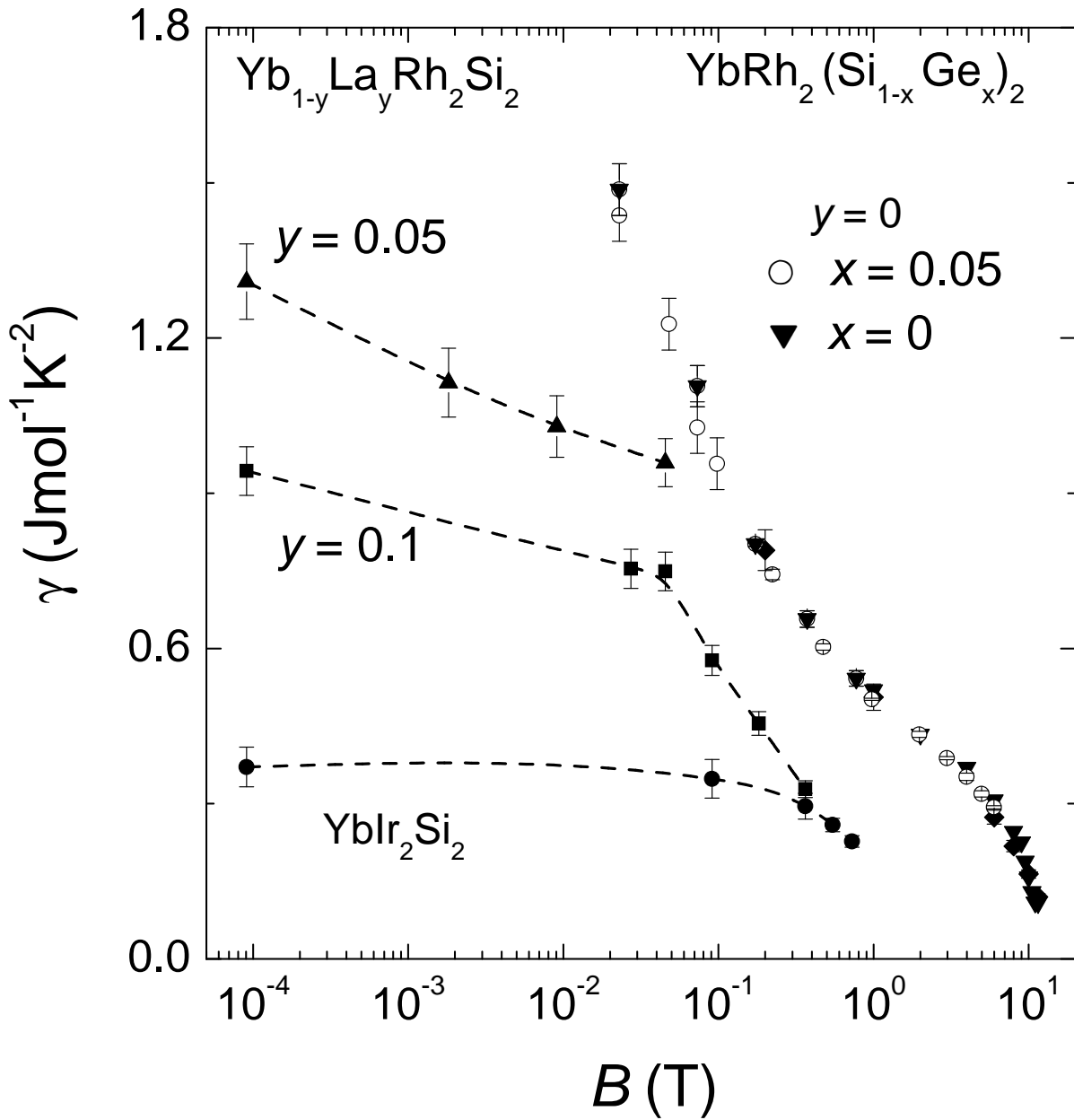
Figure 4.8: *Electronic specific–heat coefficient, $\gamma = C_{el}(T)/T|_{T\to 0}$, of $Yb_{1-y}La_yRh_2Si_2$,*
YbRh$_2$(Si$_{1-x}$Ge$_x$)$_2$, and YbIr$_2$Si$_2$ in various magnetic fields, B, applied parallel to the
crystallographic c axis. The dashed lines are guides to the eye.

the low–temperature dependence of the electronic specific–heat coefficient, $\gamma(T) \propto T^n$ at $B = 0$ ($n = -0.51$) (Fig. 4.3).

Furthermore, Fig. 4.8 emphasizes that the $Yb_{0.95}La_{0.05}Rh_2Si_2$ compound shows a much weaker divergence of γ at low fields in comparison with $YbRh_2(Si_{1-x}Ge_x)_2$. This field dependence becomes even weaker for $Yb_{0.9}La_{0.1}Rh_2Si_2$ which shows clearly LFL behavior below 70 mK. In Fig. 4.8, the nonmagnetic $YbIr_2Si_2$ shows an almost field–independent γ value. Our results provide the evidence for I–type $YbIr_2Si_2$ to be an Yb–based HF compound with a magnetically non–ordered LFL ground state below $T = 0.4$ K and a Sommerfeld coefficient $\gamma = 370$ mJK^{-2}mol^{-1}. The NFL–like behavior observed above 0.5 K and its similarity to that reported in $YbRh_2Si_2$ suggest that the Ir compound is rather close to the QCP.

4.3 $CeIn_{3-x}Sn_x$: a cubic HF alloy

$CeIn_{3-x}Sn_x$ crystallizes in the cubic Cu_3Au structure (see Fig. 4.9, inset). At ambient pressure, $CeIn_3$ orders in an antiferromagnetic structure below a Néel temperature of about $T_N = 10.2 \pm 0.1$ K [59, 92, 93, 94]. The magnetic structure is that of a simple antiferromagnet with a propagation vector $\mathbf{Q}^* = (\frac{1}{2},\frac{1}{2},\frac{1}{2})$, i. e., the Ce moments are aligned antiferromagnetically in adjacent (111) ferromagnetic planes [95]. The room–temperature valency of the Ce atom reveals a value close to 3 [96]. Due to Kondo screening the ordered magnetic moment μ_{ord} in the antiferromagnetic state is substantially reduced, $\mu_{\mathrm{ord}} \approx 0.5\mu_{\mathrm{B}}$, compared to the calculated value of $0.71\mu_{\mathrm{B}}$, when assuming a Γ_7 ground–state doublet and $J = 5/2$ [95, 97].

Opposite to the larger volume of nonmagnetic Yb^{2+} compared to the magnetic Yb^{3+}, the ionic volume of the nonmagnetic Ce^{4+} ($4f^0$, $J = 0$) is smaller than that of the magnetic Ce^{3+} state ($4f^1$, $J = 5/2$). Thus, by applying an external pressure on $CeIn_3$, T_N can be driven to $T = 0$. Hydrostatic–pressure experiments on $CeIn_3$ revealed a critical pressure of $p_c \approx 2.6$ GPa [59] which is relatively high, and therefore, no specific–heat measurements have been performed yet. For such large pressures, the influence of

pressure gradients cannot be neglected. Alternatively, the AFM transition temperature can be lowered by chemical doping. By this method, both volume and electronic–density modifications can be induced depending on the substitute. In the case of CeIn$_{3-x}$Sn$_x$, both variations are driven; the random replacement by Sn on the In lattice sites increases both, the unit–cell volume and the number of electrons [92]. The additional p electrons induce hybridization effects in the ground state and excited crystal–electrical–field states and eventually quench the magnetic moment of the cerium [98].

The magnetic (x, T) phase diagram of polycrystalline CeIn$_{3-x}$Sn$_x$ (Fig. 4.9) has been widely studied for $T > 0.4$ K and $0 \leq x \leq 3$ [93, 95, 99, 100, 101]. These previous investigations were mainly focused on the development of the valence transition from magnetic CeIn$_3$ to an intermediate valence state in CeSn$_3$ [93, 95, 101]. It was shown, that the valence fluctuations of the Ce atoms induced by Sn substitution take place for $x \geq 2.2$ and can be neglected in the region $x < 1$ which we are interested in. A disadvantage of alloying is that, with increasing doping level, more disorder is introduced. It is worth noting that the quality of CeIn$_{3-x}$Sn$_x$ single crystals investigated here, with $RRR \sim 1 - 3$, is expected to be significantly different from those of YbRh$_2$(Si$_{1-x}$Ge$_x$)$_2$, discussed in the previous section, or CeNi$_2$Ge$_2$ for which a residual resistivity ratio $RRR \sim 400$ [72] was reported.

However, the observed decrease of T_N with increasing Sn content (Fig. 4.9) over more than two decades in temperature from ~ 10 K for CeIn$_3$ to ~ 0.1 K for CeIn$_{2.35}$Sn$_{0.65}$ [103] exceeds the temperature range of $T(p)$ which was observed upon applying an external pressure on CeIn$_3$ [104, 105], indicating that the disorder introduced by doping in this system does not play an important role with respect to magnetism.

4.3.1 Non-Fermi-liquid behavior

A first report of Pedrazzini $et\ al.$ [100] showed pronounced NFL effects in specific–heat and resistivity experiments for polycrystalline samples with a Sn content of $x = 0.6$ and $x = 0.7$. From their results a critical concentration of $x_c \approx 0.65$ has been determined at which T_N vanishes. The electronic specific heat for $x = 0.6$ showed a
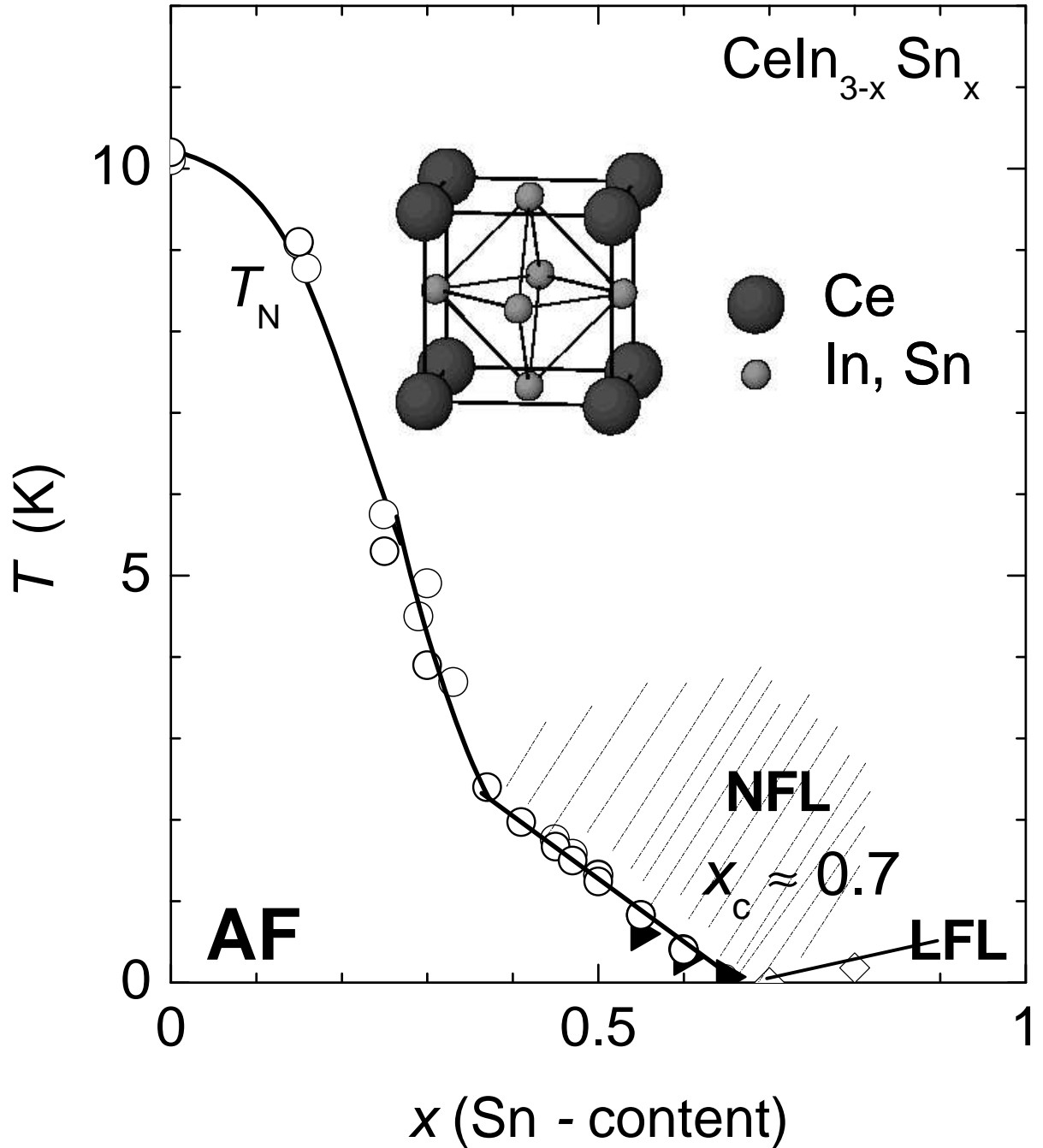
Figure 4.9: *T–x phase diagram of $CeIn_{3-x}Sn_x$ for $x \leq 1$. Open diamonds mark T^*, the upper limit of $\Delta C/T \sim const$ and $\Delta\rho(T) \propto T^2$ behavior (LFL) respectively [100, 102]. Open circles denote T_N reported in Ref. [103]. The closed symbols denote T_N obtained in the present investigation. Inset: crystal structure of $CeIn_{3-x}Sn_x$*

logarithmic behavior, $C(T)/T = a \log(T_0/T)$ with $a = 0.5$ Jmol^{-1}K^{-2} and $T_0 = 16$ K within the temperature interval 0.4 K $\leq T \leq 8$ K. The $x = 0.7$ sample also shows a logarithmic dependence, although $C_{\text{el}}(T)/T$ starts to flatten at low temperatures [106]. The measurements, however, were performed down to $T \approx 0.4$ K only. Low–temperature specific–heat measurements performed by T. Cichorek on a polycrystalline sample with $x = 0.7$ showed that the departure of $C(T)/T$ from the logarithmic behavior extends down to 0.1 K with a $C_{\text{el}}(T)/T \propto \gamma_o - b\sqrt{T}$ dependence, after the subtraction of a hyperfine nuclear contribution due to the In [107].

Moreover, resistivity measurements on polycrystalline CeIn$_{3-x}$Sn$_x$ demonstrate that T_{N} vanishes at a critical Sn content of $x_c \simeq 0.7$ [107]. For this particular concentration it was observed that the resistivity decreases linearly with decreasing temperature over much more than one order of magnitude, 0.02 K$\leq T \leq 0.8$ K. Similar $\Delta\rho(T)$ behavior was reported for CeCu$_{5.9}$Au$_{0.1}$ which displays strong anisotropic critical fluctuations [70]. This should not be the case for CeIn$_{3-x}$Sn$_x$, where the spin fluctuations are expected to develop in an isotropic environment due to its cubic crystal structure. However, the experimentally observed behavior, $\Delta\rho(T) \propto T$, is in contradiction with the 3D SDW prediction and, in addition, with Rosch's predictions for the effect of disorder [33] which show that for very clean samples, $RRR > 100$, $\Delta\rho(T) \propto T^\epsilon$ with $\epsilon \to 1$. The samples we discuss here are characterized by $RRR \sim 1$. Therefore, the low–temperature behavior should show $\Delta\rho(T) \propto T^\epsilon$ with $\epsilon \simeq 1.5$ [33]. Surprisingly, resistivity measurements on clean CeIn$_3$ ($RRR \sim 300$) under pressure [104] revealed $\Delta\rho(T) \propto T^{1.5}$. Based on these experiments and the theoretical predictions, one might explain the resistivity results obtained for CeIn$_{2.3}$Sn$_{0.7}$ [107] by assuming that the critical spin fluctuations are 2D [108]. Inelastic neutron–scattering experiments are necessary to shed light on the true magnetic fluctuation spectrum in this system.

Recently, measurements of the thermal expansion, $\beta(T)$, were performed [71] on new single crystals CeIn$_{3-x}$Sn$_x$ in the vicinity of the QCP since recent theoretical work [109] has shown that (i) the Grüneisen ratio, $\Gamma \propto \beta/C$, where C denotes the specific heat and β the volume expansion coefficient, is divergent as T goes to zero at any QCP and (ii)

the associated critical exponent can be used to differentiate between different types of QCP. It is shown that the thermal expansion for $CeIn_{2.3}Sn_{0.7}$ and $CeIn_{2.35}Sn_{0.65}$ can be well described in the temperature range 50 mK $\leq T \leq$ 1.3 K ($x = 0.65$) and 50 mK $\leq T \leq$ 1 K ($x = 0.7$), respectively, with the prediction for the 3D SDW scenario, in contrast to the conclusion drawn from resistivity experiments.

In this chapter, we present specific–heat measurement on single crystals of $CeIn_{3-x}Sn_x$ from the same generation with those in Ref. [71] close to the QCP, ($x = 0.55, 0.6, 0.65, 0.7, 0.8$), in the temperature range 40 mK $< T <$ 4 K and in magnetic fields up to $B = 12$ T. Our aim was to analyze the low temperature behavior of the specific heat very close to a QCP in order to clarify the reported discrepancy between $\rho(T)$ and $\beta(T)$ results.

4.3.2 Concentration–tuned QCP

The temperature dependence of $\Delta C/T \equiv (C - C_Q)/T$, measured at $B = 0$, of all samples studied in this work is shown in Fig. 4.10. The electronic contribution, ΔC, to the specific heat is obtained by subtracting from the total specific heat, $C(T)$, the nuclear quadrupole contribution of indium, $C_Q = \alpha_Q/T^2$ below $T < 150$ mK. The phonon contribution is negligible below 4 K [100]. The value of α_Q was obtained from the $T = 0$ intercept of the plot CT^2 vs. T^3 for each sample. The results show that the AFM transition indicated by arrows in Fig. 4.10, has a clear evolution as a function of Sn concentration.

For $x = 0.55$ the kink in $\Delta C/T$ at $T = 0.60 \pm 0.02$ K marks the onset of magnetic order. The value of T_N is always defined as the inflection point of the $\Delta C/T$ vs T data. At higher Sn content, $x = 0.60$, the signature of the magnetic order becomes less pronounced and occurs at lower temperature $T_N = 0.3 \pm 0.01$ K. A strong increase of $\Delta C/T$ for $T \to 0$ is observed for $x = 0.60$ indicating the importance of critical spin fluctuations close to the QCP. Above T_N, both samples with $x = 0.55$ and $x = 0.6$, reveal a $\Delta C/T \propto -\log T$ behavior. For a sample with a higher Sn content, $x = 0.65$, the AFM transition temperature is further reduced. For this nominal concentration, which denotes the starting composition of the crystal growth, we measured two samples:
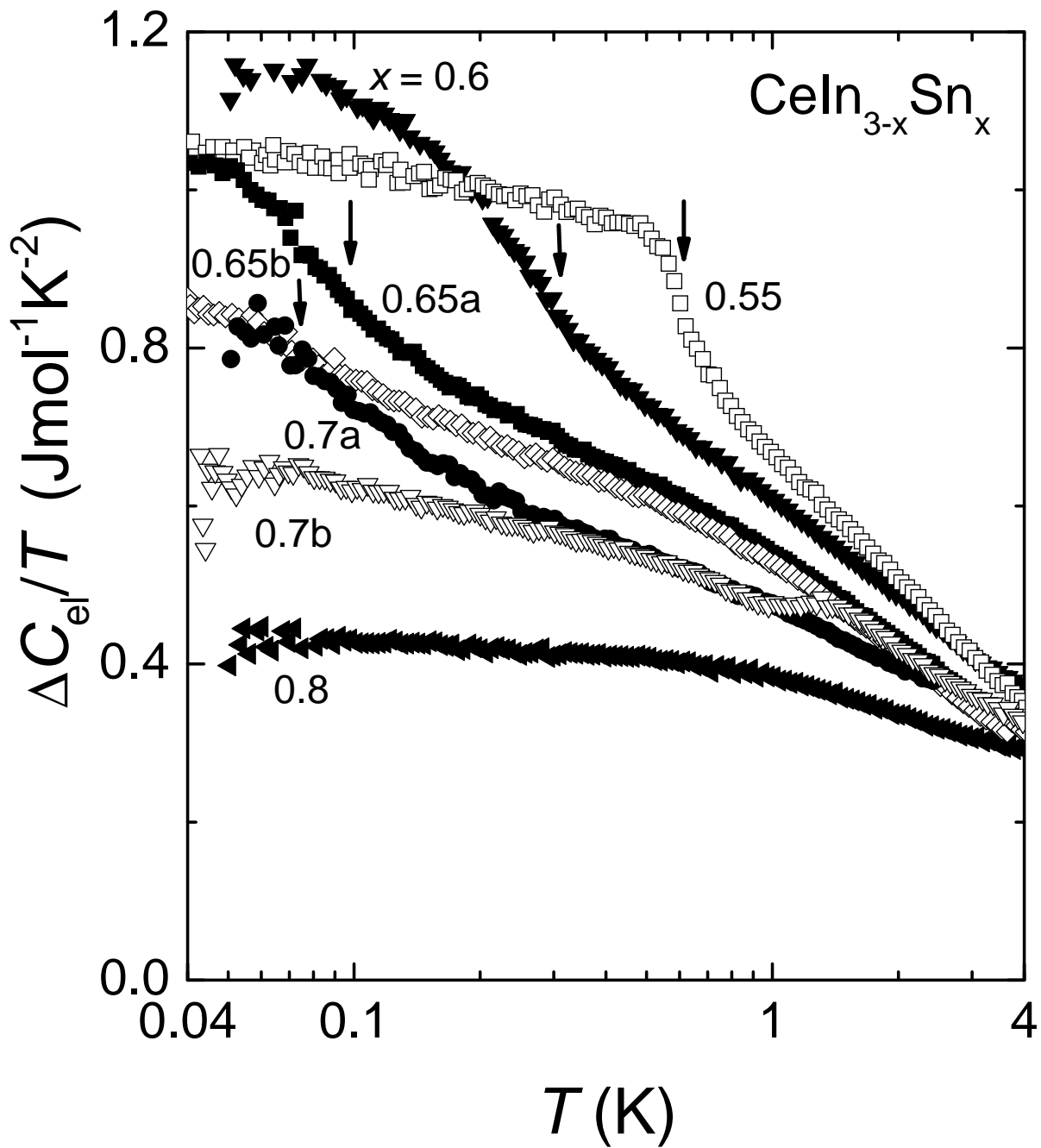
Figure 4.10: *Electronic specific heat $\Delta C/T(T)$ of CeIn$_{3-x}$Sn$_x$ for $0.55 \leq x \leq 0.80$, at $B = 0$, in a log-T plot. The arrows indicate the magnetic ordering temperature.*

0.65a and 0.65b produced using the same growing method. By using the same method to determine T_N as discussed above, T_N is 0.10±0.02 K for 0.65a and 0.07 ± 0.01 K for $x = 0.65b$. The second sample seems to have a slightly larger Sn concentration than the previous one, since T_N is smaller (see Fig. 4.10).

A distribution of the Sn concentration in the alloy can not be excluded. Following the discrepancies observed in the previous samples, for the critical concentration $x = 0.7$ we also measured two samples (0.7a and 0.7b) cut from the same single crystal. No evidence of magnetic order is found for both samples down to $T \simeq 40$ mK. Interestingly, below $T \leq 0.3$ K the sample 0.7a shows a $\Delta C/T \propto -\log T$ behavior while the data for the crystal 0.7b start to flatten. A bump is observed at 1.3 K for the sample 0.7b for reasons which are not understood. It might be due to the contribution of a small amount of impurities, below the resolution of our X–ray diffraction measurements. At even higher concentration, $x = 0.8$, $\Delta C/T$ is almost constant at low temperature ($T \leq 0.7$ K): a signature of the establishment of a LFL phase.

From these measurements we conclude that the AFM ordering is suppressed at $x_c \simeq 0.7$, in accordance with Ref. [107].

For samples with $x < x_c$, the AFM transition can also be suppressed by applying an external magnetic field. The main advantage of field tuning in the case of $CeIn_{3-x}Sn_x$ is that once the system is tuned by doping close to the QCP, the fine tuning can be made in very small steps without introducing additional disorder. In the following section, specific–heat measurements in various magnetic fields are presented.

4.3.3 $CeIn_{3-x}Sn_x$ in applied magnetic field

In these measurements, magnetic fields were applied parallel to one of the cubic crystallographic axes. The sample orientation was carefully checked by Laue X-ray diffraction. $\Delta C/T$ for all the data shown in this section is determined by subtracting from the total specific heat, C, the field–independent quadrupolar contribution, $C_Q = \alpha_Q/T^2$, and taking also into account the Zeeman contribution, $C_{hf} = \alpha(B)/T^2$, with $\alpha(B)$ deduced graphically (see Appendix of this section). Using the relation $\alpha(B) = \alpha_{dip}B^2$, with α_{dip}

the strength of the nuclear magnetic dipolar interaction for In, the linear extrapolation of the high–field data to $B = 0$ in the plot $\alpha(B)$ vs B^2 should yield also α_Q. Thus, we can determine independently α_Q for the investigated samples. The values obtained with these two different methods will be also discussed here.

In Fig. 4.11, $\Delta C(T)/T$ of the $x = 0.55$ sample, is depicted for various magnetic fields. For this concentration, T_N has the highest value among the here studied samples (~ 0.6 K), and, therefore, one can expect the highest stability of the antiferromagnetic fluctuations to field suppression.

As can be seen from the specific heat, CeIn$_{2.45}$Sn$_{0.55}$ is magnetically ordered in the range 0 T$< B < 4$ T. Further increasing the field recovers the LFL behavior, i.e., $\Delta C/T$ in $B \geq 4$ T remains essentially temperature independent at low temperature. In the inset, CT^2 vs T^3 is depicted for $B = 0$ and 4 T below $T \leq 0.15$ K in order to exemplify how we determined the nuclear contribution of In to the specific heat. At higher fields, $B \geq 8$ T the onset of this contribution is shifted to higher temperatures $T \geq 0.2$ K. The graphically determined $\alpha(B)$ values reveal the expected behavior $\alpha(B) \propto B^2$ as shown in the second inset of Fig. 4.11. The $B = 0$ intercept in this plot yields $\alpha_Q \simeq 108.5\,\mu$JKmol^{-1}, somewhat larger than the value obtained by fitting linearly the $B = 0$ data in a CT^2 vs T^3 plot, $\alpha_Q \simeq 81.1\ \mu$JKmol^{-1}.

Fig. 4.12 shows $\Delta C/T$ vs T for $x = 0.6$ in various magnetic fields.

By using the same criterion for determination of T_N as discussed before, T_N is 0.1 ± 0.02 K for $B = 2$ T (not shown). Thus, for a sample with a higher Sn content the AF transition temperature is reduced. Moreover, CeIn$_{2.4}$Sn$_{0.6}$ remains magnetically ordered at fields up to only about 3 T, in comparison with CeIn$_{2.45}$Sn$_{0.55}$. As the magnetic field is raised, antiferromagnetic order is suppressed and the low–temperature $\Delta C/T$ data show a distinct LFL behavior, i.e., $\Delta C/T$ for $B = 6$ T and $B = 8$ T remains temperature independent below ~ 0.15 K and ~ 0.35 K, respectively. Following the same procedure for the determination of α_Q, we obtained similar values from both methods, $\alpha_Q = 160.3(3)\mu$JKmol^{-1} from zero–field data, and $\alpha_Q = 167.14(19)\mu$JKmol^{-1} from high–field data, respectively.
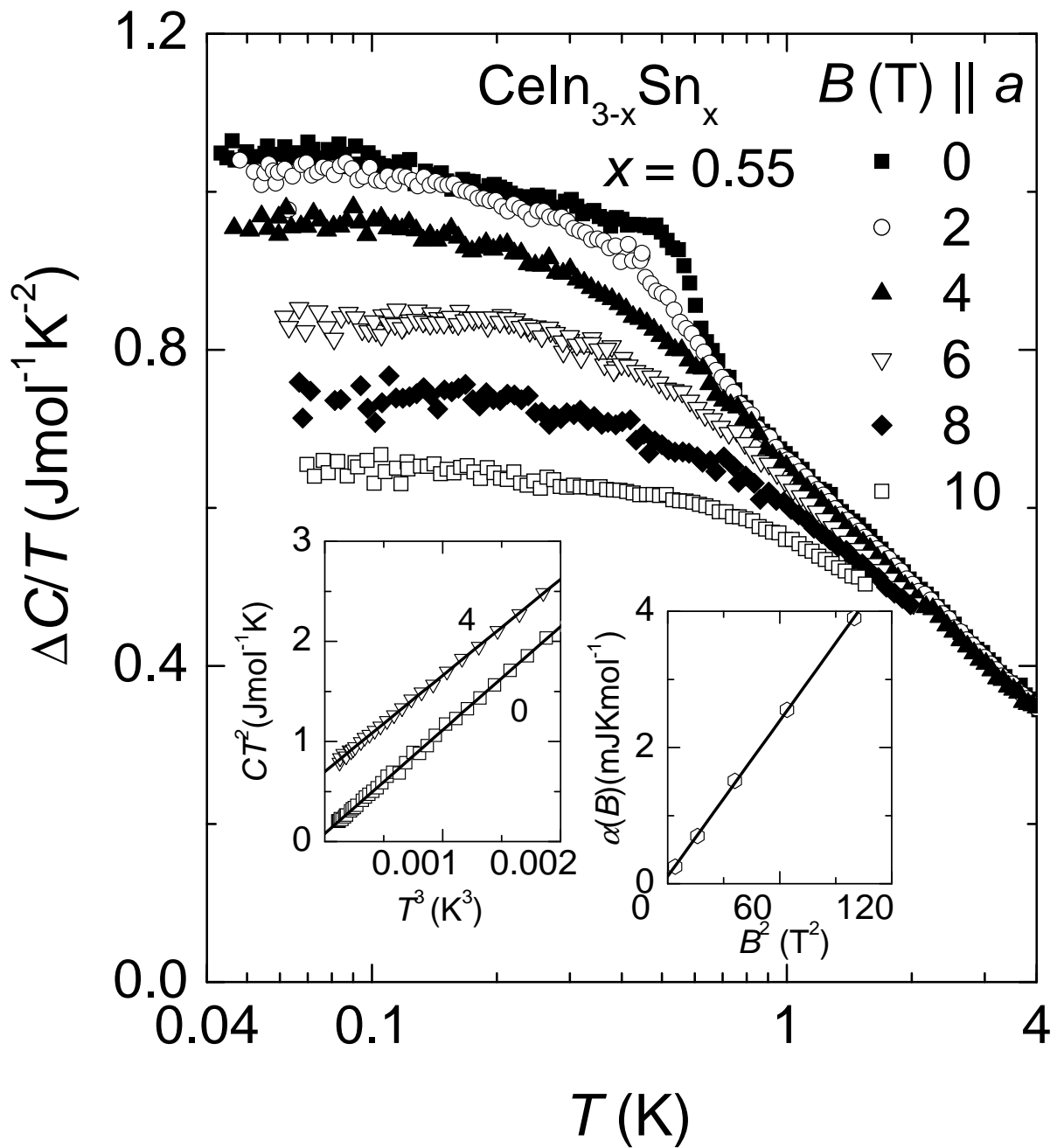
Figure 4.11: *Temperature dependence of the electronic specific heat of $CeIn_{3-x}Sn_x$ divided by temperature, $\Delta C/T$, in various magnetic fields applied parallel to the crystallographic a axis for $x = 0.55$. Inset: CT^2 vs T^3 to determine γ and α (see text) and the $\alpha(B)$ vs B^2 dependence showing the expected linear behavior.*
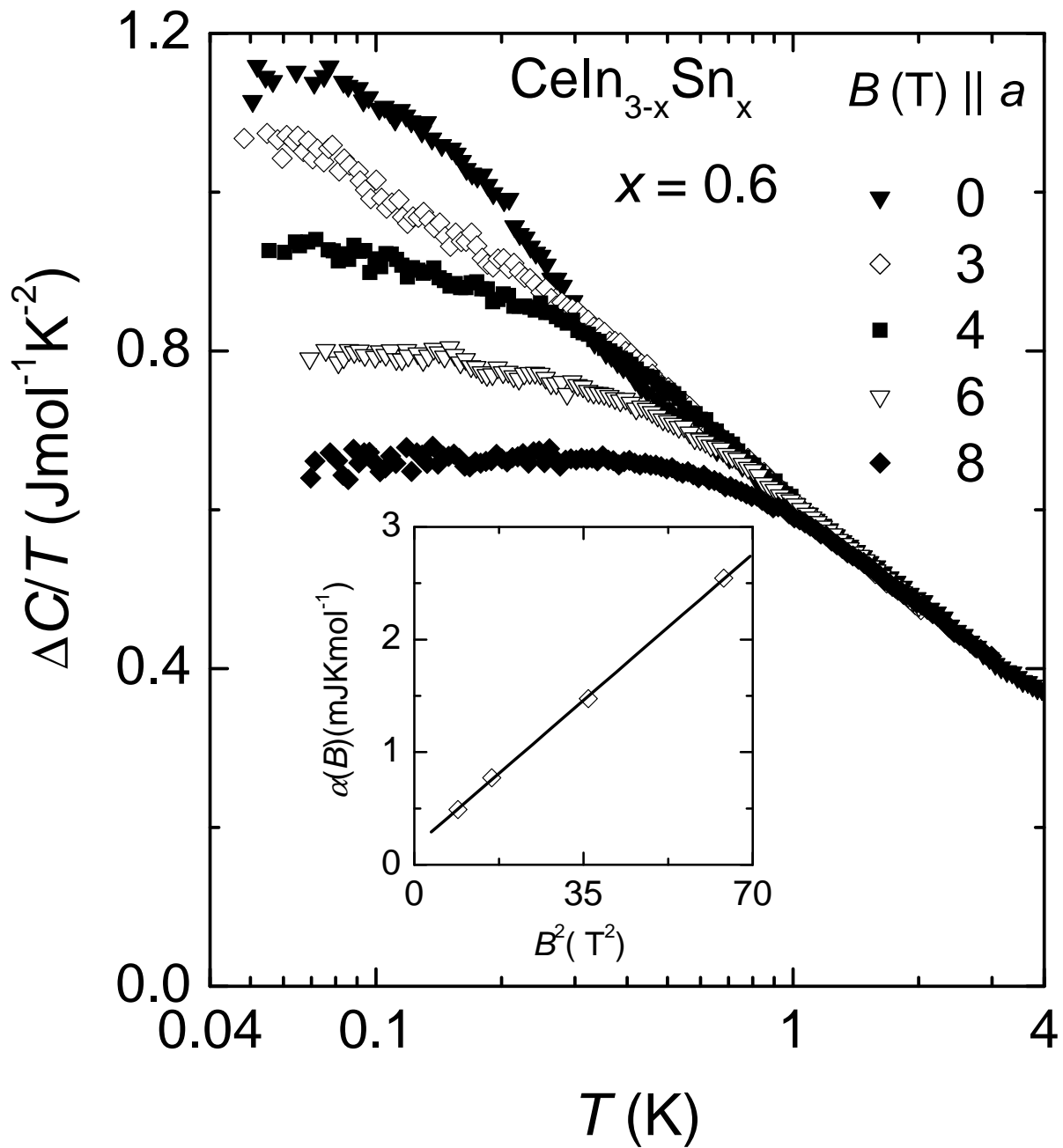
Figure 4.12: *The evolution of $\Delta C/T$ vs T in $CeIn_{3-x}Sn_x$ for $x = 0.60$ with magnetic field, B applied along the crystallographic a axis. Inset: $\alpha(B)$ vs B^2.*
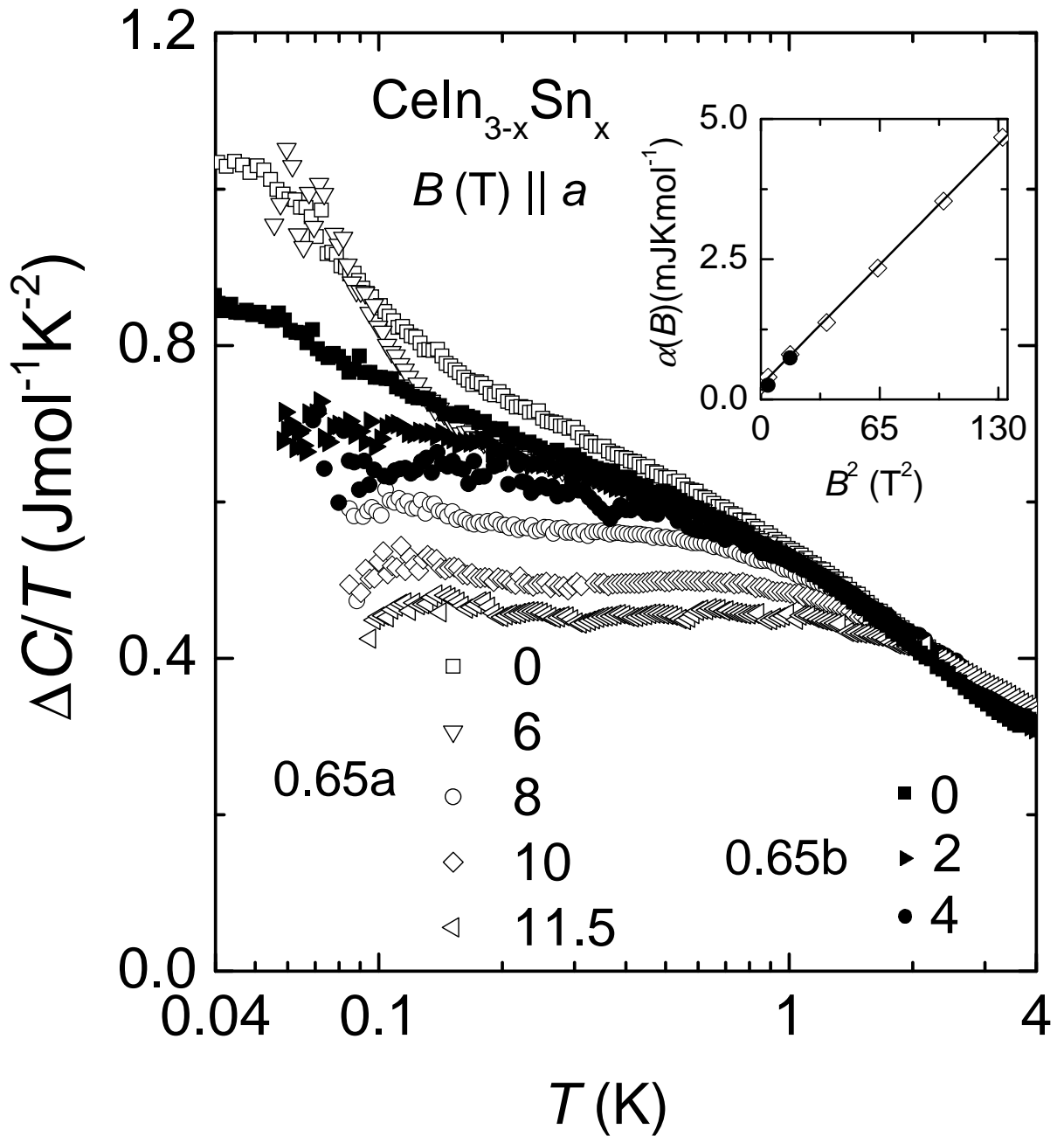
Figure 4.13: $\Delta C/T$ *vs T in $CeIn_{3-x}Sn_x$ for $x = 0.65$ in various magnetic fields applied parallel to the crystallographic a axis. Open and solid symbols show the 0.65a and 0.65b data, respectively. Inset: the evolution of $\alpha(B)$ determined graphically from a CT^2 vs T^3 plot in various applied magnetic fields.*
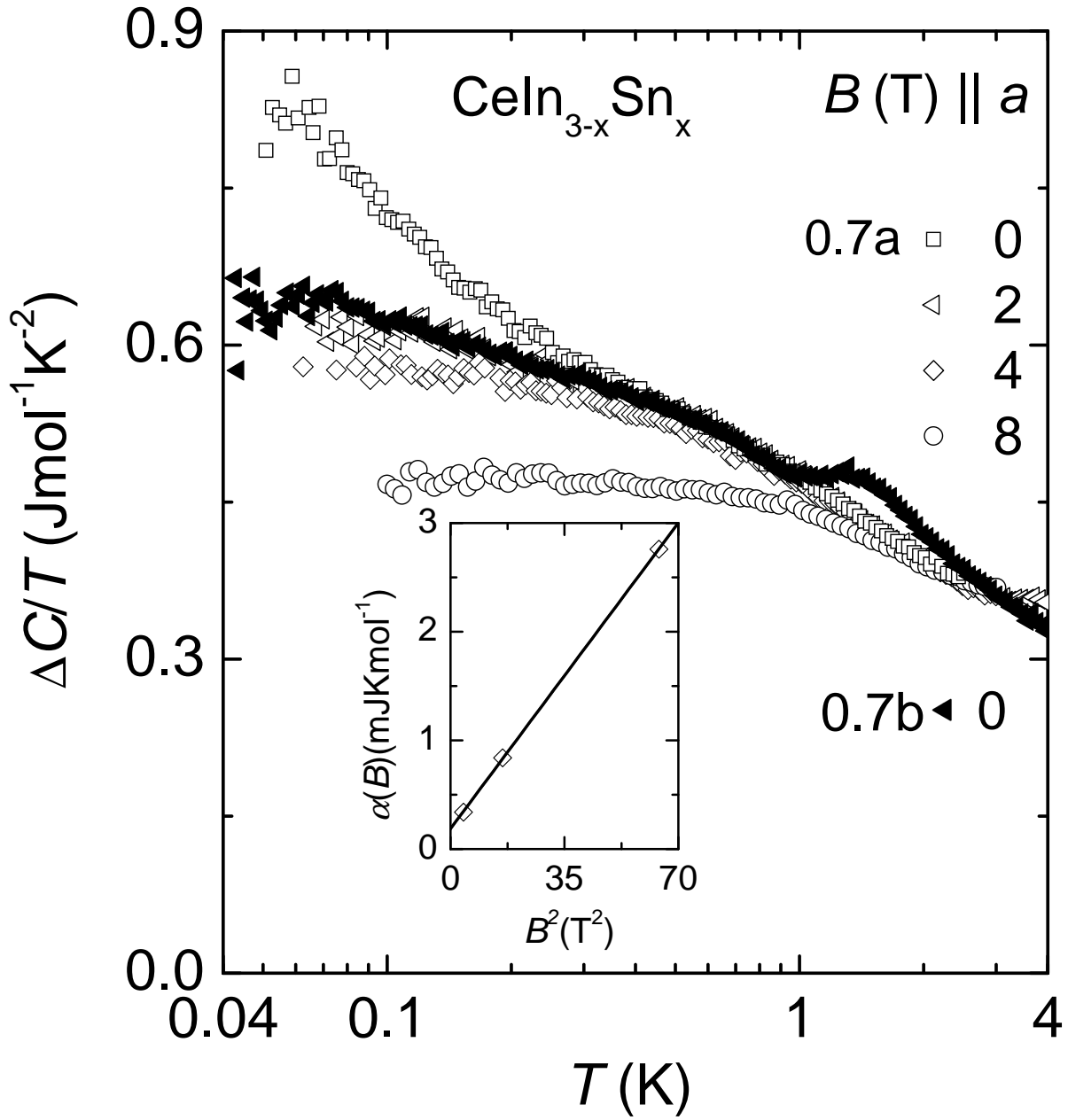
Figure 4.14: $\Delta C/T$ *vs* T *in* $CeIn_{3-x}Sn_x$ *for* $x = 0.7$*, in various magnetic fields applied parallel to the crystalographic a-axis. Open and solid symbols show the 0.7a and 0.7b data, respectively. Inset: the evolution of* $\alpha(B)$ *determined graphically from* CT^2 *vs* T^3 *plot in various applied magnetic fields.*

$CeIn_{2.35}Sn_{0.65}$ is situated in the vicinity of the AFM QCP. This is indicated by the relatively low AFM transition temperature for sample 0.65a, $T_N = 0.1 \pm 0.02$ K (open symbols in Fig. 4.9) compared with the previous sample. Surprisingly, as shown in Fig. 4.13, for this particular sample, higher magnetic fields, $B \geq 8$ T, compared to the $x = 0.55$ and $x = 0.6$ samples, are needed to recover the LFL behavior. For $B \leq 6$ T, $\Delta C(T)/T$ still shows a strong increase at low temperatures probably related to some remanent magnetic order which increases abruptly at low temperatures, $T \leq 0.2$ K. This gives an important contribution to the low–temperature part of the specific heat which overlaps with the nuclear contribution. In the inset of Fig. 4.13, $\alpha(B)$ vs B^2 for samples 0.65a and 0.65b is shown by open and solid symbols, respectively. In the case of crystal 0.65a, the extrapolation from high fields to $B = 0$ yields $\alpha_Q \simeq 234.1\mu$ JKmol^{-1} which is much larger than the value $\alpha_Q \simeq 77\mu$ JKmol^{-1} obtained by fitting the zero field data in a CT^2 vs T^3 plot. An important observation is that the discrepancy between the two values is reduced if we make the extrapolation using only the $\alpha(B)$ values obtained in the field region $B > 6$ T, where the magnetism is suppressed and does not contribute anymore to the low–temperature specific–heat data. In this case $\alpha_Q \simeq 142.5$ μJKmol^{-1}.

We checked the behavior of $C(T)$ in magnetic field for the second sample, 0.65b, which was assumed to have the same composition as the previous one, 0.65a. However, our zero–field measurements (see Fig. 4.9) have already shown that this sample has a slightly higher Sn content than 0.65a. This is inferred from the observation of a lower ordering temperature, $T_N = 0.07 \pm 0.03$ K, which in sample 0.65b can be easily suppressed by the application of a smaller magnetic field (see Fig. 4.13–closed symbols). For $B = 2$ and 4 T, $\Delta C/T(T)$ clearly shows LFL behavior, i.e., $\Delta C/T$ is temperature independent below 0.2 and 0.3 K, respectively. The corresponding $\alpha(B)$ values are shown in Table 4.4 in the appendix.

Fig. 4.14 gives the data for both samples, 0.7a and 0.7b, indicated by open and solid symbols, respectively. The logarithmic temperature dependence of $\Delta C(T)/T$ observed in zero field for 0.7a is suppressed in 2 T. For this value of the magnetic field, our data show saturation below ~ 0.15 K. With further increasing of B, $B = 4$ T, the LFL state

forms for temperatures below 0.3 K. The LFL region extends to higher temperatures upon increasing field. For $B = 2$ T, the $\Delta C(T)/T$ data are similar to those of the 0.7b sample in zero field (solid symbols) in the temperature region 0.1 K $\leq T \leq 1$ K. Taking into account the scattering of the data below 0.1 K, we can state that the 0.7a data in $B = 2$ T overlap with the 0.7b data measured in zero field for temperatures below 1 K. However, there are no magnetic–field measurements for the 0.7b sample to complete the comparison of the specific heat in magnetic field.

   With further increasing the Sn content, the CeIn$_{2.2}$Sn$_{0.80}$ sample shows no evidence of an AFM transition down to $T = 0.05$ K (see Fig. 4.15). Instead, $\Delta C(T)/T$ is almost constant below 0.15 K indicating LFL behavior. By applying field the LFL state extends towards higher temperatures. For this sample $\alpha_Q = 130.1(3)$ μJKmol^{-1} obtained from zero field data is in good agreement with the value obtained from the measurements in applied magnetic field, $\alpha_Q = 125.16(14)$ μJKmol^{-1}.

4.3.4 Discussion

The results of the specific–heat measurements on CeIn$_{3-x}$Sn$_x$ presented in the previous section show that this system has unique properties. The suppression of the AFM transition can be observed over a remarkable large temperature range, from $T_N = 10.2(1)$ K down to $T_{\mathrm{N}} \simeq 0.07$ K (see Fig. 4.9). T_N becomes zero at a critical concentration of $x \approx 0.7$. Both samples 0.7a and 0.7b, measured for this concentration are located close to the QCP. The sample 0.7b is probably at the nonmagnetic side as suggested by the comparison with the 0.7a data in applied magnetic field (see Fig. 4.14).

   In the vicinity of the QCP, quantum fluctuations become dominant and anomalous behavior is observed; $\Delta C(T)/T$ for 0.7a shows a logarithmic increase below $T \leq 0.3$ K (see Fig. 4.10). In an earlier paper [110], the measurements were performed only for $x = 0.55$, 0.6, 0.65a, 0.7b and 0.8, and the results were explained in terms of 3D SDW theory. However, our understanding of the system was improved by measuring 0.65b and 0.7a, and it became clear that the existing 3D SDW theory does not explain the
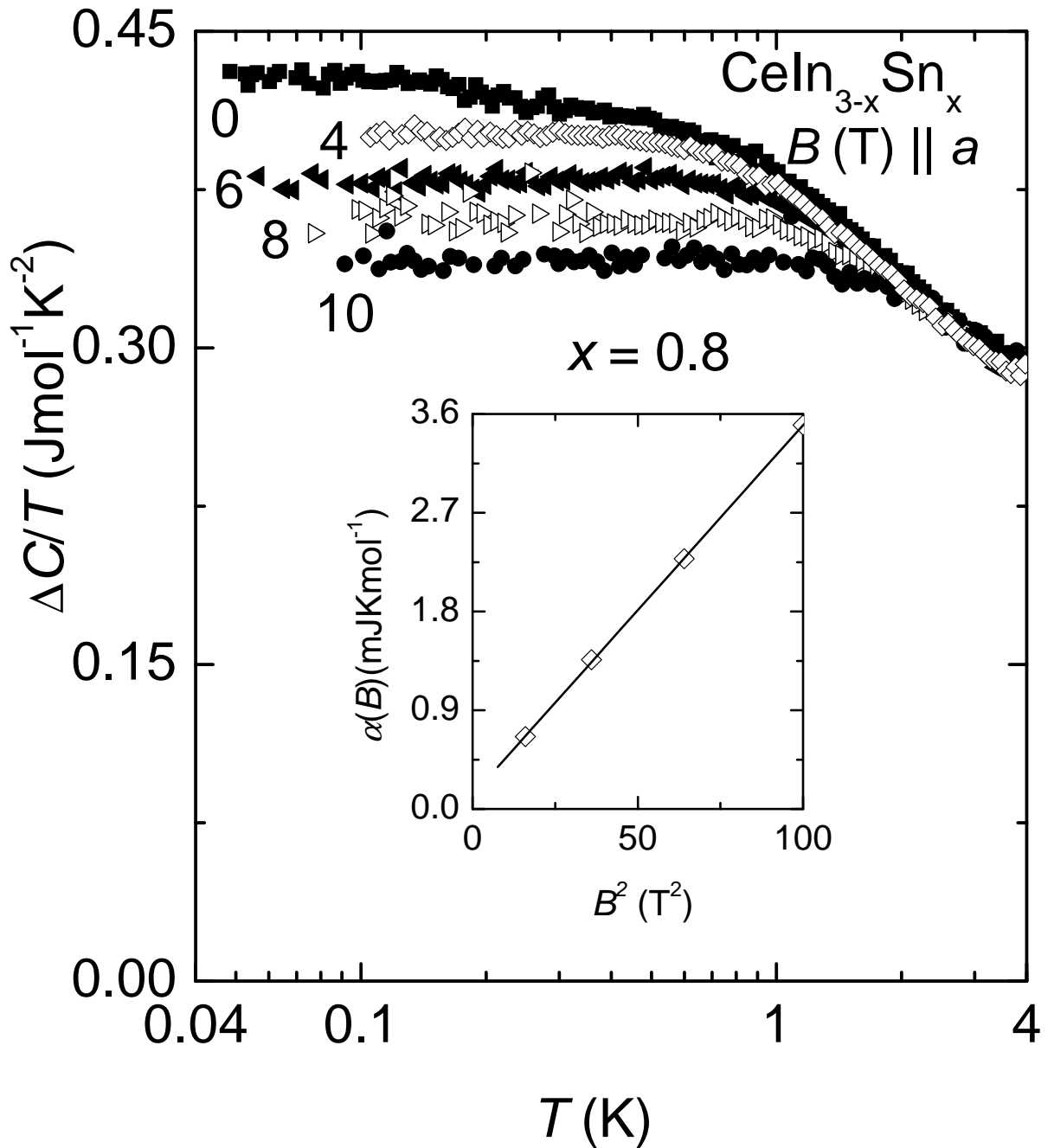
Figure 4.15: $\Delta C/T$ *vs* T *in various magnetic fields applied parallel to the crystallo-graphic a axis for* $x = 0.80$*. Inset shows the behavior of* $\alpha(B)$ *as a function of* B^2 *(see text).*

observed $C(T)$ behavior in the vicinity of the QCP. Moreover, resistivity measurements on polycrystalline CeIn$_{3-x}$Sn$_x$ demonstrate that T_{N} vanishes at the same critical Sn content of $x_{\mathrm{c}} \simeq 0.7$ [107]. For this concentration a linear decrease of the resistivity with decreasing temperature was observed over much more than one decade in temperature, $0.02 \text{ K} \leq T \leq 0.8 \text{ K}$. The observed NFL effects, in the present specific–heat data and earlier reported resitivity measurements [107] are surprising, because these features resemble the proposed behavior for the 2D SDW scenario [30, 68, 80]. The results are striking mainly when we compare them with those obtained from thermal–expansion measurements [71] which were carried out on single crystals from the same generation. The critical Grüneisen ratio, $\Gamma^{cr}(T)$ is shown to diverge $\Gamma^{cr} \sim T^{-a}$ with $a = 1.06(8)$ for a $x = 0.65$ single crystal. This agrees well with the prediction for the 3D–SDW scenario [109]. In spite of this, for $x = 0.65$, our specific heat shows magnetic order in both single–crystalline samples (0.65a and 0.65b) with $T_N \simeq 0.1 \text{ K}$ and $T_N \sim 0.07 \text{ K}$, respectively (Fig. 4.10).

Concerning the nuclear contribution to the specific heat, it is worth noting that the effect of doping on CeIn$_3$ with Sn is nontrivial; this can be seen in Fig. 4.16(a) where the α_Q values are summarized for the samples studied here in a plot α_Q vs Sn content. Solid symbols represent the α_Q values obtained by fitting linearly CT^2 vs T^3 in $B = 0$, while open symbols represent the values obtained by extrapolating $\alpha(B)$ linearly to $B = 0$ in a plot $\alpha(B)$ vs B^2, from data in the field region were the magnetic order is suppressed. The slope, α_{dip}, as a function of Sn content is shown in Fig. 4.16(b) by the open symbols. The solid line in this figure represents the evolution of α_{dip} with increasing Sn content, calculated by using eq. (2.21) in Sec. 2.2, with NMR frequencies taken from Ref [82]. For the 0.55 sample ($T_N \simeq 0.6 \text{ K}$) there is a small discrepancy between the two obtained values of about $\sim 27 \, \mu\text{JKmol}^{-1}$. This difference corresponds to the change of the slope in $\alpha(B)$ vs B^2 above $B = 4 \text{ T}$ when the antiferromagnetic order in this sample is suppressed. With further increasing Sn content, the AFM transition temperature is reduced, and a smaller field ($B \simeq 3 \text{ T}$) in the case of the 0.6 sample is needed to suppress the remaining AFM fluctuations and induce the LFL behavior. This is reflected in the small

difference we obtained between the two determined α_Q values as shown in Fig. 4.16(a). An anomalous behavior in magnetic field was observed for sample 0.65a. For this sample the difference between the high–field ($B \geq 6$ T) extrapolated value of α_Q and that obtained by fitting the low–temperature zero–field data is large, ~ 65 μJKmol^{-1}. This corresponds to a decrease in α_{dip}. However, for this particular sample the magnetic field above which the system enters the LFL state has the maximum value among the CeIn$_{3-x}$Sn$_x$ samples studied here. Therefore, it seems reasonable to suppose that, for this particular sample, (0.65a), there is an important additional contribution to the low–temperature specific heat due to some remanent low–temperature AFM correlations, which persist up to 6 T. For the 0.65b sample no anomaly was observed in applied field. The LFL state is observed at low temperatures, $T \leq 0.15$ K for $B = 2$ T. There are no measurements for $B > 4$ T but based on what we observed for the previous samples, one expects no change in the slope (α_{dip}) of the $\alpha(B)$ vs B^2 plot. The most interesting effect is observed for the sample with the critical concentration, $x \simeq 0.7$a. For this sample no AFM transition was observed down to the lowest accessible temperature, $T \simeq 0.04$ K (see Fig. 4.10). In spite of this, there is a considerable large difference ~ 75 μJKmol^{-1} between the two α_Q values which might be related to the proximity of the 0.7a sample to the QCP. Our measurements proved that 0.7a$<$ 0.7b $<$ 0.8 and thus, 0.7b sample is situated at the QCP on the nonmagnetic side. No magnetic–field measurements were done for this particular concentration.

With further increasing the Sn content, for the $x = 0.8$ sample no discrepancy was obtained in the α_Q values. It is worth noting that the linear fit of the experimentally obtained α_{dip} values when we do not consider the critical concentration 0.7a, has the same slope as that obtained using eq. (2.21) in Sec. 2.2 (Fig. 4.16(b)). This indicates that indeed the α_Q and α_{dip} values obtained from our specific–heat data are reliable and the anomaly observed in both, the $x = 0.65$ and $x = 0.7$ samples could be related to the proximity of the QCP. Nevertheless, taking into account the nontrivial effects of the substitution of In by Sn on the α_Q (which depends on the amount of In and the configuration of the ionic charge around the In atoms) and also the reproducibility of
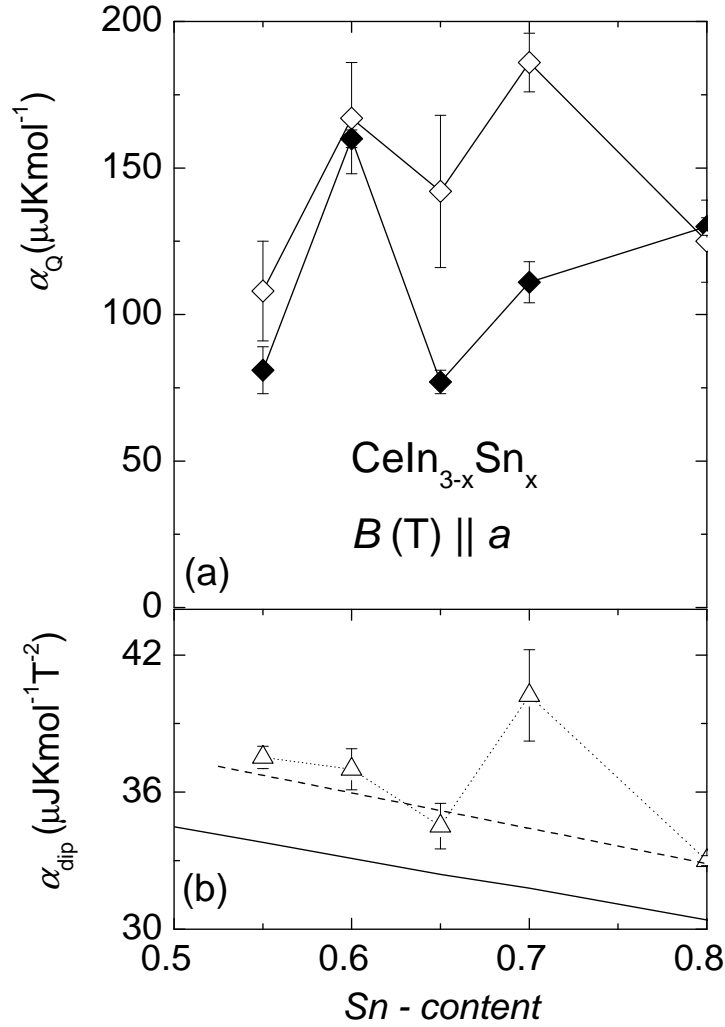
Figure 4.16: *(a) α_Q vs Sn content for $CeIn_{3-x}Sn_x$. Solid symbols represent the values obtained by fitting linearly CT^2 vs T^3 in $B=0$ and open symbols represent the values obtained by extrapolating the high–field data to zero in a plot $\alpha(B)$ vs B^2 (see text). (b)α_{dip} as a function of Sn content obtained from $\alpha(B)$ vs B^2 plot (open symbols) and the linear fit through these data (dashed line) when we do not consider the critical concentration 0.7a. Solid line represents α_{dip} vs Sn content, theoretically calculated (see text).*

the samples one has to be very careful with this speculation. However, this gives a clear motivation for further measurements of the compounds in the series in order to clarify this issue.

The antiferromagnetism in the samples with $x < x_{\mathrm{c}}$ can also be suppressed by applying a sufficiently large magnetic field, instead of increasing the doping level, leading to the recovery of the LFL state, i.e., $\Delta C(T, B)/T \simeq \gamma(B)$ which extends towards higher temperatures with rising field. Fig. 4.17(a) shows $\gamma_{0.04\ K} = C(T)/T|_{T=0.04\ K}$ vs B for $0.55 \leq x \leq 0.8$. For the samples with $x =$0.55, 0.6, and 0.65a our data have shown that there is a plateau in $\gamma_{0.04}(B)$ for $B \leq 2$ T, $B \leq 3$ T, and $B \leq 6$ T, respectively, followed by a decrease of the Sommerfeld coefficient at higher fields. The field where $\gamma(B)$ starts to strongly decrease is denoted by B^* (see Fig. 4.17(a)). For sample $x =$0.65a, B^* reaches the maximun value, $B^* = 6$ T. The existence of this plateau is probably related with the AFM spin fluctuations, since this feature is clearly observed particularly in concentrations where the AFM transition occurs at $T_{\mathrm{N}} \simeq$ 0.6 K, 0.3 K, and 0.1 K, respectively, but not for the $x =$0.65b sample which is situated very close to the QCP ($T_N \simeq 0.07$ K). In this context, very significant is Fig. 4.17(c) which shows the evolution of T_{N} (solid symbols) and B^* (open symbols) with Sn concentration. On the contrary, $\gamma(B)$ for 0.65b sample does not show a plateau. Upon applying magnetic field, the LFL state is observed at low temperatures, and $\gamma(B)$ starts to decrease by applying a small field, $B = 2$ T, similar to $\gamma(B)$ for $B > B^*$ for the samples with less Sn content. This indicates first a weakly field–dependent quasiparticle mass upon tuning the QCP by field, and, secondly, the magnetic correlations initially are very robust against field, but upon increasing the applied magnetic field, when the system approaches the QCP, $(T_{\mathrm{N}} \rightarrow 0)$, these low–lying excitations are immediately destroyed and the system is tuned from an AFM ground state directly in a LFL state, similar to the case of the earlier reported material $CeNi_2Ge_2$ [111].

For $x = 0.8$, γ remains almost constant when the field is applied as expected since this system was found to be placed in the LFL state in zero field. Thus, we can conclude that by applying an external magnetic field on the samples of the $CeIn_{3-x}Sn_x$ system
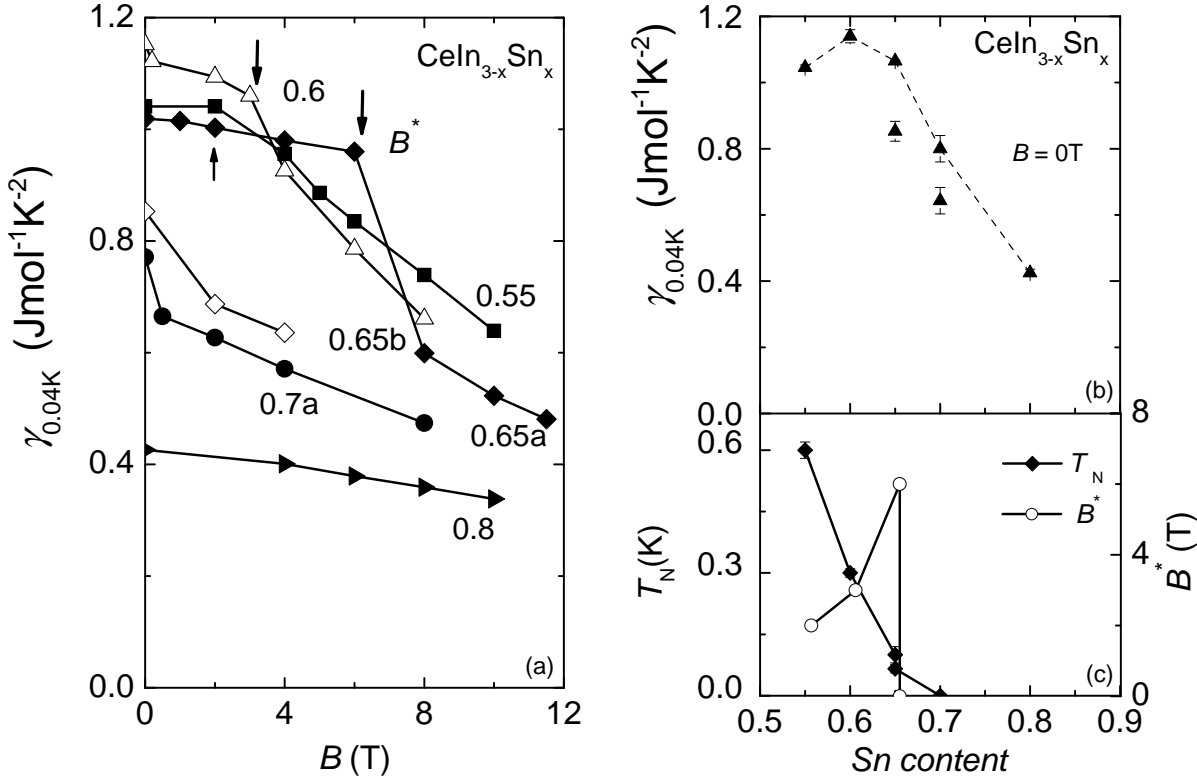
Figure 4.17: *(a) The evolution of the Sommerfeld coefficient of the specific heat at T = 0.04 K for all CeIn$_{3-x}$Sn$_x$ samples investigated here: (a) with applied magnetic field and (b) in zero field. (c) Open symbols show the concentration dependence of the field B* where γ(B) starts to decrease strongly (see text). Solid symbols indicate the concentration dependence of T$_N$.*

which show AFM ordering, no divergence of $\gamma = C(T)$ is detected by field tuning for any concentration.

Fig. 4.17(b) shows the evolution of the Sommerfeld coefficient of the specific heat, $\gamma_{0.04\ K}$ with Sn–content, for $0.55 \leq x \leq 0.8$. For $x = 0.6$, the Sommerfeld coefficient has the maximum value, $\gamma \simeq 1.14(2)$ Jmol^{-1}K^{-2}. This can be due to some low–lying spin fluctuations as this sample shows order at $T_N \sim 0.3$ K. However, similar $\gamma(x)$ behavior was earlier reported in Ref. [99] for a number of compounds [101] around their QCP. With further increase in x, for $x > 0.6$, γ decreases rapidly with increasing x. Thus, in the vicinity of the critical concentration, our results show no divergence of γ with

x (Fig. 4.17). However, such a scenario was also excluded from the analysis of the thermal–expansion data [71]. Thus, in contrast to the Yb–based compounds presented in the previous section, in the vicinity of the QCP, $CeIn_{3-x}Sn_x$ shows no evidence of a divergence in γ, neither with B nor with x.

4.4 Appendix: nuclear contributions to $C(T)$

The nuclear contributions were determined from a plot of $C_{tot}T^2$ vs T^3, assuming that the total specific heat C_{tot} is given by the sum of nuclear and electronic contributions, $C_{tot} = C_{nuc} + C_{el}$. The nuclear contributions are due to the hyperfine interactions and can be written as $C_{nuc} = \alpha/T^2 = (\alpha_Q + \alpha(B))/T^2$, with α_Q and $\alpha(B)$ the quadrupolar and the Zeeman contribution, respectively. In this way we obtained α_Q and $\alpha(B)$ for each of the investigated compounds which are summarized in the tables below:

B_{ext} (T)	$\alpha(B)$ (μJKmol^{-1})	B_{hf} (T)	M_{cal} μ_B/Yb	M_{mea} μ_B/Yb
0.2	24	15	0.129	0.114
1	95	34	0.268	0.257
6	676	93	0.733	0.719
8	954	111	0.865	0.848
10	1133	121	0.932	0.937
11.5	1290	129	0.988	0.982

Table 4.2: $\alpha(B)$ *values for various applied magnetic fields, B_{ext}, the corresponding hyperfine field, B_{hf}, the calculated and measured field dependence of the magnetization, M_{cal} and M_{mea}, respectively for $YbRh_2(Si_{0.95}Ge_{0.05})_2$ (see text).*

B_{ext} (T)	$\alpha(B)(5\%La)$ (μ JKmol^{-1})	$\alpha(B)(10\%La)$ (μ JKmol^{-1})	$\alpha(B)(Ir)$ (μ JKmol^{-1})
0.02	-	33	-
0.1	-	45	-
0.3	80	-	-
0.5	82	64	-
1	92	-	128
2	108	-	-
4	248	-	161
6	-	-	211
8	-	-	266

Table 4.3: $\alpha(B)$ values for various applied magnetic fields, B_{ext}, for Yb$_{0.95}$La$_{0.05}$Rh$_2$Si$_2$, Yb$_{0.9}$La$_{0.1}$Rh$_2$Si$_2$, and YbIr$_2$Si$_2$, respectively.

	$\alpha(B)$ (μ JKmol^{-1})					
$B(T)$	$x = 0.55$	0.6	0.65a	0.65b	0.7b	0.8
2	250	-	190	214	360	-
3	-	480	-	-	840	-
4	701	773	546	610	-	660
6	1511	1475	1160	-	2623	1360
8	2552	2545	2260	-	-	2280
10	3899	-	3500	-	-	3520
11.5	-	-	4640	-	-	-

Table 4.4: $\alpha(B)$ values for CeIn$_{3-x}$Sn$_x$, $0.55 \leq x \leq 0.8$.

# 5 Low dimensional quantum magnets

5.1 Introduction

Low–dimensional magnets have attracted considerable interest owing to the quantum–mechanical nature of their ground state. Because of the increased importance of quantum fluctuations, i.e., the tendency of spins to flip spontaneously, these systems exhibit many distinctive collective properties at low temperatures, which have no counterpart in higher dimensions. In search for correlated quantum states in low–dimensional magnets we explore the magnetic order and spin excitations in low–dimensional quantum AFMs Cs_2CuCl_4, and Cs_2CoCl_4 using specific–heat measurements at low temperatures (0.03 K $< T < 6$ K) and high fields $B < 12$ T.

The compounds we have investigated here, have the β-K_2SO_4–type crystal structure (Pnma, D_{2h}^{16}) [112] shown in Fig. 5.1(a) and very similar lattice parameters (see Table 5.1).

compound	a (Å)	b (Å)	c (Å)	J (K)	J'/J	T_N (K)
Cs_2CuCl_4	9.65	7.48	12.35	4.34(6)	0.342	0.62(1)
Cs_2CoCl_4	9.71	7.27	12.73	2.6	0.014	0.22(1)

Table 5.1: *The lattice parameters at 0.3 K, the exchange constants, and the ordering temperatures of Cs_2CuCl_4 and Cs_2CoCl_4 [112, 113, 114, 115].*
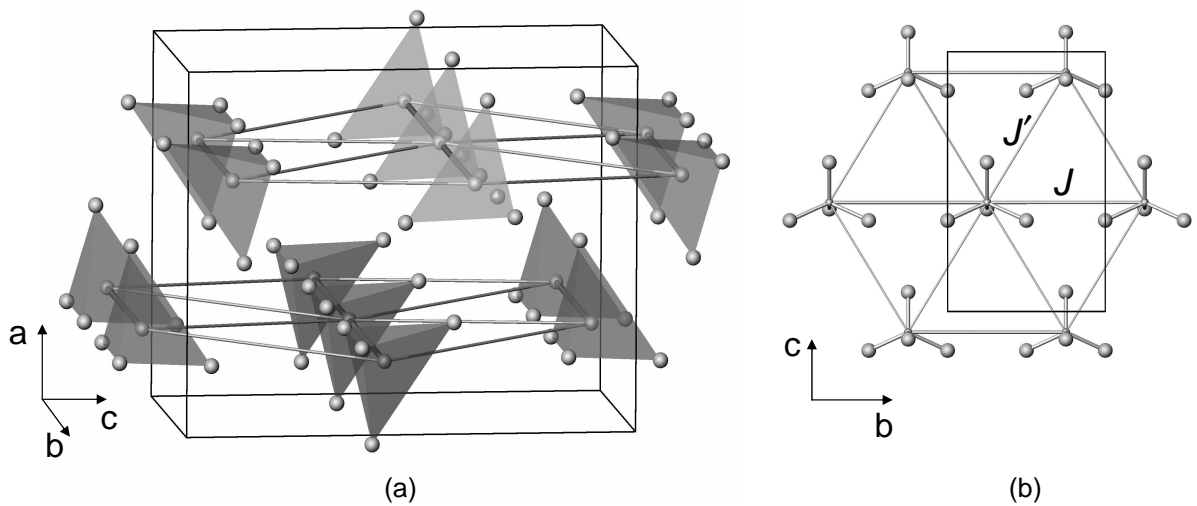
Figure 5.1: (a) *Crystal structure of Cs_2CuCl_4 showing the $CuCl_4$ tetrahedra arranged in layers (bc plane). The orthorombic unit cell is indicated by the rectangular box.* **(b)** *Magnetic exchange paths in the (bc) layer which form a two-dimensional anisotropic triangular lattice with $J'/J = 0.34(3)$.*

The chemical unit cell contains four Cu^{2+} or Co^{2+} ions, respectively, surrounded by the tetrahedrons of the chlorine atoms. The magnetic ions are Cu^{2+} for Cs_2CuCl_4 and Co^{2+} for Cs_2CoCl_4 carrying a spin 1/2, and they form a triangular arrangement with non-equivalent exchange couplings J and J' indicated in Fig. 5.1(b). The ratio J'/J controls the properties of the systems. If $J'/J = 0$ the system can be regarded as an assembly of four decoupled spin chains passing through the unit cell, along the b axis. In Cs_2CoCl_4, the important interactions are the intrachain exchange $J = 0.23$ meV, between the two nearest-neighbor (NN) ions along the b axis, and a weak exchange J' between neighboring chains, $J'/J = 0.0147$. Therefore, the system can be regarded as a quasi–one–dimensional (1D) spin–1/2 antiferromagnet with very small interchain couplings. If $J'/J = 1$ and $0 < J'/J < 1$ the system is fully frustrated and partially frustrated, respectively. Cs_2CuCl_4 falls in the class of quasi–two–dimensional (2D) frus-

trated spin system [116] with $J'/J = 0.342$.

Neighboring Cu and Co ions interact via superexchange interaction involving a bridge of two Cl^-–ions with the path $(Cu,Co)^{2+}$–Cl^-–Cl^-–$(Cu,Co)^{2+}$. It is noteworthy that the Co–Co and Cu–Cu distance itself is not important for direct exchange between the cations to be appreciable. The superexchange route mediated by two nonmagnetic Cl^- ions is quite large in both compounds, thus the exchange couplings are expected to be rather weak.

Cs₂CuCl₄ and Cs₂CoCl₄ undergo a magnetic phase transition at $T_N = 0.62(1)$ K and $0.22(1)$ K, respectively. The present study is motivated by the field–induced suppression of the ordered phase. The added benefit of the systems that we explore experimentally is the fact that the energy scale of the interactions is relatively low, so the full phase diagram is experimentally accessible. We explore this in experiments to be able to look at how quantum fluctuations are tuned by field across the whole phase diagram.

5.2 Quasi–2D spin–$1/2$ Heisenberg AFM Cs₂CuCl₄

5.2.1 Magnetic properties of Cs₂CuCl₄

Cs₂CuCl₄ system is a spin–1/2 AF on a frustrated triangular lattice so that the quantum fluctuations are strong and also enhanced by the low dimensionality. There is a strong competition between kinetic energy gained by quantum fluctuations and the potential energy gained by mean–field ordering firstly observed by neutron scattering measurements [117].

Neutron–scattering measurements on Cs₂CuCl₄ showed considerable dispersion in the (bc) plane which indicates a strong 2D character of the system [116]. These observations require a change in the point of view taken by earlier studies [118], which proposed a quasi-1D picture based on estimates of the interchain couplings. This quasi-2D character is a result of the layered crystal structure, which restricts the main superexchange routes to neighboring spin sites in the (bc) plane. Zero–field measurements showed below $T_N = 0.62(1)$ K magnetic ordering in the form of an incommensurate spiral due to the

frustrated couplings, with the ordering wavevector $Q = (0.5 + \epsilon_0)b^*$ and the incommensuration relative to Néel order $\epsilon_0 = 0.030(2)$. The incommensurate ordering wavevector and the excitation energy are strongly renormalized from their classical values, indicating large quantum fluctuations in the ground state [119]. The spin–excitation spectrum measured in neutron–scattering experiments shows extended excitation continua, and several theoretical approaches have been put forward to explain this observation in terms of fractional-spin excitations of a proximate spin-liquid state [116]. In fact, Cs_2CuCl_4 is one of the first quasi-2D spin-1/2 Heisenberg antiferromagnets where dominant excitation continua, characteristic of fractionalization of spin–1 spin waves into pairs of deconfined spin-1/2 spinons were observed [117, 119], instead of sharp spin-wave excitations. Although P. W. Anderson first proposed a 2D fractionalized state in 1973 (the resonating valence bond state (RVB)) [120], the essential conditions for its existence have remained highly contentious.

Neutron–scattering measurements [116] at high fields above the ferromagnetic saturation were used to determine the full spin Hamiltonian. The main exchanges form a two-dimensional triangular lattice with spatially anisotropic couplings as shown in Fig. 5.1(b) with $J = 0.374(5)$ meV for the spin chains along the b-axis and $J'/J = 0.34(3)$ for the zig-zag bonds between the chains in the bc plane. Weak Dzyaloshinskii-Moriya (DM) anisotropy within the layers, along the zig-zag bonds $D_a/J = 0.053(5)$ was found and the interlayer coupling was estimated to $J''/J = 0.045(5)$. The DM interaction breaks the isotropic spin symmetry and creates an easy-plane anisotropy in the bc plane of the spiral order.

The incommensurate spiral order is stable up to saturation (~ 9 T) for fields applied perpendicular to the spiral plane. Moreover, using the field to control the excitations, for this particular direction of the applied magnetic field recent neutron scattering measurements suggested that the field–induced magnetic phase transition can be understood as a Bose condensation of magnons [119]. Surprisingly, the incommensurate spiral order is suppressed by rather small parallel fields (2.1 T $\parallel$ c-axis) compared to saturation field ~ 9 T) [119]. With the aim to learn more about the ground–state properties in

the intermediate-field region and to understand better how the physics evolves from the low-field region, dominated by strong quantum fluctuations, up to the saturated ferromagnetic phase, where quantum fluctuations are entirely suppressed by the large field, we have used specific–heat measurements to probe the complete phase diagrams in both parallel and perpendicular fields.

5.2.2 Results in zero field

Figure 5.2 shows the results of the specific–heat measurements on a solution-growth single crystal of Cs_2CuCl_4 in zero magnetic field in the temperature range 0.03 K $\leq$ $T \leq$ 6 K. The magnetic specific heat, C_{mag}, was obtained by subtracting from the total specific heat, C_{tot}, the contribution of the lattice and the nuclear specific heat. To estimate the lattice contribution, C_{ph}, additional high–temperature measurements (0.3 K $\leq T \leq$ 300 K) were performed in a commercial PPMS (Quantum Design) calorimeter using the relaxation method. Thus, using a Debye temperature $\Theta_D = 126$ K estimated from the high-temperature $T \geq 10$ K data, $C_{ph} = 13600 \, (T/\Theta)^3$ Jmol^{-1}K^{-1}. The nuclear quadrupolar contribution to the specific heat, $C_Q = \alpha_Q/T^2$ at very low temperatures, $T \leq 0.1$ K was determined from a plot of CT^2 vs T^3. In this way we obtained $\alpha_Q = 33(11) \times 10^{-6}$ JKmol^{-1}. The contributions of the phonon and nuclear specific heat to C_{tot} have been accounted for in the analysis of all the raw data shown in this chapter.

The most prominent features of the magnetic specific heat at $B = 0$, presented in Fig. 5.2 are a sharp λ–like anomaly at $T_N = 0.62$ K which indicates the transition to 3D long–range order, where the magnetic structure found by neutron diffraction is a spiral in the (b, c) plane [112], and a broad maximum of height $C/$R$= 0.35 \pm 0.01$ at $T_{max} \simeq 2$ K. This broad maximum is interpreted as a crossover from a paramagnetic to a spin–liquid (SL) state, with well developed short–range AFM spin-spin correlations [116]. However, in this experiment the value and the position of the maximum associated with the SL boundary coincide with that expected for the spin–1/2 Heisenberg chain (solid line in Fig. 5.2) if one considers only the high–field coupling constant $J = 4.3$ K. This model
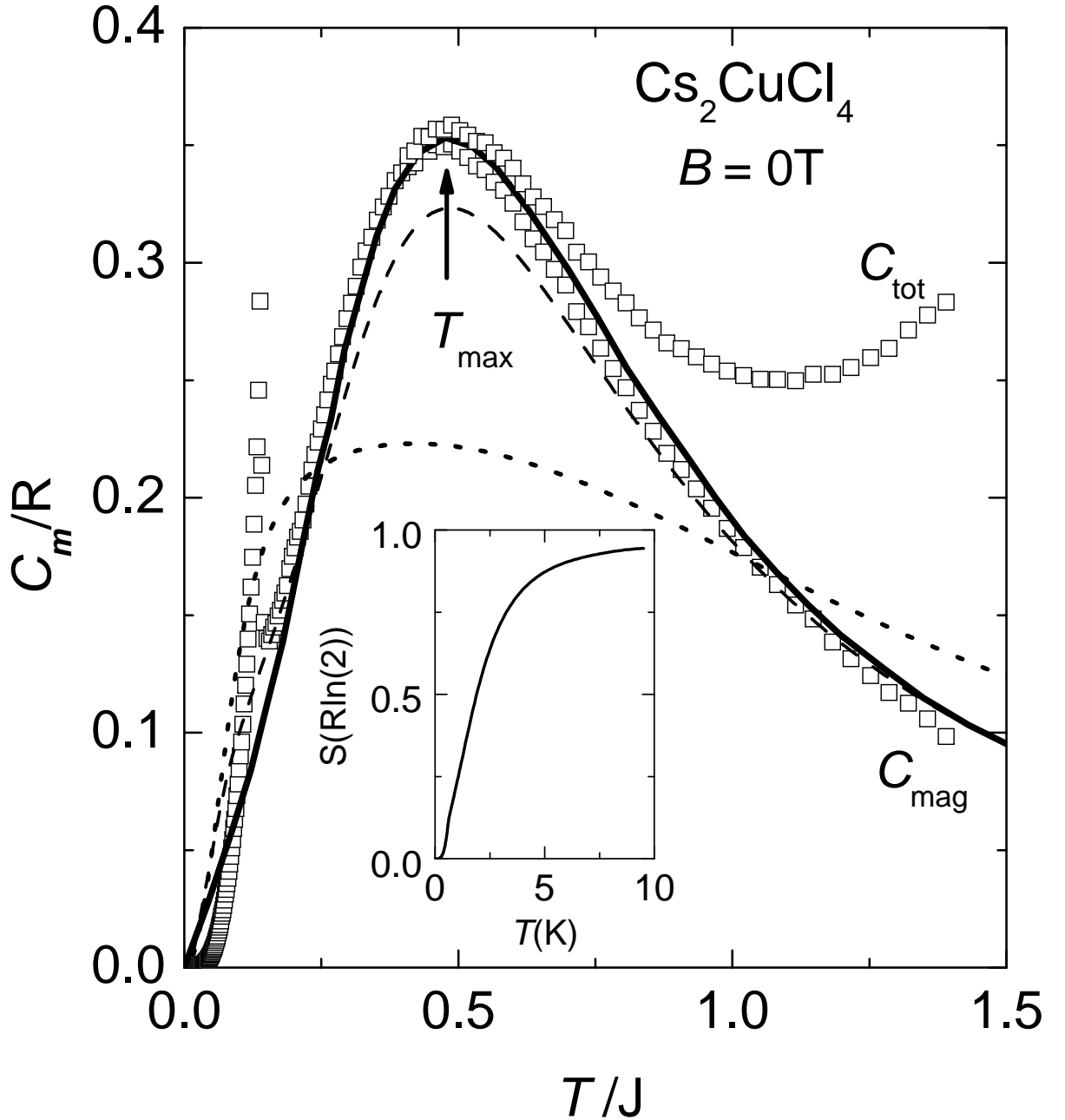
Figure 5.2: *Specific heat per mole of Cs_2CuCl_4 in units of R in zero magnetic field. From the total specific heat, C_{tot}, the phonon contribution has been subtracted (see text) to obtain the magnetic part, C_m. The solid line represents the prediction for the spin–1/2 antiferromagnetic uniform Heisenberg chain [121]. The dashed line is calculated using high–temperature series expansions with the realistic J, J' $(J'/J = 1/3)$, [122]. The dotted line represents $C_m(T)$ for an isotropic triangular lattice $(J = J')$ [16]. Inset: Magnetic entropy per mole of Cs_2CuCl_4.*

for $C(T)$ for non-interacting 1D Heisenberg chains was obtained by solving numerically the non-linear integral equations presented in Klümper's paper [121] and coincides well with our experimentally obtained specific–heat data in the whole temperature range, $T \geq T_N$. This seems to show that above T_N interchain interactions are destroyed by thermal fluctuations. The dashed line in Fig. 5.2 represents C/R for the 2D anisotropic triangular lattice, obtained within the 5th order high–temperature series expansion [123], extrapolated to low temperature using the Bernu and Misguich procedure [16]. This model is appropriate to Cs_2CuCl_4 because it takes into account the realistic J and J'. The overall shape of the specific heat in both models are similar to the data obtained experimentally; the broad peak position appears at essentially the same T/J; the only manifestation of the frustrated couplings $J'/J = 1/3$ (dashed line) is a small $\sim 10\%$ depression of the peak value in contrast to the experimental results. This difference can be understood since this model is an approximation, and not an exact calculation.

The comparison between the experimental data and the theoretical model for a 2D isotropic triangular lattice ($J = J' = 0.375$ meV) [16] shown by dotted line in fig. 5.2 was also done. The overall shape of the zero–field specific heat shows significant differences. Such differences are expected since Cs_2CuCl_4 is an anisotropic triangular lattice with $J'/J = 1/3$, not 1. This comparison shows that with decreasing the J'/J ratio, the position of the broad peak shifts up in temperature, close to the 1D case.

The evolution of the magnetic entropy with increasing temperature provides valuable information on the variation of the low–energy spectrum of excitations. The normalized magnetic entropy, S_{mag}, obtained by integrating the magnetic specific heat, is plotted in the inset of Fig. 5.2. At low temperatures, the transition at T_N results in a change of slope of S_m, indicating that this transition is not of first order. The entropy starts to saturate at $T \simeq 10$ K before reaching the $R \ln 2$ value, expected for a spin–1/2 system. Thus, S_{mag} recovers the full entropy $R \ln 2$ for spin-1/2 near 10 K, which corresponds roughly to the bandwidth of the measured spin excitations. We can define here an energy scale of $\sim 2J$ ($\sim 8K$). If one exceeds this, the system enters the paramagnetic state.

5.2.3 Bose - Einstein Condensation of magnons

First we describe the change of the specific heat in a magnetic field applied perpendicular to the spiral plane (bc) (Fig. 5.3). C_{mag} is determined by subtracting from the total heat capacity $C_{tot}(T)$ the contributions we determined in zero field, described above, and the nuclear Zeeman contribution $C_{\mathrm{hf}} = \alpha(B)/T^2$ deduced from a linear fit to the low temperature data ($T \leq 0.15$ K) in a $C_{tot}T^2$ vs T^3 plot with $C_{\mathrm{nuc}} = \alpha(B)/T^2 + \alpha_Q/T^2$. The obtained $\alpha(B)$ values are plotted in the inset of Fig. 5.3. In this plot the extrapolation to $B = 0$ yields $\alpha_Q = 38 \times 10^{-6}$ JKmol^{-1}. This value is in agreement with $\alpha_Q = 33 \times 10^{-6}$ JKmol^{-1} reported in section 5.2.2. Furthermore, the slope of the $\alpha(B)$ vs B^2 plot represents the nuclear magnetic dipolar interaction, $\alpha_{dip} = 11.46(50)\mu$JKmol^{-1}T^{-2} which is in very good agreement with the estimated value, 11μJKmol^{-1}T^{-2} using NMR data [82].

As shown in Fig. 5.3, the position of the broad maximum and the ordering temperature hardly changes for small fields, $B \leq 4$ T. Only the shape of the broad peak changes with field and becomes broader at higher fields. The broad maximum is probably still there even for $B > 4$ T but the location of the maximum, T_{max}, is difficult to determine because the high–temperature tail of the sharp transition at lower temperatures overlaps with the low–temperature tail of the broad peak. Therefore, from our measurements, it is hard to extract the evolution of this feature with magnetic field.

The transition temperature to the spiral ordered state, which can be regarded as a cone–like structure [116] is clearly visible as a sharp anomaly in $C_m(T)$ with T_N nearly constant in this low–field regime (see inset of Fig. 5.3). However, it varies very strongly above 8 T. As shown in Fig. 5.4, with increasing field the λ–like anomaly in $C_m(T)$ is gradually suppressed in its height and its position is pushed to lower temperatures. An extraordinary change occurs as the field is increased from 8.4 T to 8.44 T (see inset of Fig. 5.4). Within this tiny field change ($\Delta B/B < 0.5\%$), T_N is reduced by almost a factor of two ($T_N = 0.075(4)$ K at 8.44 T), nearly one order of magnitude below its value in zero field. No further evidences of the transition can be resolved from our data upon approaching the critical field, $B_{c^a} \simeq 8.5$ T. Thus, for $B > B_c$ the transverse component
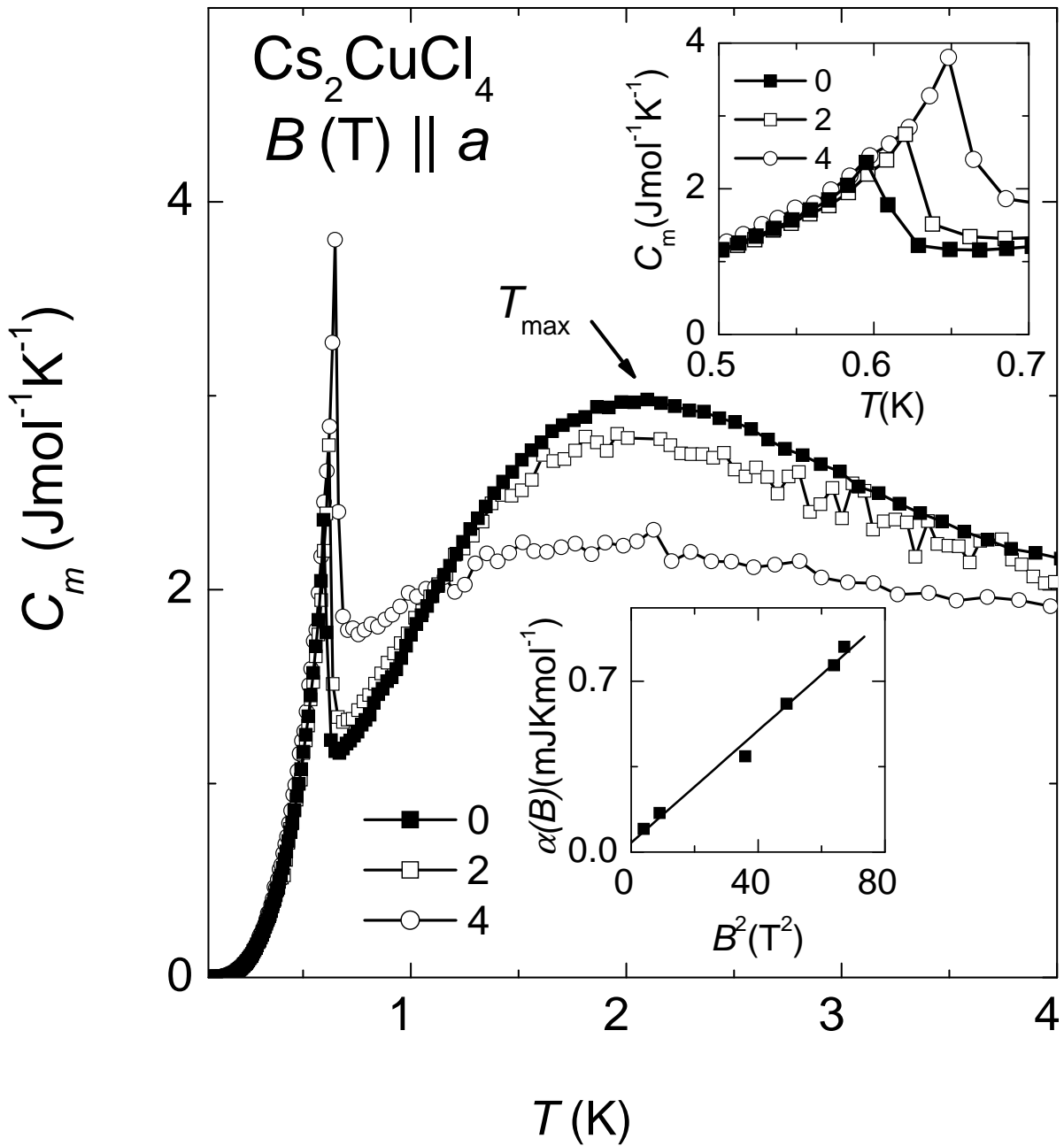
Figure 5.3: C_m vs T of Cs_2CuCl_4 at low magnetic fields, $B \leq 4$ T, applied perpendicular to the (bc) plane. The top inset shows the same data for $0.4\ K \leq T \leq 0.8\ K$. The $\alpha(B)$ vs B^2 dependence (for $B < B_c$) in the bottom inset shows the expected linear behavior.
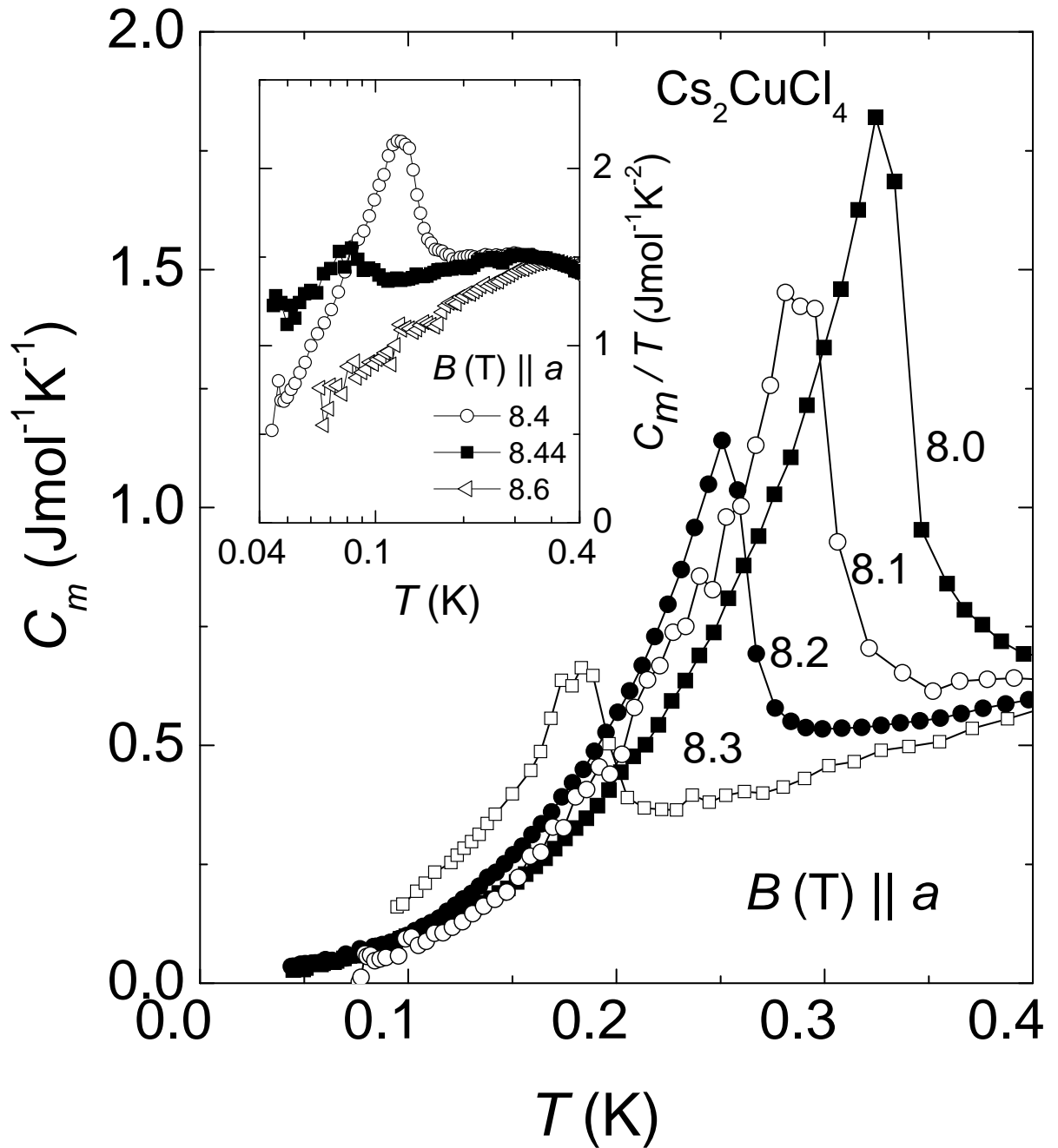
Figure 5.4: C_m vs T of Cs_2CuCl_4 at high fields close to the critical field. A small increment in the field leads to a strong decrease of T_N and a considerable reduction of the jump height. Inset: C_m/T vs T in a semi–logarithmic plot. For $B = 8.44$ T, a broad anomaly is observed at $T_N = 75 \pm 4$ mK, indicating the vicinity of the critical field ($B_c \simeq 8.51$ T).

of the ordered magnetic moment completely disappears and the spin system enters a field–induced ferromagnetic (FM) state [116].

In the field–induced FM state, $B > B_c^a$, a gap, Δ, in the magnon–excitation spectrum was earlier observed in the neutron–scattering measurements [116]. Its field dependence was given to be $\Delta = g\mu_B(B - B_c^a)$ with $g = 2.19(2)$ and μ_B the Bohr magneton [116]. Accordingly, if for $B < B_c^a$ and $T < T_N$ the spin–excitation spectrum is gapless, the gap appears at $B > B_c^a$ and increases linearly with $(B - B_c^a)$. Therefore, a line of crossover temperatures below which the gap opens is expected. The measured magnon dispersion relations in the saturated phase [116] indicated strong 2D character. The magnon dispersion along the a direction, perpendicular to the 2D layers was found to be very small, ~ 0.05 K, due to a weak interlayer spin coupling. Therefore it is unlikely that the specific heat in the gapped FM phase and for $T \gg 50$ mK is sensitive to the dispersion in the a direction.

As a consequence, for temperatures well above a characteristic energy scale $E^* \approx 50$ mK, the actual magnon dispersion is of 2D character. However, for $T \lesssim E^*$ a smooth cross-over to a 3D character is expected. Assuming first a 2D quadratic magnon dispersion, the leading contribution to the temperature dependence of the specific heat is given by $C_{mag} \simeq \exp(-\Delta/T)/T$, provided that $T < \Delta$. As shown in Fig. 5.5, this behavior fits well the experimental data above 0.3 K. The obtained field dependence of $\Delta(B)$ is discussed below. The deviation from a straight line of the 9 T data below 0.3 K in Fig. 5.5 might indicate the cross-over from 2D to 3D magnons. Actually with lowering T, the low–energy 3D magnons become gradually the dominant excitations contributing to $C(T)$. This notion is supported by the low-temperature data plotted as $C_m\sqrt{T}$ vs $1/T$ in the inset to Fig. 5.5. This presentation is used since a 3D dispersion relation yields as leading term in the specific heat $C_{mag} \simeq \exp(-\Delta/T)/\sqrt{T}$. The straight line below ≈ 0.15 K indicates that this model describes the data appropriately. However, in this cross-over region, the 2D model describes the data equally well and the determined value of the gap is (within the error bar) the same as the one deduced from the $C_{mag}T$ vs $1/T$ plot.
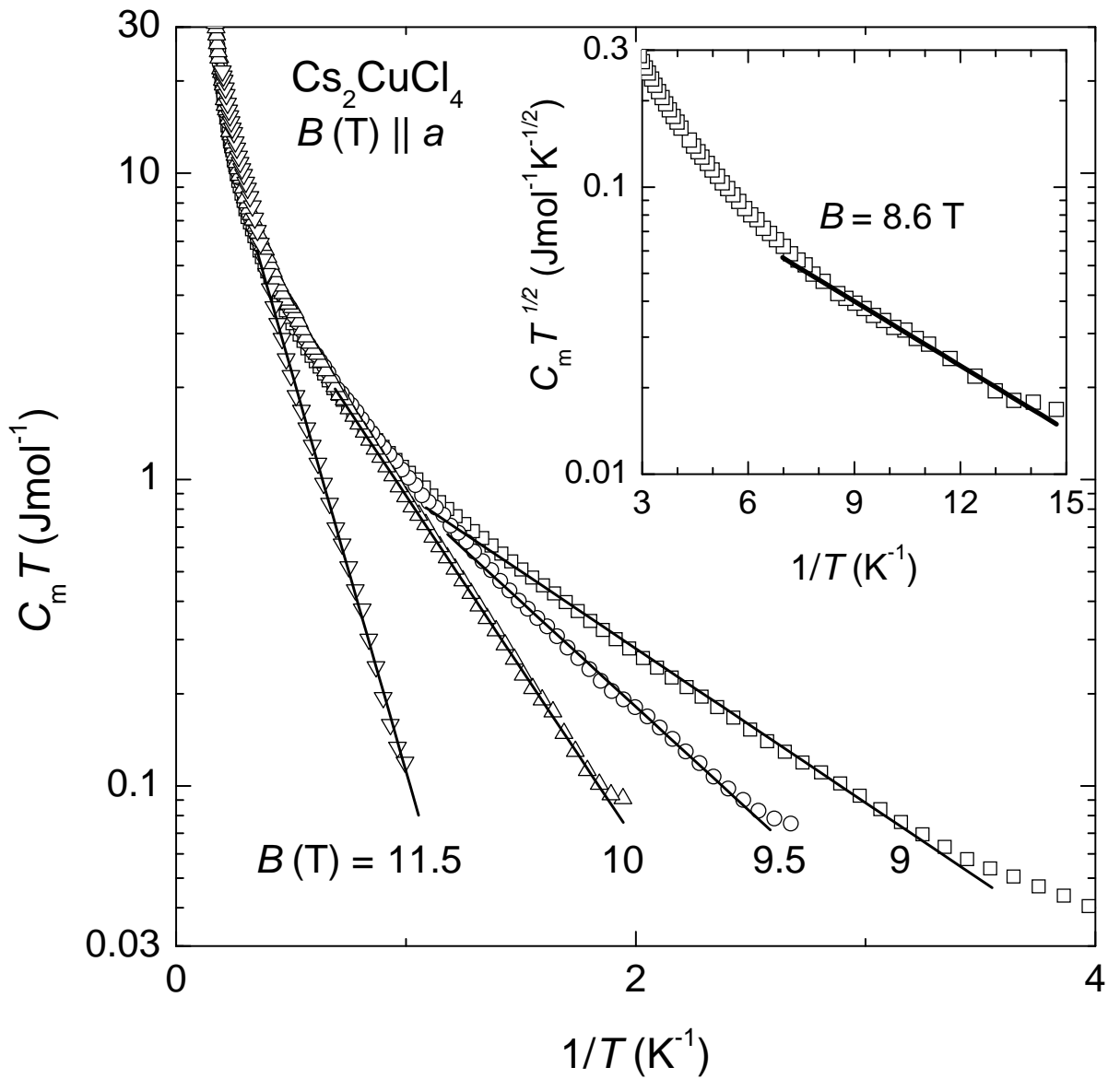
Figure 5.5: *Semilogarithmic plot of $C_m T$ vs $1/T$ of Cs_2CuCl_4 for fields above B_c. In this representation the slope of the data (solid lines) yields the value of the gap Δ present in the magnon–excitation spectrum. The data shown in the inset were obtained at $B = 8.6$ T and are plotted as $C_m\sqrt{T}$ vs $1/T$.*

The (T, B) phase diagram of Cs$_2$CuCl$_4$ obtained from our specific–heat experiments is presented in Fig. 5.6. The field dependence of the magnetic transition temperature is in very good agreement with $T_N(B)$ obtained from neutron data [122]. The specific–heat data, however, revealed that T_N starts to decrease strongly above 8 T and $T_N \rightarrow 0$ for $B \rightarrow B_c$. Thus, the Néel temperature is field dependent, $T_N(B) = f(B - B_c^a)$, and the end point of this phase boundary is the QCP. Our aim was to measure $C(T, B)$, with a special emphasis on the critical region near the QCP. These measurements were motivated by a recent suggestion that the field–induced magnetic phase transition can be understood as a magnon BEC. Instead of T_N, we label the transition temperature T_c in the field range near B_c, in order to follow the nomenclature used in the theoretical description. Fitting the power–law dependence

$$T_c(B) \propto (B_c - B)^{1/\phi} \tag{5.1}$$

to the data for $B \geq 8$ T with the assumption of $B_c^a = 8.50$ T yields an exponent $\phi = 1.52(10)$ which can be indeed understood in the framework of BEC of magnons.

However, we want to stress that the value of ϕ is very sensitive to the chosen value of B_c. An exponent $\phi = 1.44(10)$ is obtained if $B_c^a = 8.51$ T is used. The solid line plotted in the inset to Fig. 5.6 represents the result of the theoretical analysis described below. Above B_c^a the fully spin-polarized FM state is created and the gap Δ opens in the spin–excitation spectrum. For the interpretation of the phase transition below B_c as a BEC of magnons it is crucial that the gap closes at B_c. To provide a compelling evidence for this fact we re-examined the phase diagram [116] above B_c with our thermodynamic measurements. The results are presented in Fig. 5.6 (filled diamonds). The Δ values are found to be consistent with those reported from the neutron–scattering experiments [116]. These data can be used as a method to estimate independently B_c; The dashed line in Fig. 5.6 represents a linear fit of $g\mu_B(B - B_c)$ with μ_B the Bohr magneton. One obtains $B_c \simeq 8.49(10)$ T and $g = 2.13(15)$. It is noteworthy that the relatively large error bar at high B is caused by the rather narrow T range used for the fit.

Thus, for $B < B_c$, the phase transition from the paramagnetic phase ($T > T_c$) to
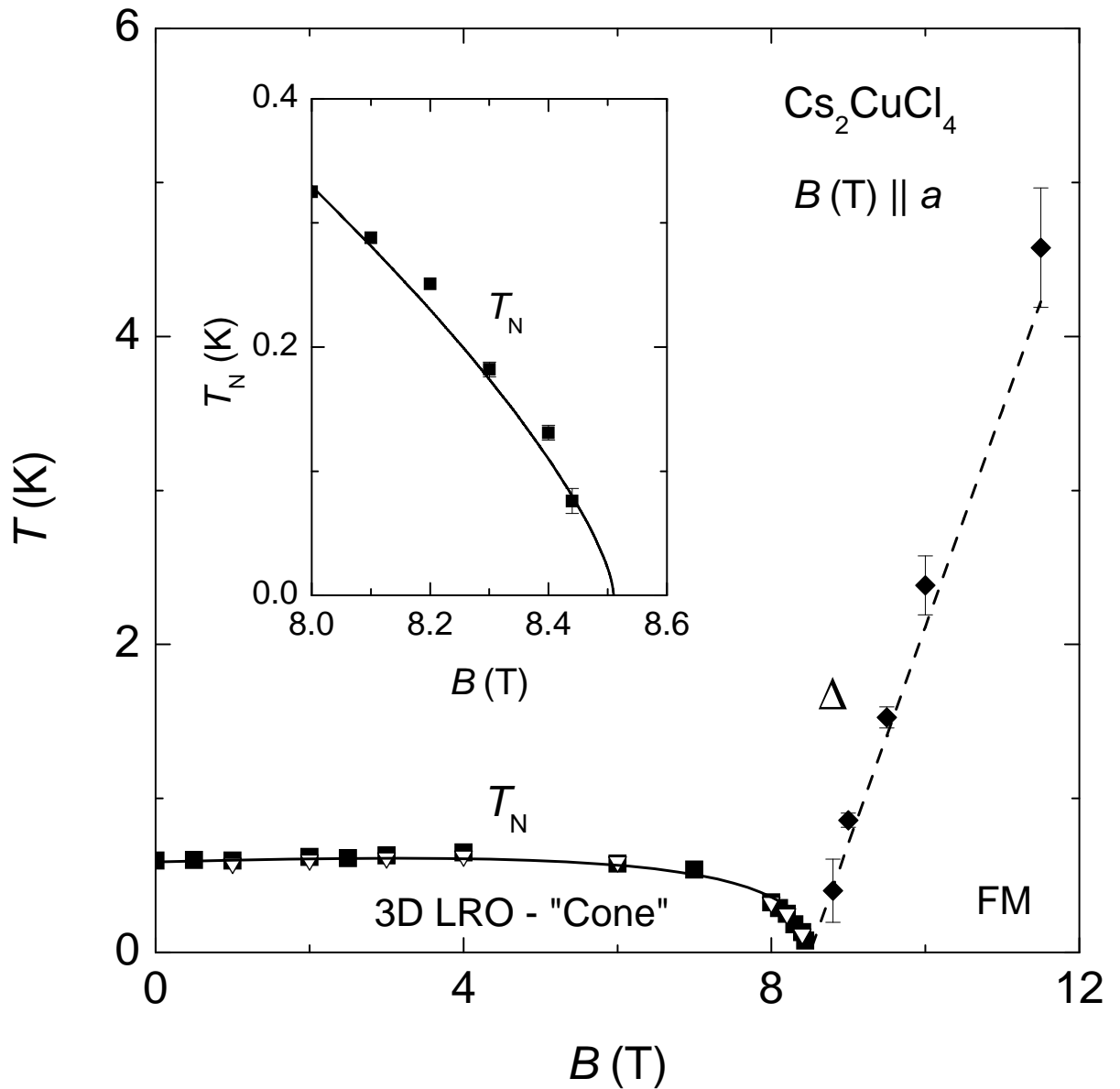
Figure 5.6: *(T, B) phase diagram of Cs_2CuCl_4 for $B \parallel a$. The ordering temperature T_N decreases as the magnetic field approaches the critical field $B_c = 8.51$ T. Open symbols are neutron–scattering data [122]. Above B_c a field-polarized ferromagnetic (FM) state is entered and the gap Δ in the spin–excitation spectrum opens. Inset: The experimental $T_N(B)$ data points are well described by the calculated phase boundary of the BEC of magnons (solid line).*

the ordered spiral phase ($T < T_\text{c}$) will be described below as the magnon BEC. The measurements of the specific heat, $C(T)$, suggested that the transition is of second order. For instance, for all $B < B_c$ the specific heat as a function of temperature shows a peak of an asymetric λ shape at the transition temperature T_c as shown in the previous section. The phase boundary curve behaves like $T_\text{c} \sim (B_{sat} - B)^{1/\phi}$ with some critical exponent ϕ. Here one of our main goals is to compare the measured and the calculated values of the critical exponent ϕ.

To describe the magnon BEC in Cs$_2$CuCl$_4$ [124], the main steps of the theoretical approach are the following. First the theory is based on the quasi–2D spin–1/2 AFM Heisenberg model on a spatially anisotropic triangular lattice. The exchange spin couplings J, J', and J'' for Cs$_2$CuCl$_4$ are taken from the inelastic neutron–scattering measurements [116]. Effects of the magnetic anisotropy are studied in an extended version of the spin model including DM spin coupling of the strength D reported in [112, 116]. The use of the hard–core boson representation for the spin–1/2 operators [5, 6, 8] to treat the observed phase transition slightly below the saturation field B_c as a BEC of magnons allows one to map the original spin model onto the Hamiltonian of interacting bosons. This mapping is valid if the boson Hilbert space is restricted to forbid on–site occupancy larger than unity. We used the hard-core boson representation for spin-1/2 operators $S_i^\pm, S_i^z$ in the original Hamiltonian H,

$$H = H_0 + H_{DM} + H_B, \tag{5.2}$$

which involves the isotropic exchange H_0, the DM anisotropic term H_{DM}, and the Zeeman energy H_B.

Because the DM interaction ($D = 0.053(5)J$ [116]) changes sign between even and odd magnetic layers, which are stacked along the a direction, two types of bosons, a_i and b_j are introduced for the two types of layers. This can be achieved through $S_i^+ \to a_i$, $S_i^- \to a_i^+$, and $S_i^z = 1/2 - a_i^+ a_i$, and a similar description for b_j [125]. The hard-core boson constraint was satisfied by adding to H an infinite on-site repulsion, $U \to \infty$, between bosons given by

$$H_U^{(a)} + H_U^{(b)} = U \sum_i a_i^+ a_i^+ a_i a_i + U \sum_j b_j^+ b_j^+ b_j b_j. \tag{5.3}$$

The interlayer coupling $J'' = 0.045(5)J$ [116] mixes a and b boson modes and results in two bare magnon–excitation branches A and B. Their dispersion relations are given by [116]

$$E_q^{A,B} = J_q \mp \mathrm{sign} \mathrm{D_q} \sqrt{\mathrm{D_q^2} + \left(\mathrm{J_q''}\right)^2} - \mathrm{E_0}, \tag{5.4}$$

with

$$J_q = J \cos q_x + 2J' \cos (q_x/2) \cos (q_y/2) \ , \tag{5.5}$$

$$D_q = 2D \sin (q_x/2) \cos (q_y/2) \ , \tag{5.6}$$

$$J_q'' = J'' \cos (q_z/2) \ . \tag{5.7}$$

Here $J' = 0.34(3)J$ [116] and the q values are restricted to $0 \le q_x < 2\pi$, $0 \le q_y < 4\pi$, and $0 \le q_z < 2\pi$.

The degenerate minima $E_{\vec{Q_1}}^A = E_{\vec{Q_2}}^B = 0$ are at $\vec{Q}_1 = (\pi + \delta_1, 0, 0)$ for branch A and at $\vec{Q}_2 = (\pi - \delta_2, 2\pi, 0)$ for branch B. Without loosing precision we can use $\delta_1 \simeq \delta_2 \simeq \delta = 2 \arcsin (J'/2J)$. The bilinear part of H now reads

$$H_{bil} = \sum_q \left[\left(E_q^A - \mu_0 \right) A_q^+ A_q + \left(E_q^B - \mu_0 \right) B_q^+ B_q \right], \tag{5.8}$$

with $A_q = \alpha_q a_q + \beta_q b_q$, $B_q = \alpha_q b_q - \beta_q a_q$, $\alpha_q^2 + \beta_q^2 = 1$, and the bare chemical potential $\mu_0 = g\mu_B (B_c - B)$. The saturation field $B_c = W/(g\mu_B)$, with W being the magnon bandwidth, was calculated to be $B_c = 8.51$ T assuming $g = 2.20$ [125, 126].

The interaction given by eq. (5.3) describes the scattering of A and B magnons. Near the quantum critical point, $(B_c - B) \ll B_c$ and at low temperature, the average density of magnons $n^A = n^B = n$ is low, $n \sim (1 - B/B_c)$. Here, $n^{A/B}$ is a temperature and field–dependent density of A or B magnons.

$$n^{A/B} = \int d\varepsilon \frac{\rho^{A/B}(\varepsilon)}{e^{\beta(\varepsilon^{A/B} - \mu_{eff})} - 1} \tag{5.9}$$

.

The magnon scattering can be treated in the ladder approximation [127], neglecting interference between the a and b channels. In this approximation, the problem reduces to solving the Bethe–Salpeter equation in each channel.

This results in the renormalized scattering amplitudes $\Gamma^{(i)}(\vec{q}_1, \vec{q}_2; \vec{q}_3, \vec{q}_4)$ for $i = a, b$. Here $\vec{q}_3, \vec{q}_4$ and $\vec{q}_1, \vec{q}_2$ are magnon momenta before and after scattering, respectively, and $\vec{q}_1 + \vec{q}_2 = \vec{q}_3 + \vec{q}_4$. The total energy of scattered magnons was set to zero. This limit is compatible with our main goal to describe the phase transition near B_c when approaching the phase boundary $T_c(B)$ from higher temperatures. At $T \to T_c$, only the magnon states at $\vec{q} \simeq \vec{Q}_{1,2}$ are occupied and the magnon–spectrum renormalization near the minima is important.

With given $\Gamma^{(a)}$ and $\Gamma^{(b)}$, the complete set of two-particle scattering amplitudes was then obtained by multiplying $\Gamma^{(a),(b)}$ by products of four α_q and β_q coefficients. For instance, a scattering process $(A_{\vec{q}_3}, B_{\vec{q}_4}) \to (A_{\vec{q}_1}, B_{\vec{q}_2})$ in the channel a is described by the amplitude $\alpha_{q_1} \beta_{q_2} \alpha_{q_3} \beta_{q_4} \Gamma^{(a)}(\vec{q}_1, \vec{q}_2; \vec{q}_3, \vec{q}_4)$.

The renormalization of low-energy magnons was found by treating the magnon scattering effects in the Hartree-Fock approximation:

$$
\begin{aligned}
H_{int}^{MF} = \quad & 2\Gamma n \sum_q \left(A_q^+ A_q + B_q^+ B_q \right) \\
& + 2\Gamma' \alpha \beta n \sum_q \left(A_q^+ B_q + B_q^+ A_q \right),
\end{aligned}
\tag{5.10}
$$

where $\alpha_{Q_1}^2 = \alpha_{Q_2}^2 \equiv \alpha^2$ and $\beta_{Q_1}^2 = \beta_{Q_2}^2 \equiv \beta^2$. Taking into account that $\alpha^2 \gg \beta^2$, we keep here only the leading contributions to energy parameters Γ and Γ':

$$
\begin{aligned}
\Gamma \quad & \simeq \alpha^4 \Gamma^{(a)} \left(\vec{Q}_1, \vec{Q}_1; \vec{Q}_1, \vec{Q}_1 \right) \\
& = \alpha^4 \Gamma^{(b)} \left(\vec{Q}_2, \vec{Q}_2; \vec{Q}_2, \vec{Q}_2 \right), \quad \Gamma' \simeq 2\Gamma/\alpha^2,
\end{aligned}
\tag{5.11}
$$

and we obtained the estimate $\Gamma \simeq 0.85J$. According to eq. (5.10), the chemical potential of magnons is renormalized $\mu_0 \to \mu_{eff} = \mu_0 - 2\Gamma n$, and the low-energy magnons

are hybridized due to the second term in eq.(5.10). This term shifts the bottom of the magnon band slightly down and leads to a weak mass enhancement of low-energy magnons. Both effects are proportional to n^2 and we omit them since $n \ll 1$ near T_c for $(B_c - B) \ll B_c$.

For a given $B \lesssim B_c$ and with decreasing temperature the magnon BEC occurs when the effective chemical potential μ_{eff} vanishes [8]. Then $T_c(B)$ is determined by

$$g\mu_B \left(B_c - B\right) = 2\Gamma n \left(T_c\right) \ . \tag{5.12}$$

Here $n\left(T\right) = \sum_q f_B\left(E_q\right)$ with $f_B\left(E_q\right)$ being the Bose–distribution function taken at $\mu_{eff} = 0$ and $E_q = E_q^A$ or $E_q = E_q^B$. This means that for $T < T_c$ the magnon condensate develops simultaneously at $\vec{q} = \vec{Q}_{1,2}$. It is worth emphasizing that at $\mu_{eff} \to 0$ the distribution function $f_B(E)$ diverges as T/E for $E \to 0$. Therefore, the low–energy 3D-magnon spectrum, $E < E^*$, mainly contributes and drives the BEC transition. The phase boundary can be calculated using eq. (5.12). It gives a very good description of the experimental data near B_c (see inset to Fig. 5.6), but deviates strongly at lower fields, i.e., for $B_c - B > 0.5$ T. This indicates that the mean-field description of the magnon BEC is only applicable in the close vicinity of B_c. The calculated boundary is well described by eq. (5.1) with a critical exponent $\phi_{th} \simeq 1.5$ close to the predicted value $\phi_{\mathrm{BEC}} = 3/2$ characteristic for 3D quadratic dispersion of low-energy magnons [8, 128].

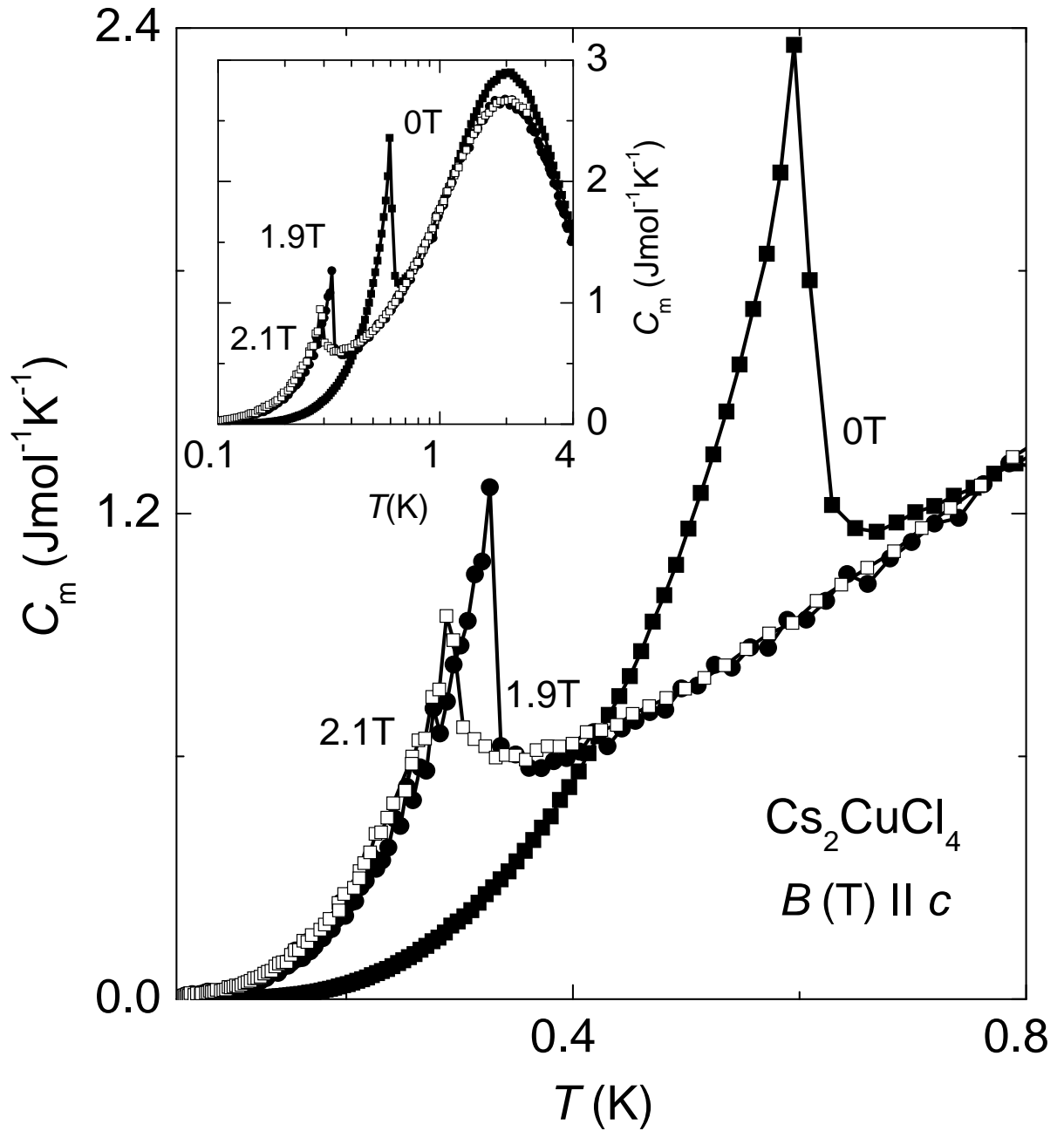## 5.2.4 Phase diagrams for $\vec{B} \parallel c$ and $\vec{B} \parallel b$

Fig. 5.7 shows the temperature dependence of the magnetic specific heat in various magnetic fields applied parallel to the crystallographic c axis. It is noteworthy that C_m was subtracted from the raw data in the same way as we did for $B \parallel a$ (see the section above) and $\alpha(B)$ vs B^2 showed the same linear behavior.

With fields less than 2.1 T, $C_m(T)$ shows similarities to the situation when the magnetic field is applied along the a axis: a single λ–like anomaly and a broad maximum at higher temperatures (see inset Fig. 5.7). For $B = 1.9$ T, $C_m(T)$ exhibits a clear λ–shape peak at $T_N = 0.326$ K. A small increase of the field to $B = 2.1$ T shifts the transition to a

slightly lower temperature, $T = 0.288$ K accompanied by a significant reduction of the peak width by almost a factor of two. In the inset the same data show the evolution of $C_m(T)$ in the temperature range 0.1 K $\leq T \leq 4$ K in a semilogarithmic plot. The position of the broad maximum does not vary with B in this low–field range.

A remarkable change in C_m occurs as the field is increased above 2.1 T. T_N start to increase with increasing field and is observed at 0.302 and 0.341 K for $B = 2.2$ and 3 T, respectively (see inset–top Fig. 5.8) whereas the size of the peaks is reduced. For $B = 3.8$ T two sharp peaks in the specific heat can be resolved at 0.220 T and 0.371 K, respectively (main part of Fig. 5.8). As the field increases to $B = 4$ T the position of the latter one remains almost unchanged, $T = 0.371$ K while the second peak is shifted to an even lower temperature, $T = 0.171$ K. Thus, the separation between the peaks increases. With further increasing the field to $B = 5$ T (inset–bottom Fig. 5.8), the temperature position of the dominant λ–like anomaly remains almost constant ($T = 0.371$ K). Only the lower peak is shifted to higher temperature, $T = 0.310$ K. As a consequence, the separation between the two peaks decreases. Moreover, for $B = 6$ T they are still distinguishable and appear at $T = 0.334$ K and $T = 0.322$ K, respectively. A further increase of the field leads to the suppression of both transitions; for $B = 8$ T no anomaly was observed in specific–heat measurements down to 0.08 K. Note that the position of the broad maximum is not affected by the applied magnetic field for $B \leq 4$ T, it is still clearly visible at ~ 2 K like in $B = 0$. However, for higher fields, it is not any longer observed in $C_m(T)$, similar to the situation when $B \parallel a$, discussed above.

The specific–heat data show many similarities when B is aligned along the c and b axis. When B is applied along the crystallographic b axis the transition is split into two close peaks for $B = 3$ T (Fig. 5.9). This double structure can still be seen in C_m vs T until $B = 6$ T and then vanishes with increasing field (see inset of Fig. 5.9). Similar to the case $B \parallel c$, the temperature position of the dominant λ–like anomaly first decreases with increasing B up to ~ 2 T. Upon approaching B_c^b, for $B \geq 6$ T (Fig. 5.10) the transition temperature varies strongly, the height of the λ–like anomaly is gradually suppressed and its position is shifted downwards with increasing field. For $B = 9$ T no anomaly was

Figure 5.7: *The temperature dependence of the magnetic specific heat of Cs_2CuCl_4 in magnetic fields up to 2.1 T and $T \leq 0.8$ K, for $B \parallel c$. Inset shows the same data for $0.1\ K \leq T \leq 4\ K$ in a semilogarithmic plot.*
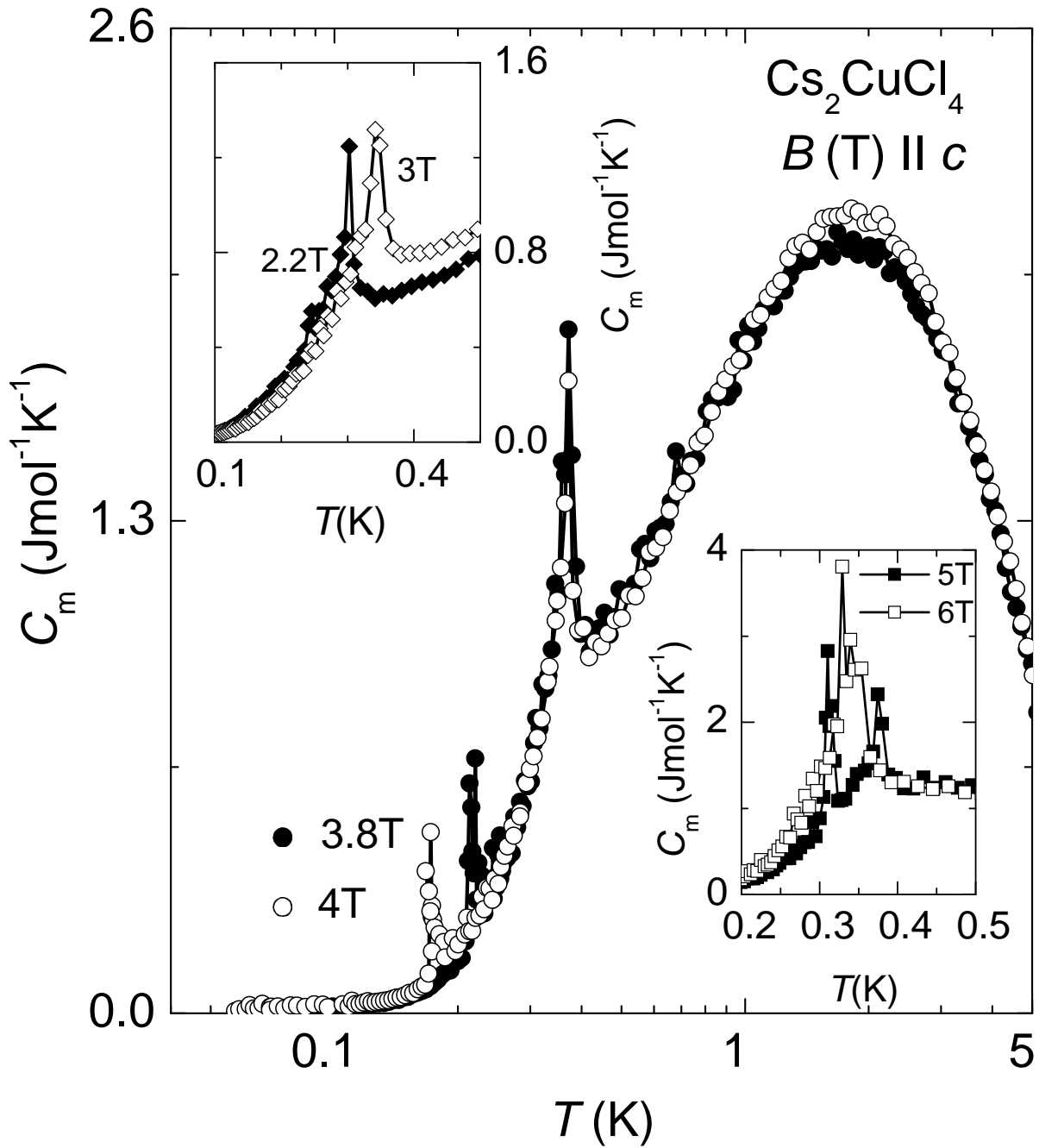
Figure 5.8: *C_m vs T of Cs_2CuCl_4 for $B = 3.8$ and 4 T in a semilogarithmic scale. Inset–top: C_m vs T for $B = 2.2$ and 3 T applied parallel to the c axis, in the temperature range 0.1 $K \leq T \leq$ 0.5 K; inset–bottom: the evolution of C_m with T in $B = 5$ and 6 T, $B \parallel c$, at low temperatures, 0.2 $K \leq T \leq$ 0.5 K.*

observed in specific heat measurements down to 0.08 K. As for the situation when $B \parallel a$ and $B \parallel c$ the broad maximum observed in specific–heat versus temperature is becoming broader with applying magnetic field and seems to disappear in a field of about 6 T. However, as discussed in the previous section it is hard to determine its evolution with magnetic field from our specific–heat data.

In Fig. 5.11(a) and (b), the magnetic field–phase diagram based on our specific–heat measurements is shown together with the data obtained form neutron scattering and magnetization measurements to complete the phase diagram. For the field along the c and b axis the phase diagrams show a much more complicated structure than that along the a axis. For $B \parallel b$ three new phases appear above the spiral phase. Two of these phases occupy a small area in the $T - B$ phase diagram. For field along the c axis it is most complicated. The system undergoes five different magnetic ordered phases in magnetic field.

Starting with $B \parallel c$, a transition occurs above ~ 1.4 T to a phase, marked II on Fig. 5.11(a), first reported by neutron–scattering measurements [119], where the order is no longer incommensurate helical as at low field. Instead, in phase II the structure is elliptical with a large elongation of the spins along the field direction. The incommensuration here, approaches a linear relation with field with a large slope, and the total ordered moment decreases with increasing field [119]. The phase II is very well observed in neutron–scattering measurements but it cannot be probed by the specific–heat measurements. Our measurements were performed at constant field and temperature variation, therefore this phase transition has not been observed. One needs magnetocalorimetric measurements to detect this transition.
Recent neutron–scattering experiments [122] have found that the intermediate field phases (III and IV) which cover most of the phase diagram in field for 2.1 T $\leq B \leq$ 7.1 T have a commensurate AFM order in the (bc) plane. This result is quite surprising as this type of ordering is not predicted by semiclassical calculations. A possible scenario could be that in applied field zero-point quantum fluctuations increase the stability of a commensurate phase compared to a classical incommensurate cone phase. For this
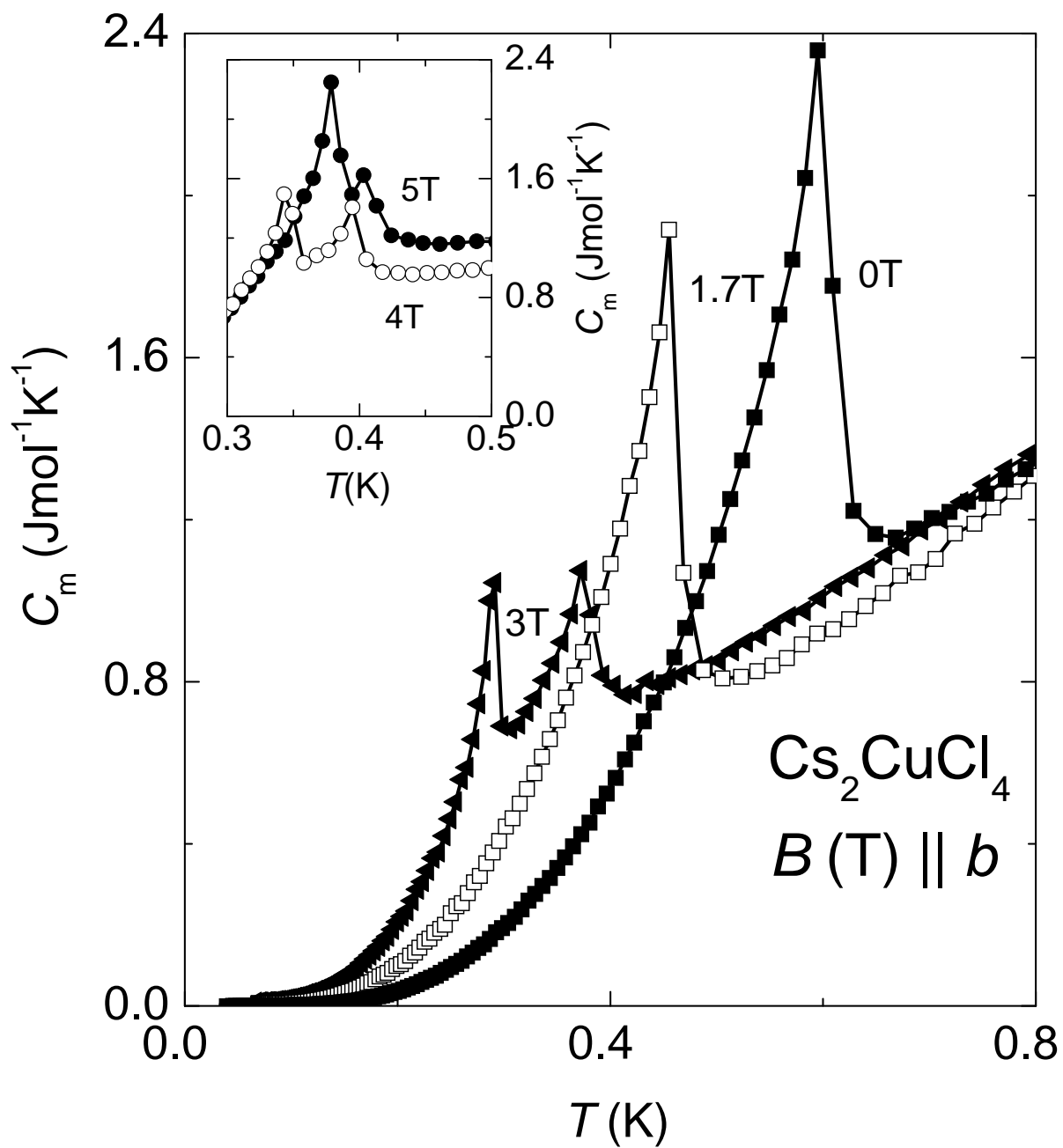
Figure 5.9: C_m vs T of Cs_2CuCl_4 at various magnetic fields, $B \leq 3$ T, applied along the crystallographic b axis. The inset shows the data for $B = 4$ and 5 T.

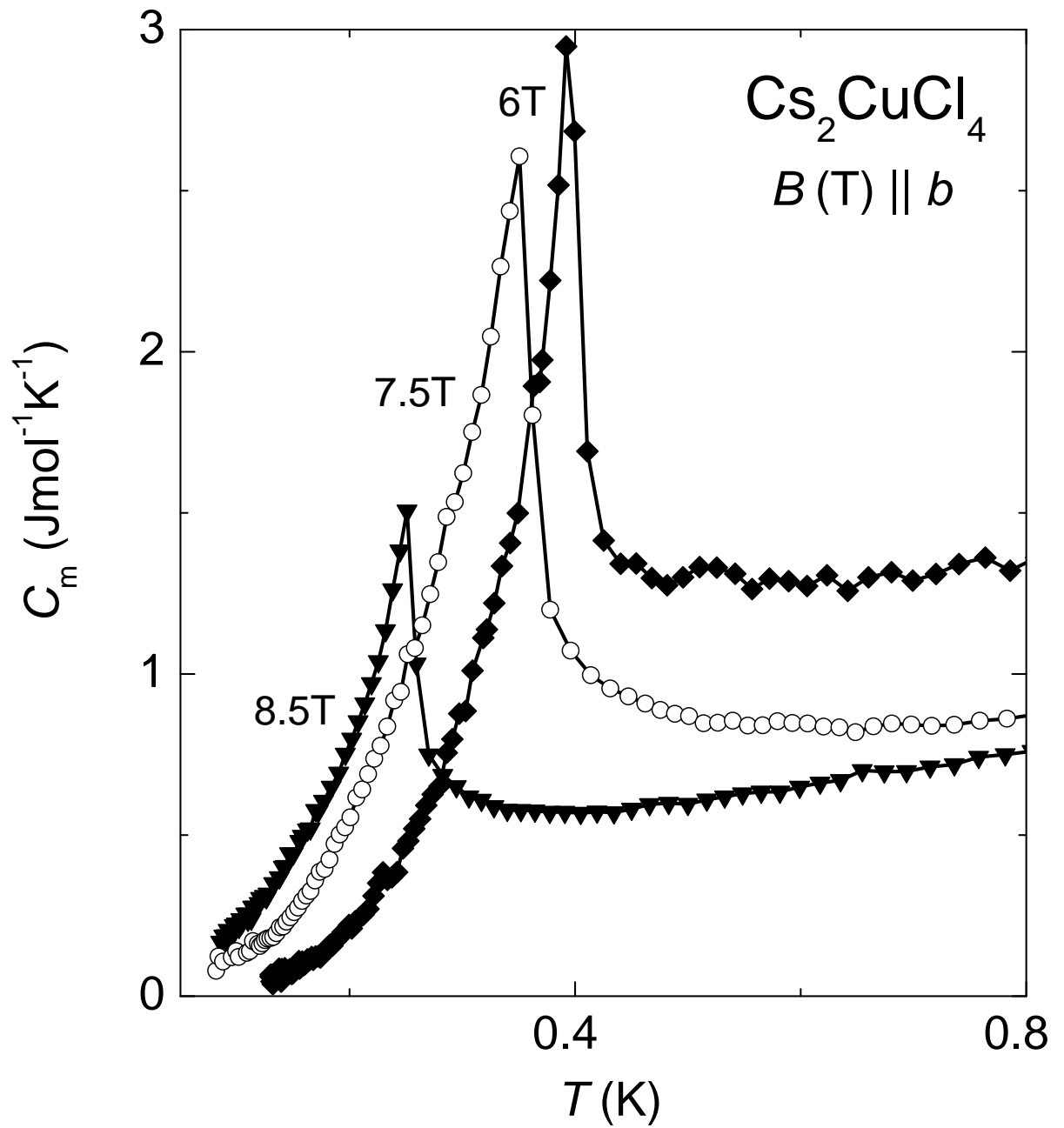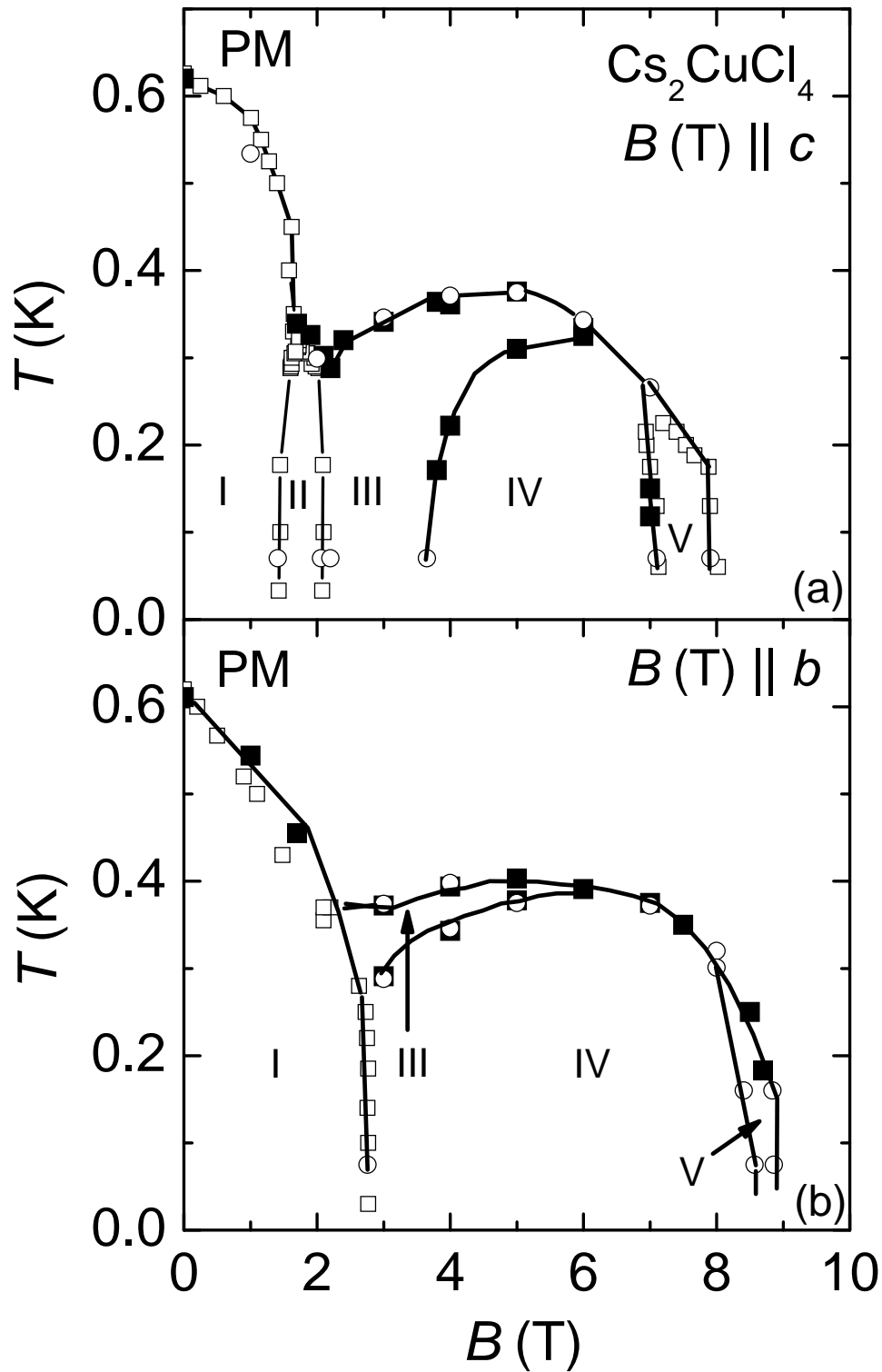**Figure 5.10:** C_m vs T of Cs_2CuCl_4 in magnetic fields up to 8.5 T for $B \parallel b$.

Figure 5.11: *T−B phase diagram of Cs₂CuCl₄ for B ∥ c (a), and B ∥ b(b), respectively. Open symbols (circles and squares) represent the boundaries of the various phases described in the text, measured using neutron scattering and magnetisation, respectively. Filled symbols (squares) show the position of the sharp peaks found in the specific–heat measurements.*

particular field orientation, the transition at 3.6 T is probably some reorientation of the spins between the layers. There is definitely a magnetic transition there also, confirmed recently by neutron–scattering measurements [122], but the structure does not change qualitatively.

Our experiments show that there are many similarities between the b and c axes. Thus, one might expect that the intermediate phases, III and IV for $B \parallel b$ are also similar to III and IV observed for $B \parallel c$ (see Fig. 5.11(a) and (b)). The high–field phase (V), near 8 T, which appears for both, $B \parallel c$ and $B \parallel b$, can be also incommensurate, most likely with spins nearly aligned along the field but tilted a bit, either in the bc plane in the form of a fan or some other form of distorted cone. Neutron data are still to be analyzed, to extract the full details of the magnetic structure.

5.3 1D spin–$1/2$ XY–like antiferromagnet Cs_2CoCl_4

5.3.1 Magnetic properties of Cs_2CoCl_4

Cs_2CoCl_4 is a quasi–one–dimensional spin–1/2 XY–like antiferromagnet with very small interchain couplings which can be studied in terms of the XXZ model [4]. Crystal–field effects lead to a strong planar anisotropy with the exchange interactions mostly restricted between the spin components in an XY easy plane.

In the tetrahedral cubic environment the orbital ground state for the Co^{2+} ions is a singlet with $S = 3/2$. Small distortions from a perfect tetrahedron combined with spin-orbit interactions will split the $S = 3/2$ orbital singlet state into two Kramers doublets with a separation, $D \simeq 15$ K [4, 129]. The magnetic exchange energy is much lower than the inter–doublet separation and therefore only the lowest-lying doublet states participate in the low–energy dynamics at low temperatures ($k_B T \ll D$). The ground–state doublet is mainly charaterized by the quantum numbers $m = \pm 1/2$, while the upper doublet corresponds to $m = \pm 3/2$ [129]. Since the coupling between the singlet and triplet state is very small one can consider the system as an effective spin–1/2 system. This explains the applicability of the $S = 1/2$ XXZ model in describing the observed magnetic

behavior of these compound.

There are two theoretical studied cases of the effects on the magnetic properties of quasi-one-dimensional antiferromagnets with anisotropic exchange interactions on the direction of the applied magnetic field. First of them is the XXZ model in the uniform longitudinal magnetic field (along the z axis). Since the longitudinal field commutes with the XXZ Hamiltonian the model is exactly solved by the Bethe ansatz and was studied in great details [1]. In the second case the field is applied in the transverse direction and the exact integrability is lost. Thus, the behavior of the XXZ model in the symmetry-breaking transverse field (noncommuting field) [2] is essentially different from the case of the longitudinal field applied along the anisotropy axis. In particular, such noncommuting terms introduce quantum fluctuations into the $T = 0$ ground state which, for large enough fields, can completely disorder the system. Such a scenario has been observed in the three–dimensional Ising ferromagnet LiHoF$_4$ in a transverse magnetic field [3]. Nevertheless, due to its high dimensionality, the system behaves in a mean–field–like way. Motivated by recent neutron–scattering results [4], in this work we consider the quasi-one–dimensional antiferromagnet Cs$_2$CoCl$_4$ and the effects of noncommuting applied field on its ground state.

Neutron–scattering measurements [4] showed that in zero field, interchain couplings cause long–range order (LRO) below $T_N = 217$ mK with the spins ordered antiferromagnetically along the chains and the moments confined to the (bc) plane (perpendicular to the anisotropy axis); noncommuting applied magnetic fields are found to initially stabilize the perpendicular antiferromagnetic order by promoting a spin–flop phase (with an increased perpendicular antiferromagnetic moment). The spin–flop phase at low fields has a small ferromagnetically aligned magnetic moment along the field. It was found that in higher fields the antiferromagnetic order becomes unstable and is suppressed at the critical field $B_c = 2.15$ T. The spins become fully aligned along the field direction above 2.5 T. The intermediate region (2.15 T $\leq B \leq$ 2.5 T) was characterized as a phase with no long–range order in the (bc) plane, proposed to be a spin–liquid phase with a finite fluctuating spin moment. This opens the possibility of checking experimentally

the existence of a spin liquid, proposed long time ago theoretically but not explored experimentally up to now. Therefore, specific–heat measurements for a range of fields to cover the whole phase diagram are very important, in particular near the critical field, ($B_c = 2.15$ T) where the gap to spin excitations, Δ, is expected to close but to be finite on either side of the transition. Measuring experimentally what happens to the spin gap across the critical point is very important in understanding the mechanism of the transition and for comparison with theory.

5.3.2 Results in zero field

Figure 5.12 shows results of the specific–heat measurements of Cs_2CoCl_4 in zero field over the whole investigated temperature range 0.07 K $\leq T \leq 6$ K on a semilogarithmic scale. It was obtained by subtracting from the raw data the contribution of the addenda and the nuclear–quadrupole contribution ($\alpha_Q = 123 \times 10^{-6}$ JKmol^{-1}). The transition at $T_N \simeq 0.22$ K, clearly visible as a very sharp first order like anomaly in $C(T)$, was interpreted as a transition to a magnetically ordered phase caused by small couplings between the chains [130]. The broad maximum of height $C/R = 0.35(1)$, characteristic of low–dimensional systems is found at $T \sim 0.9$ K. At higher temperatures, the specific heat shows a Schottky anomaly near $5 - 6$ K characteristic of excitations to a higher crystal–field level.

Figure 5.12 shows the total specific heat C_{tot}, of Cs_2CoCl_4 (open circles) completely modeled by fitting the sum of a term due to XY–like linear chains (dashed line), C_{XY}, with the exact solution for the specific heat provided by Katsura [131], plus a Schottky term (dotted line), C_{Sch}, and a phonon–like term (dash–dotted line), C_{ph}. The total fit is indicated by the solid line in this figure and gives a perfect fit of C_{tot} in the whole temperature range, $T \geq T_N$. The values obtained from the fit, $J = 3.09(1)$ K (0.267 meV), the Kramers splitting $D \simeq 15$ K (~ 1.3 meV), and the amplitude of the phonons $\beta \simeq 7 \times 10^{-3}$JK^{-4}mol^{-1} ($\theta_D \simeq 125$ K), are in good agreement with earlier estimates of J, D, and β, respectively [4, 114, 129, 130]. Open squares in Fig. 5.12 show the magnetic specific heat of Cs_2CoCl_4, $C_m(T)$, obtained after extracting from $C_{tot}(T)$
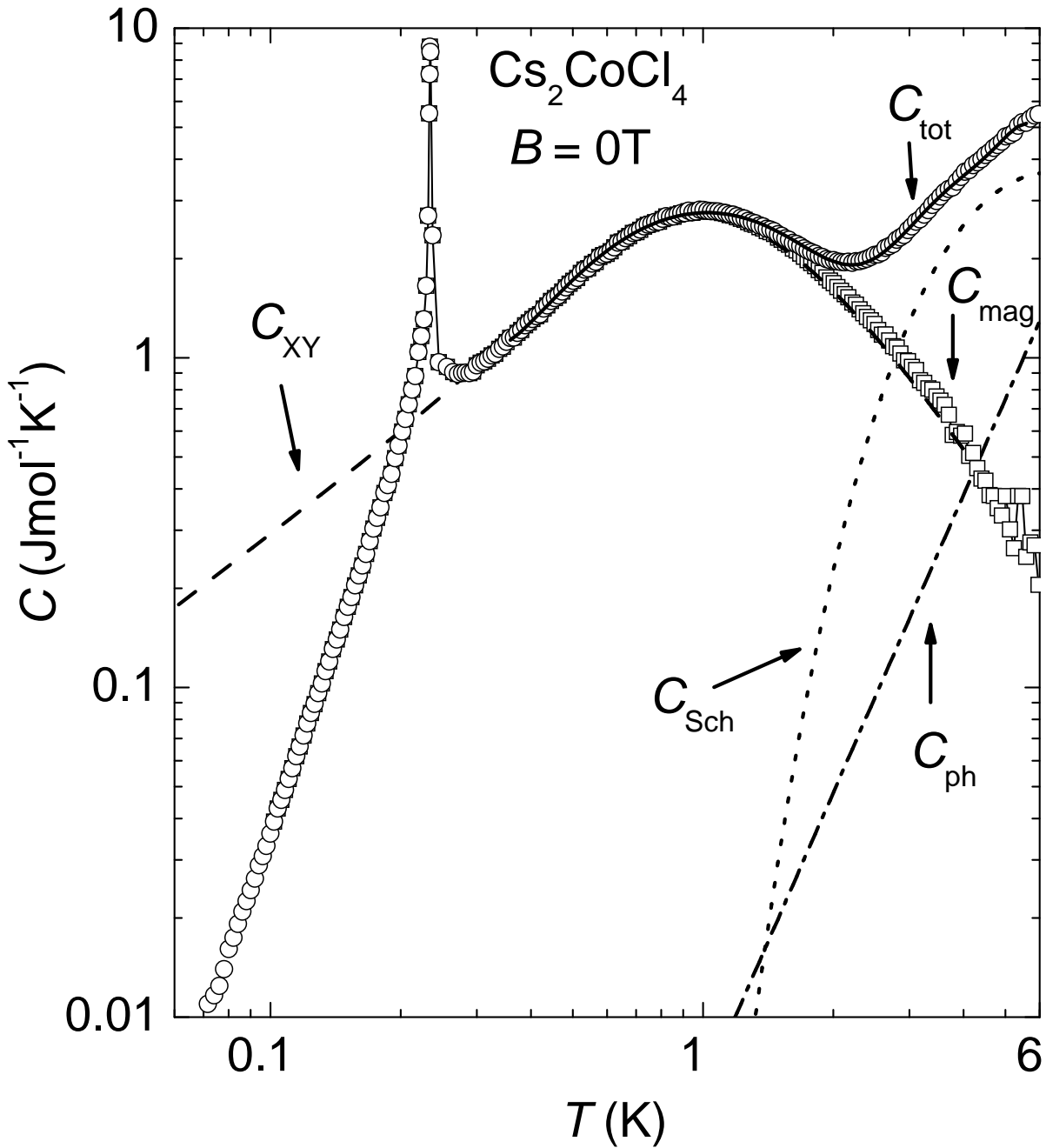
Figure 5.12: *The temperature dependence of the specific heat of Cs_2CoCl_4 in zero field and for the temperature range 0.07 K $\leq T \leq 6$ K. From the total specific heat, C_{tot}, (open circles) the phonon contribution (dashed-dotted line), C_{ph}, and the Schottky anomaly, C_{Sch} (dotted line), has been subtracted (see text) to obtained the magnetic part of the specific heat, C_m (open squares). The overall shape of C_m agrees well with the numerical predictions for an $S = 1/2$ XY–like AF chain (dashed line) with exchange coupling $J = 3.09(1)$ K (0.267 meV).*

the Schottky and the phonon contribution. Thus, we may directly compare our data below 1 K with theoretical predictions regarding the magnetic–exchange contribution. As mentioned in the introduction we expect the magnetic interaction to be of the XY type. Clearly, a good agreement is obtained between the XY linear–chain model shown by the dashed line in Fig. 5.12 and our experiment (open squares) in the entire temperature range, $T \geq T_N$. Thus, it can be concluded that not only the absolute value of T_N but also the temperature dependence of C are in good agreement with previously reported measurements [130]. However, it is worth noting, that in the earlier report, only smoothed data points have been included and this prevented the authors to see the transition as a very sharp peak. Therefore, at $T = T_N$ in Ref. [130] $C \simeq 1.8$ Jmol^{-1}K^{-1} whereas in our measurements $C \simeq 10$ Jmol^{-1}K^{-1}.

## 5.3.3 Noncommuting fields: $\vec{B} \perp \vec{b}$

First we describe the change of the specific heat under an applied noncommuting magnetic field. We carried out measurements for $B \parallel c$ up to $B = 4$ T. $C_m(T)$ for all the data discussed here, is determined by subtracting from the total specific heat C_{tot} the field–independent quadrupolar contribution $C_Q = \alpha_Q/T^2$, the Schottky term due to Kramers splitting, and the phonon contribution determined by the zero–field experiments (see previous section). The Zeeman contribution which exists in applied magnetic field at low temperature, $T \leq 0.1$ K, $C_{hf} = \alpha(B)/T^2$, with $\alpha(B)$ deduced graphically, was also subtracted. The obtained $\alpha(B)$ values are plotted in the inset of Fig. 5.14 in the form $\alpha(B)$ vs B^2 showing the expected linear behavior.

The results of the specific–heat measurements on Cs_2CoCl_4 in small fields are shown in Fig. 5.13 where the magnetic specific heat versus temperature is depicted in a semilogarithmic plot. In $B = 0.5$ and 1.5 T, the phase transition has only shifted towards higher temperature, namely $T_N = 0.285$ and 0.331 K, respectively. The overall shape of $C_{mag}(T)$ at T_N is not changed in this field range. The transition remains first–order like up to 2 T (inset of Fig. 5.13). The influence of the magnetic field on the broad maximum is very small and its position, T_{max}, shown by an arrow in Fig. 5.13, hardly
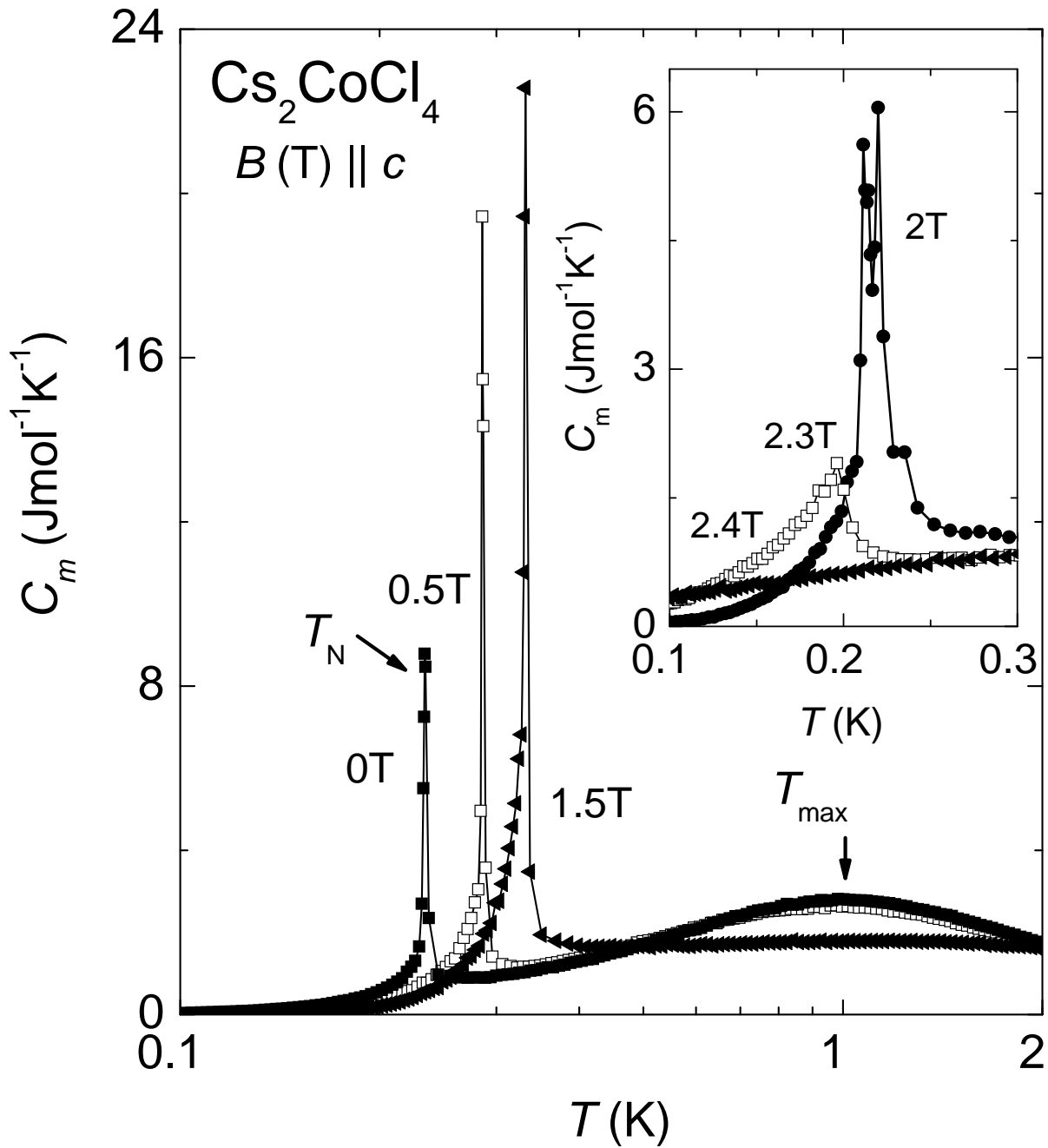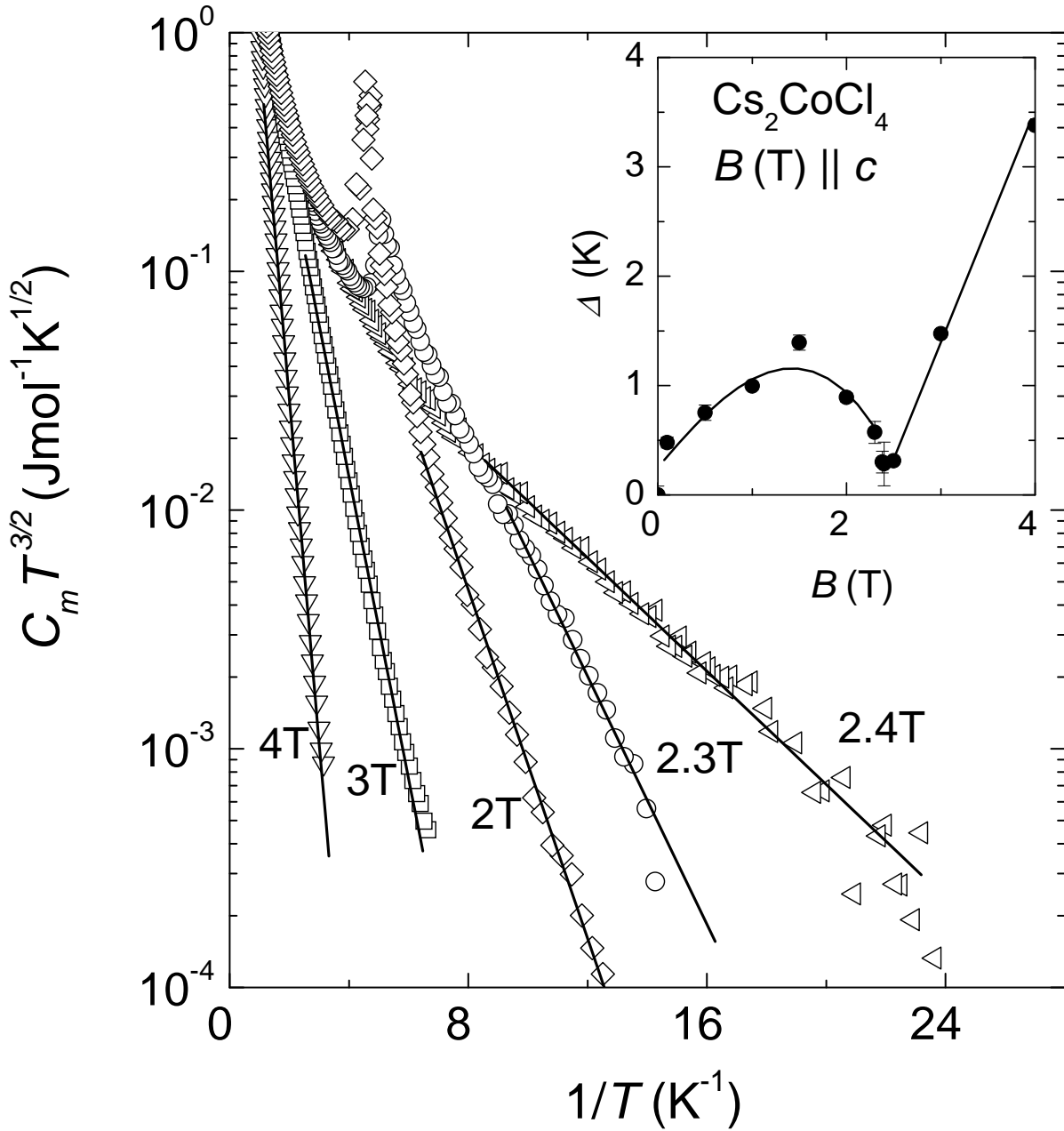
Figure 5.13: *The temperature dependence of the magnetic specific heat, C_m, of Cs_2CoCl_4 in a semilogarithmic plot for $B = 0, 0.5,$ and 1.5 T applied parallel to the c axis. Inset: C_m vs T close to the critical field.*
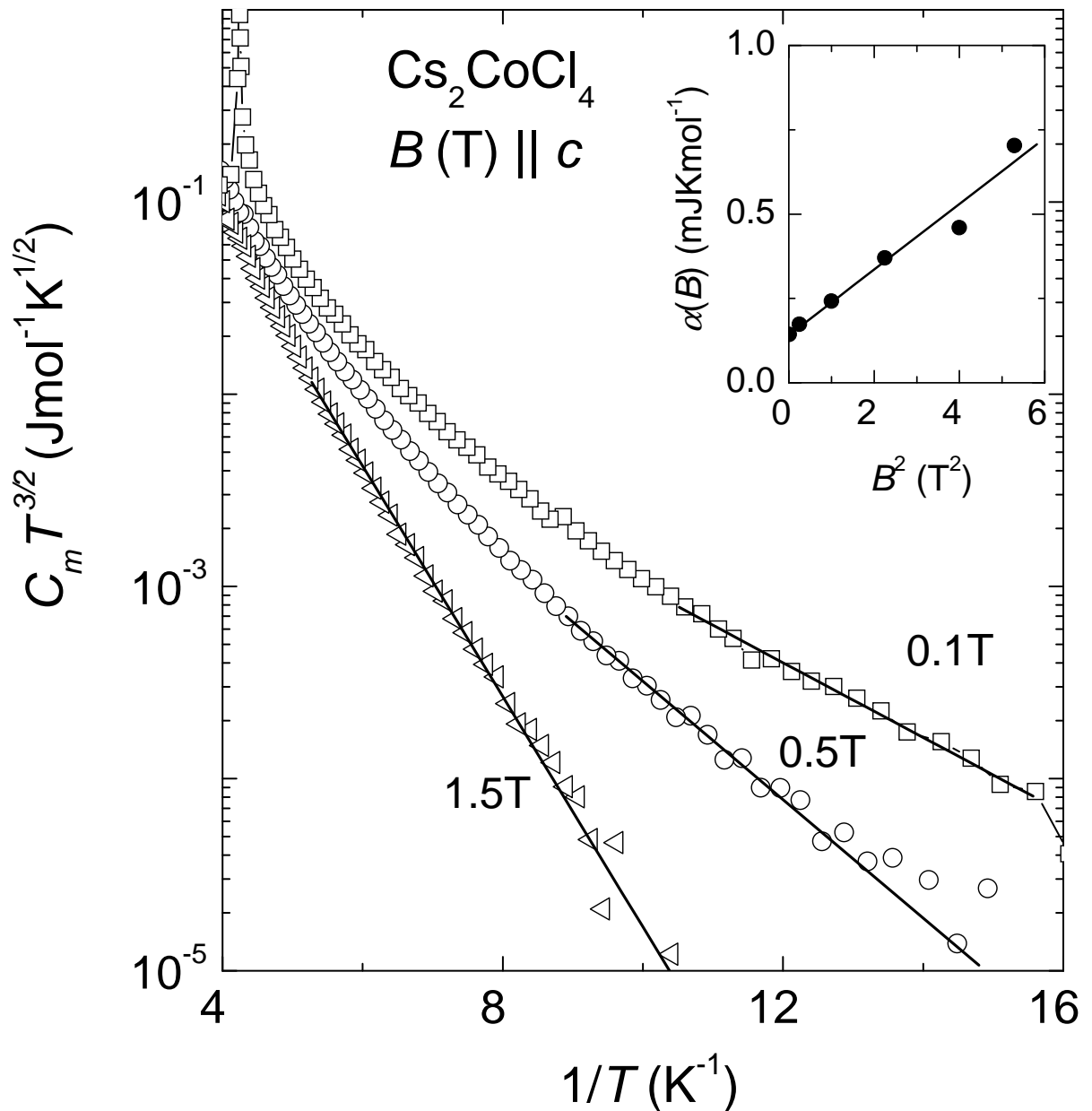
Figure 5.14: $C_m T^{3/2}$ *vs* $1/T$ *of* Cs_2CoCl_4 *for low magnetic fields indicating that the low–temperature data can be described by the XY model (solid lines). The slope of the data yields the field dependence of the gap. Inset:* $\alpha(B)$ *vs* B^2 *determined from the linear fit in a* CT^2 *vs* T^3 *plot in various applied magnetic fields, showing the expected linear behavior.*

Figure 5.15: $C_{mag}T^{3/2}$ *vs* $1/T$ *of* Cs_2CoCl_4 *for higher fields,* $B \geq B_c$. *Comparing the data in* $B = 2$ *and* 2.4 *T, there is a large increase in the slope of the specific heat at low temperatures indicating that the gap decreases. Inset: the field dependence of the gap over the whole phase diagram.*

changes for fields $B < 1.5$ T. However, above this value of the magnetic field, T_{max} is not any longer observed in $C_m(T)$. A clear double–peak structure is seen in $C_m(T)$ for $B = 2$ T as shown in the inset of Fig. 5.13. The peak maxima occurs at $T = 0.211$ and 0.219 K, respectively which hints that there may be two close–by transitions, whereas neutron–scattering measurements [4] showed that the AFM order does not extend beyond 2.15 T. Moreover, with increasing field, for $B = 2.3$ T, the double-peak structure is smeared out and only one peak, much broader than the low–field peak, is visible at $T = 0.196$ K. With further increase of the field no anomaly was observed in specific–heat measurements down to the lowest temperature, $T \simeq 0.06$ K. Thus, for $B > 2.4$ T, the system changes into a high–field paramagnetic state. In fact, neutron–scattering measurements [4] found that the spins become fully aligned along the field direction above 2.5 T. This observations strongly suggest the existence of two critical fields, $B_{c1} \simeq 2$ T at which T_N is suppressed and the double–peak structure appears in $C(T)$, and $B_{c2} \simeq 2.4$ T which marks the beginning of the high–field paramagnetic state separated by a new intermediate phase.

In the following we present the low–temperature specific heat of Cs_2CoCl_4 for $B \parallel a$. Attention has focused on the new intermediate phase suggested already from our specific–heat data in $B \parallel c$. However, it turned out that for this particular direction of the applied magnetic field, the measurement is difficult. This is most likely due to reduced thermal conductivity of the sample for the field $B \parallel a$. Thus, $\kappa_1 \ll \kappa_2$ required for a proper quasiadiabatic measurement (see Chapter 3) is no longer fulfilled for this particular direction. Since to our knowledge there are no thermal–conductivity measurements up to date for this compound, this remains an open question. Under such circumstances it was not possible to perform the measurements in this field direction accurate enough to extract the energy gaps consistently from this set of data.

Fig. 5.16 shows the magnetic specific heat for $B \parallel a$ for several magnetic fields. This plot shows that the data for $B \parallel a$ are most likely similar to those obtained for $B \parallel c$. The AFM transition, indicated by a sharp peak in $C_m(T)$ at $T_N = 0.22$ K for zero field, and its evolution with increasing magnetic field is shown in the inset of Fig. 5.16.

Analogous to $B \parallel c$, at low fields, $B \leq 1.5$ T, T_N increases with increasing field, whereas the broad maximum at T_{max} is almost constant at low fields and disappears at $B = 1.5$ T. At $B = 2$ T a double–peak structure is observed as shown in the main plot of Fig. 5.16, similar to the situation when $B \parallel c$. However the two peaks appear here at slightly higher temperatures $T = 0.214$ and $T = 0.24$ K, respectively. Nevertheless, this second peak can be associated with the transition to the new intermediate phase, discussed above. With further increasing the field, for $B = 2.3$ T a cusp–like anomaly can clearly be seen at $T = 0.193$ K that broadens upon increasing field to $B = 2.35$ T and its position is shifted to lower temperature, $T = 0.159$ K. As the field is increased from $B = 2.35$ to $B = 2.38$ T the transition is suppressed in its height and shifted downwards to $T = 0.128$ K. No further signature of the transition upon approaching further the critical field, $B_{c2} = 2.4$ T, can be resolved from our data.

In conclusion, these measurements confirmed the existence of a new intermediate phase in the region 2 T $\leq B \leq 2.4$ T suggested from the specific–heat measurements along the c axis. Moreover, the phase boundary of the new phase is now well defined. Theoretical arguments show that the transverse field induces a gap in the spin–excitation spectrum [2]. The behavior of the spin gap with the applied magnetic field across the critical point is very important in understanding the mechanism of the transition and for comparison with theory. To extract the field–dependent spin gap we fit our specific–heat data in the low-temperature limit($T < \Delta$) to,

$$C \propto \frac{1}{T^{3/2}} e^{-\Delta/T}, \tag{5.13}$$

predicted for the XY model (see Sec. 2.2).

As shown in Fig. 5.14 and Fig. 5.15 this behavior fits well the experimental data at low temperatures and allowed the gap to be extracted. The change in slope with field indicates that the activation energy changes upon applying an external magnetic field. In Fig. 5.14 the low–temperature data clearly show the suppression of the specific heat in field, indicating that the field initially pushes the density of states towards higher energies. This is consistent with the field initially increasing the gap of spin fluctuations. Moreover, in this field range, T_N increases slightly with increasing field (see Fig. 5.13).

Figure 5.15 shows the temperature dependence of the magnetic specific heat, for $2 \text{ T} \leq B \leq 4 \text{ T}$ and $T \leq 1 \text{ K}$. By comparison between the data obtained for $B = 2$ and 2.4 T e.g., one important feature is immediately noted: there is a large increase in the specific heat at low temperatures indicating an increase in the low-energy density of states in this field range. This is consistent with the gap decreasing between 2 and 2.4 T and possibly vanishing near the critical field, $B_{c2} \simeq 2.4$ T. Above B_{c2}, in the high–field paramagnetic state, the specific heat is largely suppressed for $B = 3$ and 4 T (Fig. 5.15). This is because of the large gap which appears above B_{c2} and increases linearly with increasing field. The field dependence of the gap determined from the fits is shown in the inset of Fig. 5.15.

5.3.4 Commuting field $\vec{B} \parallel \vec{b}$

At zero field the spin–ordering direction is along b. Therefore, at some field spins will flop to be perpendicular to the field and, as a consequence, more transitions are expected with increasing field. Nevertheless, the final transition at high fields, is expected to be in the same universality class as in the other directions, corresponding to the case when the perpendicular order vanishes.

Figure 5.17 shows the magnetic specific heat of Cs_2CoCl_4 for small fields, $B = 0, 0.2$, and 0.5 T, in the temperature region $T \leq 1$ K. The sharp peak at $T_N \simeq 0.22$ K in zero field indicating a phase transition to a magnetically ordered phase is shifted to lower temperature for $B = 0.2$ T. Furthermore, for this field, a second peak appears at $T \simeq 0.134$ K indicating a transition to a new type of ordered phase. However, the height of the peak which appears at lower temperature, is much smaller than the peak observed above it. For $B = 0.5$ T (see inset of Fig. 5.17) two sharp maxima are observed associated with phase transitions at slightly higher temperatures $T = 0.148$ and 0.199 K respectively. This applied magnetic field results also in a change of the ratio of the heights of the two peaks; they become comparable.

As shown in Fig. 5.18, with increasing the magnitude of the field, for $B = 1$ T the peak positions shift to higher temperatures. Surprisingly, the lower peak at $T = 0.174$ K, is
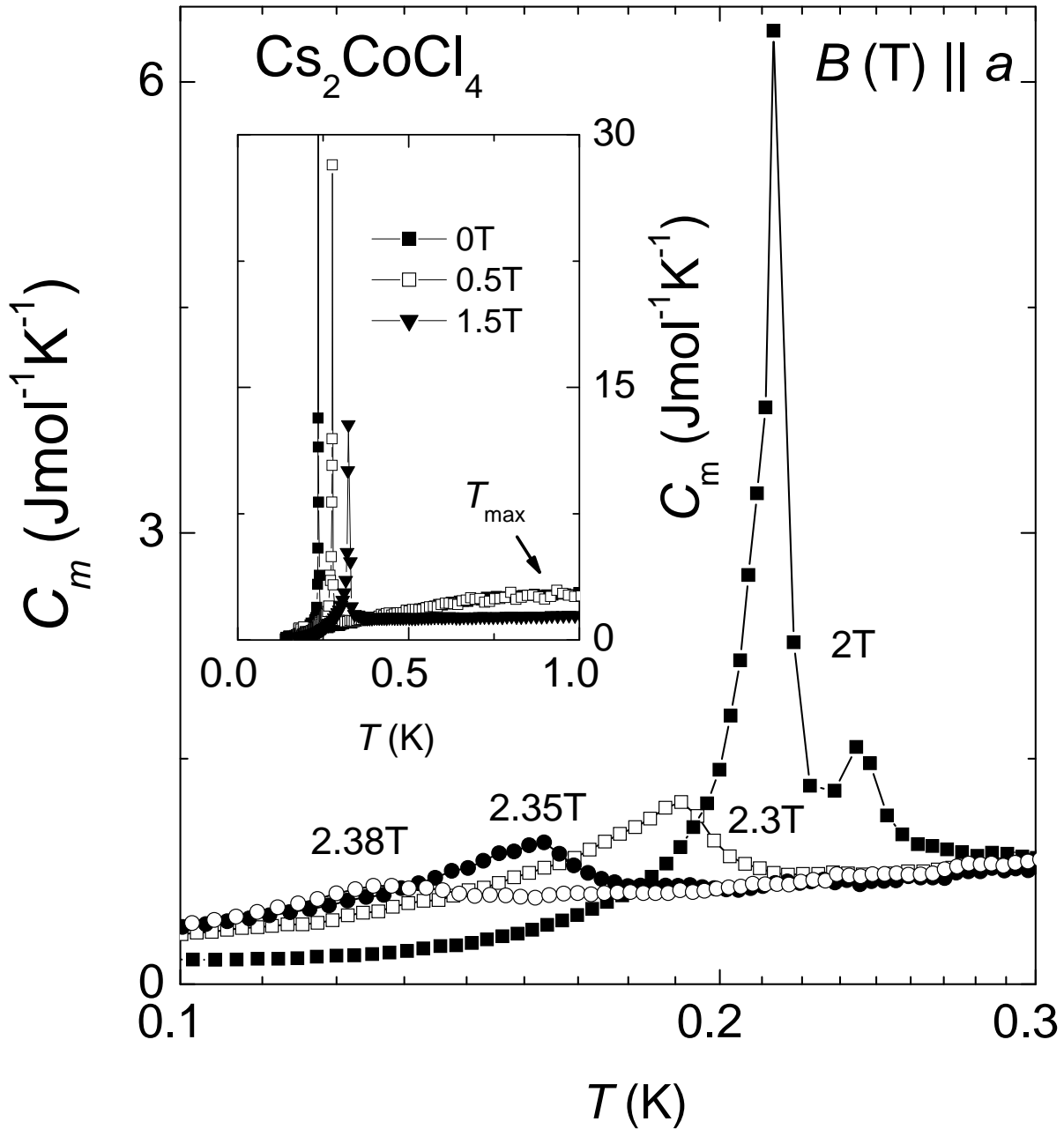
Figure 5.16: C_m *vs* T *of* Cs_2CoCl_4 *in a semilogarithmic plot for fields along* a, *close to the critical field. A new feature appears at* $B = 2$ *T. The* $B = 2.38$ *T data reveal a small cusp–like anomaly at* $T = 0.128$ *K indicating the vicinity of the critical field,* $B \simeq 2.4$ *T. Inset:* C_m *vs* T *in a semilogarithmic plot for* $B = 0, 0.5,$ *and* 1.5 *T applied parallel to the* a *axis.*
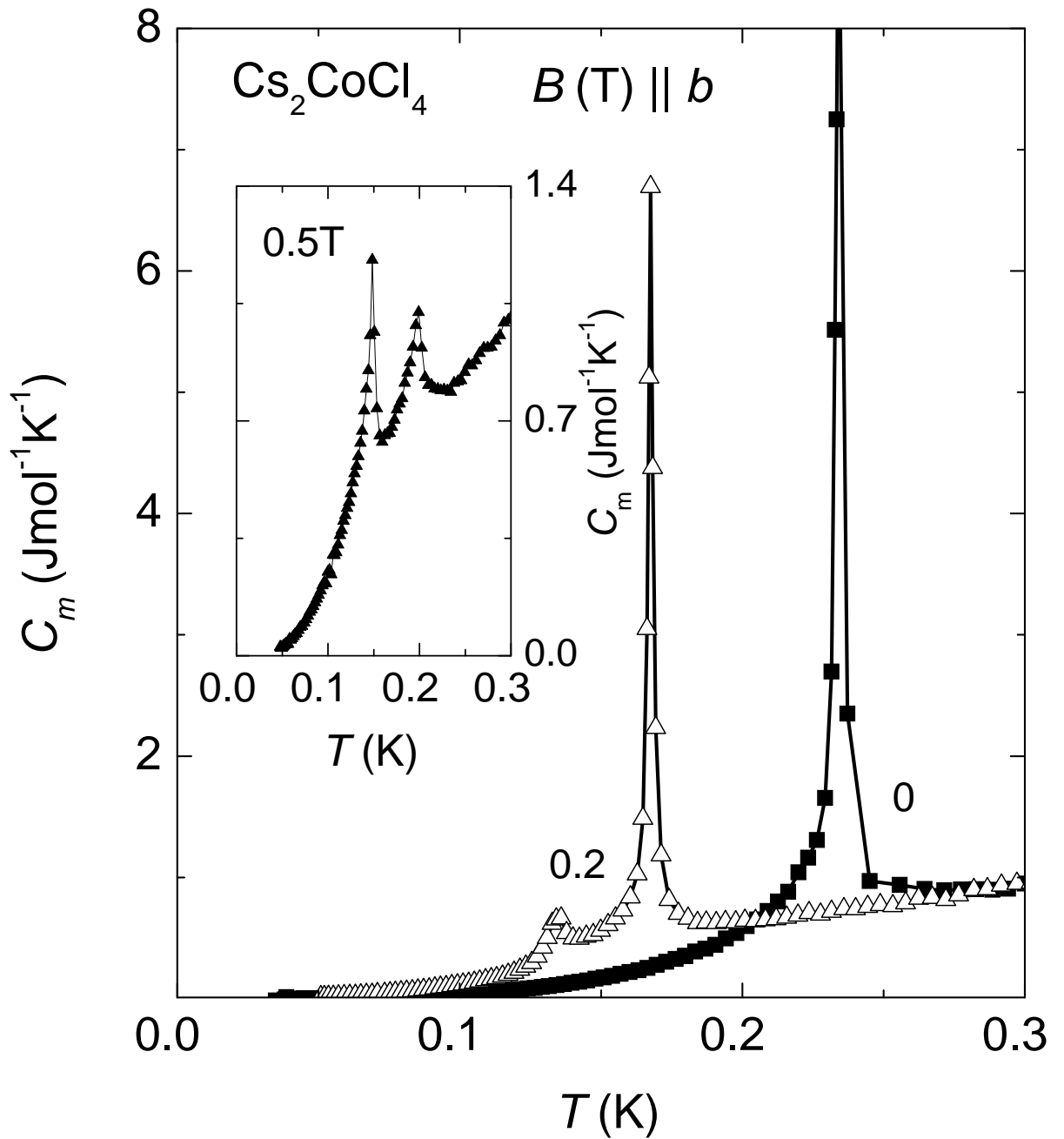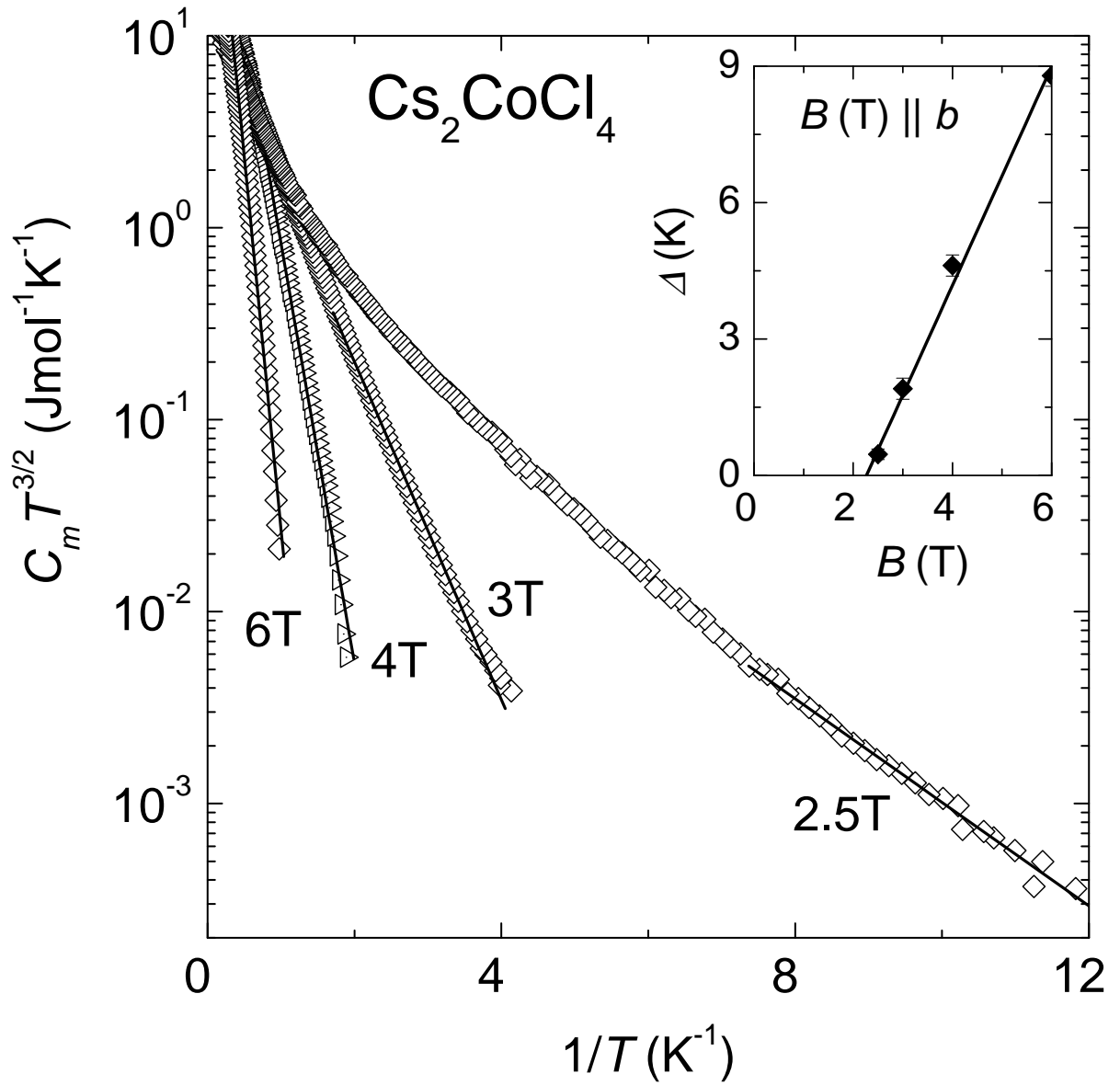
Figure 5.17: *Magnetic specific heat versus temperature of Cs_2CoCl_4 for $B = 0$ and $B = 0.2$ T applied parallel to the b axis. Inset: $B = 0.5$ T data for $T \leq 0.3$ T.*
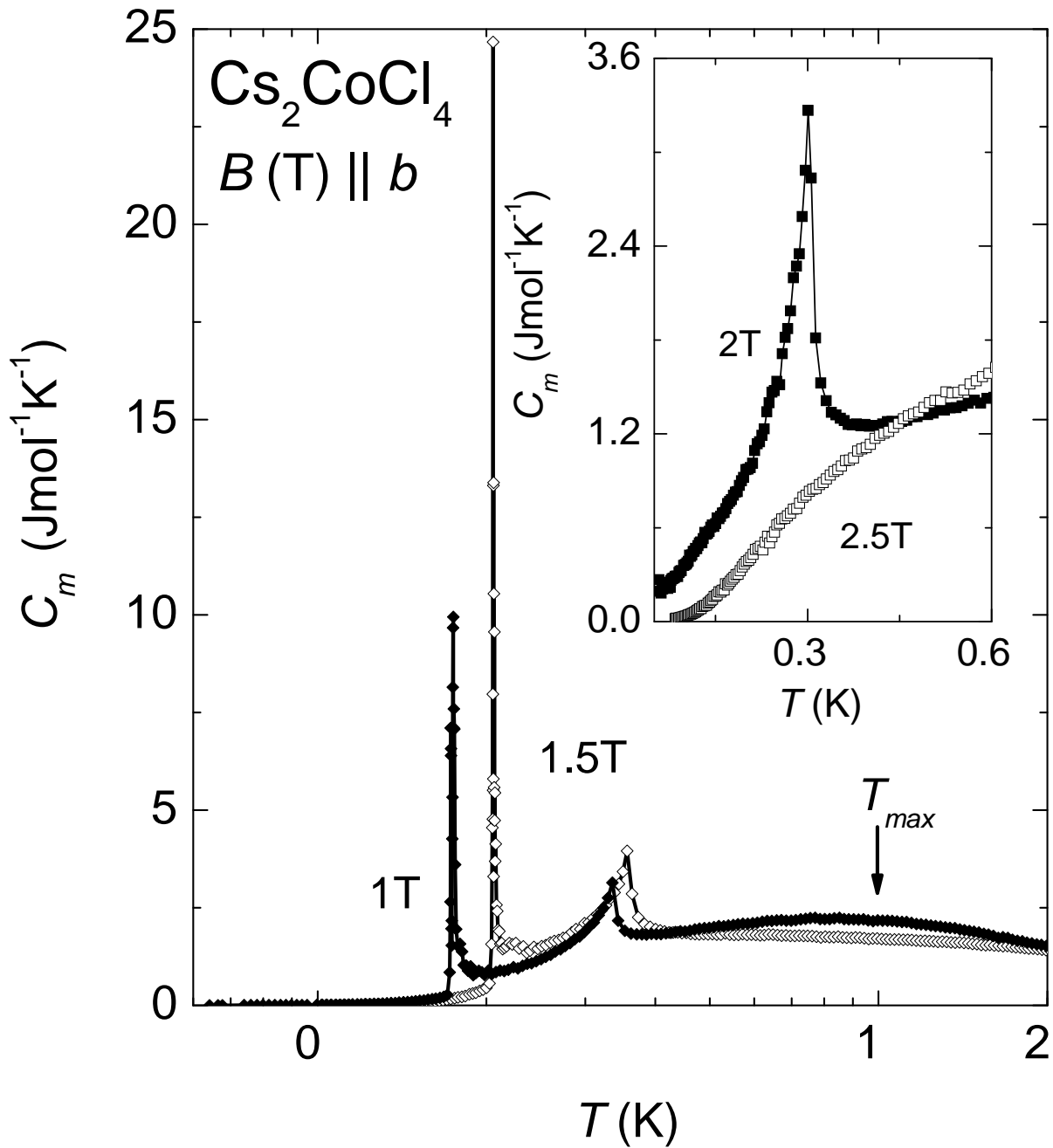
Figure 5.18: *Magnetic specific heat of Cs_2CoCl_4 versus temperature close to the anti-ferromagnetic phase transition in magnetic fields $B = 1$ and 1.5 T applied parallel to the b axis. Inset: $B = 2$ and 2.5 T data.*

Figure 5.19: $C_{mag}T^{3/2}$ *vs* $1/T$ *of* Cs_2CoCl_4 *for higher fields,* $B \geq B_c$. *Inset: the excitation gap* Δ *versus magnetic field.*

very sharp as compared to the upper one at $T = 0.335$ K. Both transitions are shifted to higher temperatures with increasing the magnetic field to $B = 1.5$ T ($T = 0.206$ K and $T = 0.356$ K, respectively). The origin for these peaks will be discussed later. However this double–structure feature is observed for fields up to 2 T. As shown in the inset of Fig. 5.18, for $B = 2$ T only one sharp phase transition is clearly exhibited at a temperature of $T = 0.301$ K. Below the transition, a broad shoulder at $T \simeq 0.130$ K is observed. No signature of other transitions was observed for $B = 2.5$ T. Instead, similar to $B \parallel c$ and $B \parallel a$ the specific heat is strongly suppressed because of the field–induced gap in the spin–excitation spectrum. In the following we examine the low–temperature limit of the specific–heat which is sensitive to low–energy properties of the spin system. Fitting the low–temperature region by eq. (5.13) (see also Sec. 2.2) we can obtain the evolution of the excitation gap with applied magnetic field.

Figure 5.19 shows $C_m T^{3/2}$ vs $1/T$ in a semilogarithmic plot above the critical field up to 6 T. The gap versus field, determined from fitting the low–temperature part is shown in the inset of Fig. 5.19. The data in the inset are fitted by the line shown which extrapolates to $\Delta = 0$ at $B \simeq 2.26$ T. Thus from this fit we have estimated the critical field, $B_c \simeq 2.26$ T.

5.3.5 Discussion

Our specific–heat measurements in zero magnetic field confirmed the earlier reported results [4, 129, 130]. In zero magnetic field the system can be described by the XY model for which the specific heat was also calculated analytically. This gives a perfect fit of the data and similar proportions for each contribution type as in previous papers [129, 130]. The values for J and the Kramers splitting ($J/k_B = 3.09(1)$ K ($J = 0.267$ meV) and $D/k_B \simeq 15$ K (~ 1.3 meV), respectively) are also consistent with neutron–scattering experiments [4]. The value $J = 0.267$ meV in this fit is slightly larger than the XXZ predicted $J = 0.23$ meV as an XY model is used here for the description of the specific heat [131]. But this slight effect is also expected and was discussed already in Ref. [130].

We also measured the thermal excitations of the system in nonzero fields and at very

low temperatures. In this limit it can be mapped on to an anisotropic spin model, namely to the XXZ model with the anisotropy parameter Δ' assumed to be $-1 < \Delta' < 1$ (XY universality class) [4].

Theoretical studies [132] found that a noncommuting field breaks the U(1) symmetry of the model to a lower Ising–like symmetry which brings the ground state to long–range order at $T = 0$ into a spin–flop Néel state. In fact, at a special coupling, $B = \sqrt{2}J/\mu_B$ corresponding to $B = 1.7(1)$ T, the spin–flop Néel state is the exact $T = 0$ ground state. Another important observation was that a noncommuting field induces quantum fluctuations into the system and at high fields this causes a disordered spin-liquid phase to occur below the saturated phase. This phase transition is therefore a nontrivial quantum phase transition through a quantum critical point with the noncommuting field as a control parameter. Above a crossover field of about $2J$ corresponding to 3.3(1) T nearly all the spin moments are aligned along the field direction and the physics here is characterized as a saturated phase. Theoretical arguments show that spin–liquid phases such as this are generally gapped (evidenced by the exponentially decaying correlations in the zero–temperature ground state) and therefore robust against small perturbations. Thus it is expected that the effect of a nonzero anisotropy parameter and interchain coupling does not change the qualitative features of the predicted phase diagram. In the following, we look for these features in the phase diagram (T, B) based on our specific–heat data in a noncommuting field.

In noncommuting fields the applied field opens a gap in the excitation spectrum, and stabilizes perpendicular antiferromagnetic order (spin-flop phase). The gap initially increases with field, then decreases and closes at a critical field B_c where the perpendicular antiferromagnetic order disappears. For fields higher than B_c, the gap increases again with increasing field. For a quasi–1D system which has a finite T_N this would predict an increase of T_N with increasing field, then a suppression of T_N to 0 at a critical field B_c above which no long-range order exists [4, 132, 133]. Analyzing our specific–heat data looking for these trends, we observed indeed that our results are entirely resembling the

theoretical predictions.

The T, B phase diagram presented in Fig. 5.20 summarizes the data obtained from the specific–heat measurements on Cs_2CoCl_4 in applied noncommuting fields. A spin–flop phase at low temperatures below T_N and $B \leq B_{c1}$ with $B_{c1} = 2$ T is established. Magnetic fields initially stabilize the AFM order by supressing fluctuations. This is directly observed in the increase in T_N with magnetic field. For $B = 2$ T, a second sharp peak appears at $T = 0.211$ K which hints that there may be a second close–by transition. However, for $B = 2.3$ T a cusplike anomaly develops at $T \simeq 0.196$ K and then vanishes with increasing field. For $B = 2.4$ T, our specific–heat measurements show no anomaly down to the lowest temperature, $T \simeq 0.06$ K. Nevertheless, fields along a and c are similar in that the spin–ordering direction in zero field (along b) is perpendicular to the applied field, so that with increasing field the spins cant along the field direction up to the critical field where fluctuations suppress the perpendicular order. Therefore, we completely defined the intermediate phase (T, B) using both sets of data in noncommuting field. Above $B_{c2} = 2.4$ T the high–field paramagnetic state is entered. This state is not a fully–polarized state because the magnetization is not saturated above B_c [4] and in fact theoretically a saturation of the magnetization is not expected as shown in Ref. [132].

Figure. 5.20 shows also, a direct comparison between the phase diagram based on our $C_{mag}(T)$ data, and the phase diagram of weakly coupled XXZ chains in a transverse magnetic field (solid line) obtained by using the mean–field approximation for the inter-chain coupling and known exact results for an effective one–dimensional model [133]. In comparison to the theoretical phase diagram, our measurements indicate that there is another ordered phase in the intermediate region 2.1 T $\leq$ B $\leq$ 2.4 T. We observed a peak in the specific heat even at 2.3, 2.35 and 2.38 T, although much broader than the low–field peaks and the natural explanation is a transition to an ordered phase, whereas the neutron–scattering measurements showed that the antiferromagnetic order does not extend beyond $B_{c1} = 2.15$ T. This new phase appears near the region where the gap in the excitation spectrum of the spin flop state is vanishing. It separates the high field

paramagnetic state and the spin–flop state.

However, near the critical field B_{c1} many states become close in energy, so in fact it is not surprising that other phases may occur. In the absence of any perturbation we believe the transition is in the same universality class as that of an Ising chain in transverse field [2], i.e., close to the critical field only fluctuations perpendicular to the field are important and in fact it is an Ising symmetry that is broken spontaneously upon entering the ordered phase from high fields, $B > B_{c2}$, with $B_{c2} \simeq 2.4$ T. As the chains in Cs_2CoCl_4 form a zig-zag arrangement, one possibility for this new phase is an incommensurate–order phase, such as a spin–density–wave state (moments perpendicular to the field) stabilized by the frustrated interchain couplings [122, 134]. Starting from high fields there is the gapped quantum paramagnetic phase. The gap closes at B_{c2} at an incommensurate wavevector, $Q(B_{c2})$, then lowering the field between B_{c2} and B_{c1} the system is gapless and the incommensuration varies continuously with field. At B_{c1}, the ordering wavevector locks into a commensurate value $Q(B_{c1}) = Q_{AF}$, which corresponds to antiferromagnetic order along the chains. Thus, below B_{c1} the order is commensurate and the gap opens. Therefore, the intermediate phase, $B_{c1} \leq B \leq B_{c2}$ is a spin–density–wave phase, which is gapless with power–law spin correlations. The width in field, $B_{c2} - B_{c1}$, depends on the frustration J'/J, i.e., is zero if $J' = 0$. To confirm this, more specific–heat measurements are needed in this field region and also magnetization measurements versus field at mK temperatures to look for small anomalies near the critical fields.

In the longitudinal field theoretical arguments [133] show that the spectrum remains gapless if the field does not exceed the saturated value $B_c = J(1 + \Delta')/g\mu_B$. Using the proposed values for the exchange interactions in Cs_2CoCl_4, $J = 0.23(1)$ meV, $\Delta' = 0.25$, and $g = 2.4$ [4], the longitudinal critical field is estimated as $B_c = 2.2(1)$ T. We have extracted the critical field from the linear fit of $\Delta(B)$ and obtained $B_c \simeq 2.26$ T, which is in very good agreement with the predicted value.

Our specific–heat data on Cs_2CoCl_4 for fields $B \parallel b$ established that for this particular direction the compound has a very rich phase diagram (see Fig. 5.21). In the high–
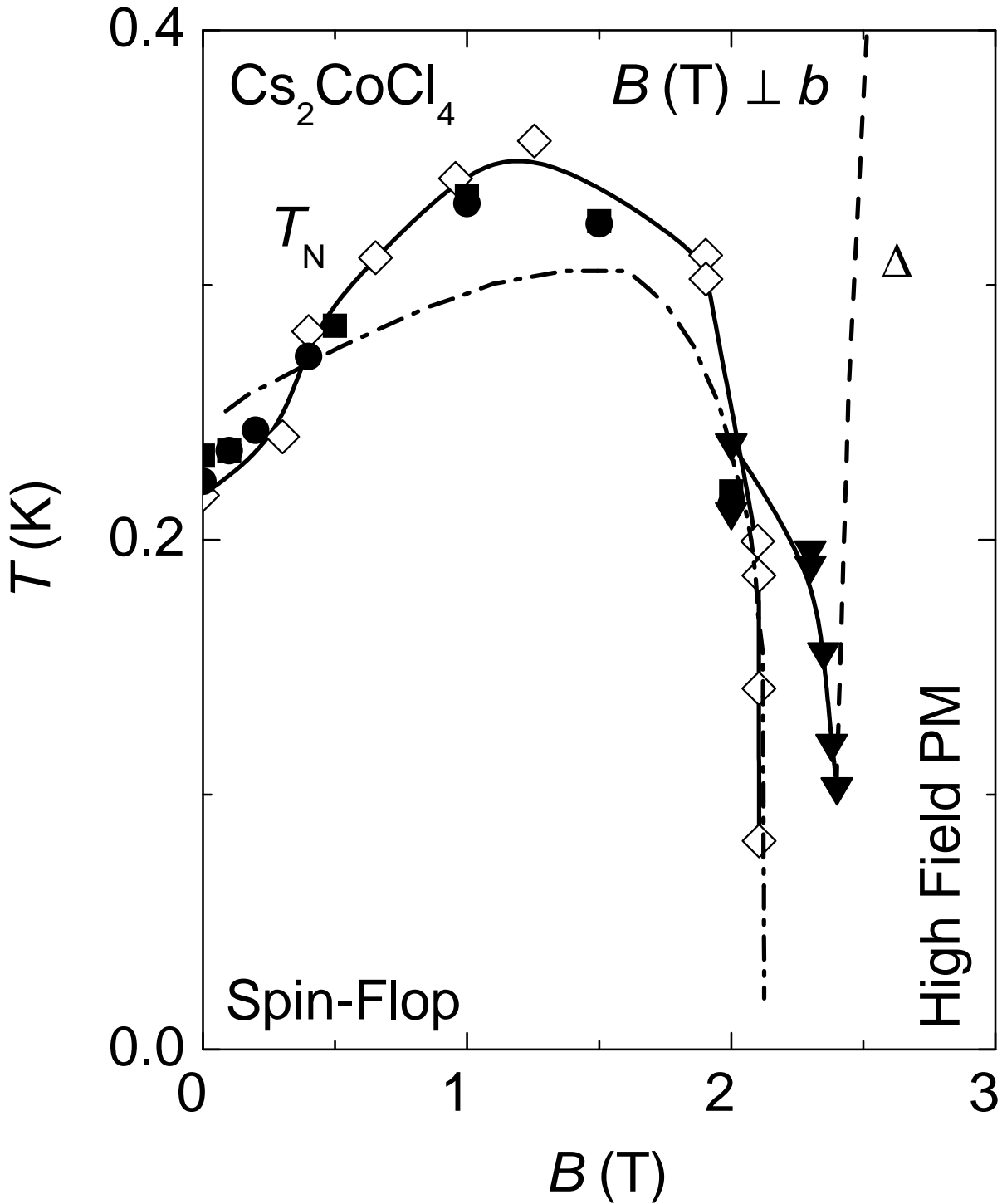
Figure 5.20: *T, B phase diagram for Cs_2CoCl_4 in noncommuting fields ($B \perp b$). Filled symbols show the position of the anomalies found in the specific–heat measurements for $B \parallel c$ and $B \parallel a$. Open diamonds denote the phase boundary of the long–range order obtained by using neutron scattering [4, 122]. The dashed–dotted line shows the expected phase diagram [133] of weakly coupled XXZ chains in a transverse magnetic field. The solid lines denote the experimentally observed phase boundary lines. The dashed line represents the evolution of the gap, Δ, with magnetic field.*
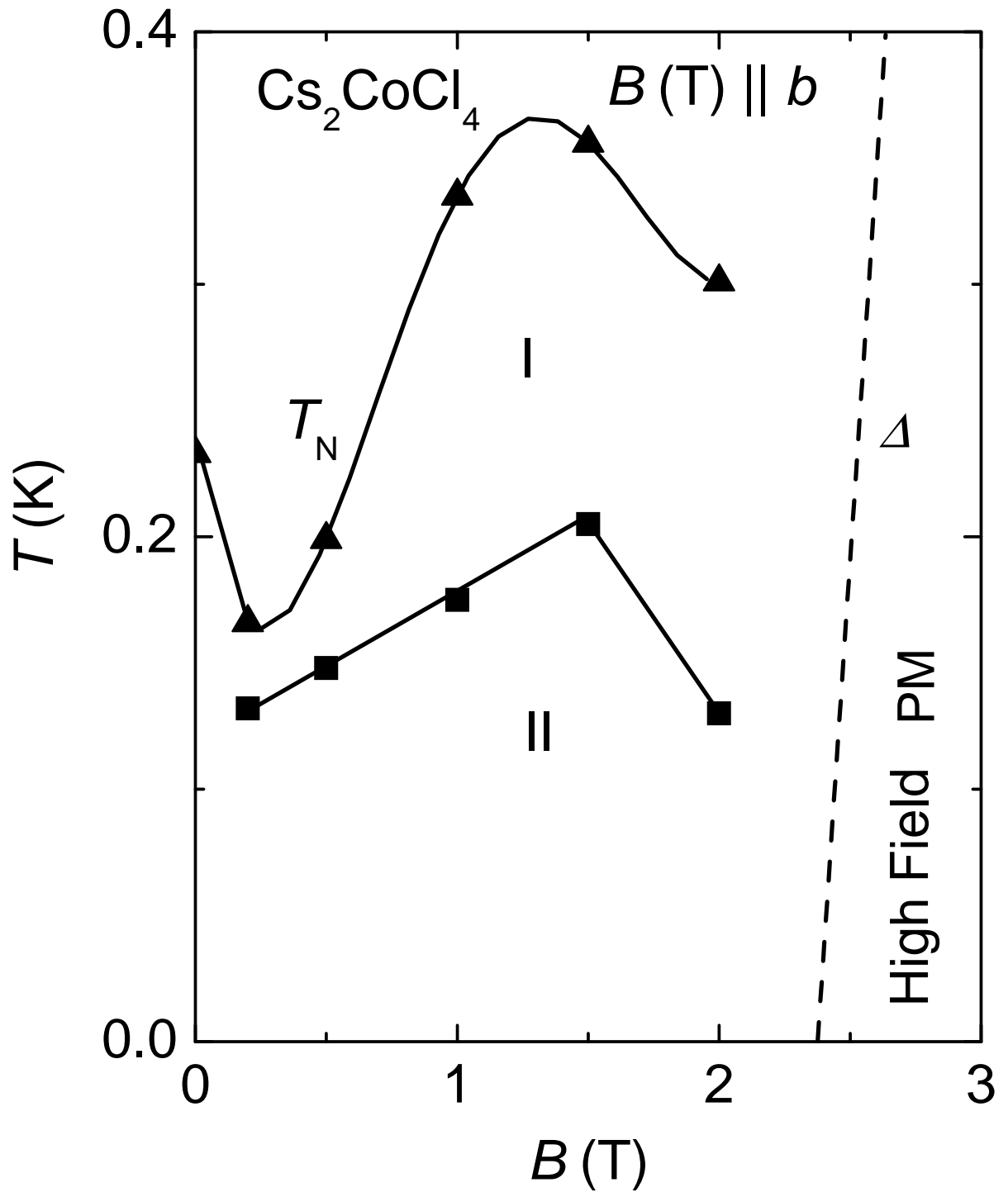
Figure 5.21: *(T, B) phase diagram of Cs_2CoCl_4 for $B \parallel b$ (commuting field). In small magnetic fields, $B \geq 0.2$ T, two phases appear denoted by I and II. Above $B_c \simeq 2.26$ T, the system enters the high–field paramagnetic phase. The gap, Δ as a function of magnetic field is shown by dashed line.*

temperature and low–field region of the phase diagram, similar to $B \perp b$, there is a crossover from a paramagnetic state to a state with short–range spin–spin correlations ($T_N < T < T_{max}$). The broad maximum at $T_{max} \simeq 1$ K in zero magnetic field is still clearly visible for fields up to 1.5 T. However, at lower temperatures small magnetic fields of $B \simeq 0.2$ T induce already new ordered phases, denoted by I and II in Fig. 5.21 and indicated by the sharp peaks in the specific heat. We believe that this is due to a change of the relative orientation between the chains. Thus, our measurements highlight a potentially very significant phase diagram in Cs$_2$CoCl$_4$ in longitudinal fields. Further studies using NMR, magnetic susceptibility, and neutron–scattering measurements are called in order to investigate the nature of these magnetic phases.

6 Conclusions

In this work a versatile calorimeter for measuring heat capacities ($C_{min} \approx 1 \mu J/K$ at 0.1 K) of small solid samples, $m < 0.05$ g at low temperatures (0.03 K$\leq T \leq 6$ K) and in high magnetic fields ($B < 12$ T) was developed. It is based on the quasiadiabatic heat–pulse method which makes possible a rapid data acquisition, much faster than a relaxation–time technique. The other advantage is that three different samples can be mounted on three platforms of the sample holder and one sample is measured while the other may cool down. Our results show that the heat capacity can be determined with high precision in a fast and accurate way.

We have experimentally investigated the low–temperature properties of two classes of materials with a special emphasizes near the QCP induced by substitution and magnetic field: (1) the HF systems $YbRh_2(Si_{0.95}Ge_{0.05})_2$, $Yb_{1-y}La_yRh_2Si_2$ ($y = 0.05, 0.1$), and $YbIr_2Si_2$ with tetragonal structures and $CeIn_{3-x}Sn_x$ ($0.55 \leq x \leq 0.8$) with cubic structure; (2) the quantum spin systems: Cs_2CuCl_4 and Cs_2CoCl_4.

In all the HF compounds we have observed NFL behavior in zero magnetic field close to the QCP. The La–substituted system does not show an antiferromagnetic (AFM) transition down to the lowest accessible temperature (0.03 K) while in $YbRh_2(Si_{1-x}Ge_x)_2$ with $x = 0$ and $x = 0.05$ AFM transitions occur at $T_N \simeq 0.07$ K and 0.02 K, respectively. Moreover, $Yb_{0.95}La_{0.05}Rh_2Si_2$ already shows a tendency to saturation in $\Delta C(T)/T$ below 0.04 K at a Sommerfeld coefficient $\gamma \simeq 1.35$ JK^{-2}mol^{-1}, one of the highest values among magnetically non–ordered Yb–systems. This is suggestive of a LFL ground state in this compound. For $Yb_{0.9}La_{0.1}Rh_2Si_2$ we observe below 0.07 K saturation of $\Delta C/T$

indicating clearly a LFL state for this concentration. For $YbIr_2Si_2$, $\Delta C(T)/T$ saturates below ~ 0.5 K to a value of $\gamma = 0.372$ $JK^{-2}mol^{-1}$. Thus, $Yb_{1-y}La_yRh_2Si_2$ ($y = 0.05, 0.1$) and $YbIr_2Si_2$ are found to be placed on the non-magnetic site of the QCP, in contrast to $YbRh_2(Si_{1-x}Ge_x)_2$ ($x = 0, 0.05$) which are just on the magnetic side.

However, no $C(b, T)$ scaling behaviour, ($b = B - B_c$) was found. The NFL effects observed in $CeIn_{3-x}Sn_x$ in zero field in the vicinity of $x_c \simeq 0.7$ cannot be described by the existent theories for 3D SDW. This experimental observation, which agrees with resistivitiy measurements [103], stresses the need of further theoretical development that would explain not only the linear temperature dependence of the resistivity but also the observed logarithmic dependence of the specific heat. In the presence of magnetic fields we observed field–induced LFL behavior in all the systems. However, in contrast to the Yb–based compounds in the vicinity of the QCP, $CeIn_{3-x}Sn_x$ shows no evidence of a divergence in γ, with B or with x.

Furthermore, we used specific–heat measurements in the mK temperature range and at high fields (up to 12 T) to probe the phase diagrams in the low–dimensional quantum antiferromagnets Cs_2CuCl_4 and Cs_2CoCl_4.

For zero–field measurements our results for the insulating magnet Cs_2CuCl_4 above the ordering temperature T_N are well described within the spin–1/2 AFM isotropic Heisen-berg chain model [121]. This indicates that the coupling between chains is thermally broken and 1D short–range AFM spin correlations are effective for $T > T_N$. From the comparison with the 2D anisotropic triangular–lattice model at $J'/J = 1/3$ one can conclude that the 1D model is more appropriate for our specific–heat data. However, this conclusion is not completely decisive because DM anisotropy was not included in the theoretical calculations. Again, further theoretical work is needed in order to clarify this issue.

In applied magnetic field, we have presented experimental evidence that in Cs_2CuCl_4 the field dependence of the critical temperature $T_c(B) \propto (B_c - B)^{1/\phi}$ close to the critical field $B_c = 8.51$ T is well described with $\phi \simeq 1.5$. This is in very good agreement with the exponent expected in the mean-field approximation. Together with the observed

opening of a spin gap above B_c these findings support the notion of a Bose-Einstein condensation of magnons in Cs_2CuCl_4. Furthermore, for other field orientations with respect to the crystallographic axes we found evidences of new magnetic phases which occur for intermediate fields 2 T $< B < 8$ T between the spiral AFM state, $B \leq 2.1$ T and the fully spin–polarized state, $B > 8$ T. This is the motivation for future thorough neutron–scattering measurements to map the whole Brillouin zone in order to characterize the magnetic structure of these new phases.

Finally, we studied the low–temperature thermodynamics of the quasi-one-dimensional spin-1/2 XY-like AFM Cs_2CoCl_4 in magnetic field. We presented (T, B) phase diagrams for noncommuting and commuting fields. In noncommuting fields, our results show a new phase transition in the intermediate region 2.1 T $\leq B \leq 2.4$ T, separating the spin–flop state and the high–field paramagnetic state whereas the neutron–scattering measurements showed that the antiferromagnetic order does not extend beyond $B_{c1} = 2.15$ T. The nature of this phase is still unclear and needs some further experimental and theoretical investigations. In commuting field a rich phase diagram was obtained which opens new perspectives for theoretical studies.

In summary, we have obtained specific–heat results that bring new insight into the thermodynamical properties of HF and low–dimensional spin systems near the QCP. The comparison of our data with other experimental results shows that we were able to reproduce and improve their quality. Exploring different compounds, e.g., HF metals and magnetic insulators, besides the agreement with current theories, many of our results point out new directions for further theoretical studies.

7 Overview of the analyzed samples

Compound	Sample-Nr.	$mass$ mg	Mounting
$YbRh_2Si_2$	37085d	7.22	$B \perp c$
$YbRh_2(Si_{0.95}Ge_{0.05})_2$	48002e	21.03	$B \perp c$
$Yb_{0.95}La_{0.05}Rh_2Si_2$	55053c	3.4	$B \perp c$
$Yb_{0.9}La_{0.1}Rh_2Si_2$	55057c	6.79	$B \perp c$
$YbIr_2Si_2$	47198	15.4	$B \parallel c$
$CeIn_{2.5}Sn_{0.55}$	42237	13.79	$B \parallel a$
$CeIn_{2.4}Sn_{0.6}$		17.46	$B \parallel a$
$CeIn_{2.35}Sn_{0.65a}$	42171	28.76	$B \parallel a$
$CeIn_{2.35}Sn_{0.65b}$	42280	62.90	$B \parallel a$
$CeIn_{2.3}Sn_{0.7a}$	42263	4.51	$B \parallel a$
$CeIn_{2.3}Sn_{0.7b}$	42263	30.47	$B \parallel a$
$CeIn_2Sn_{0.8}$	42260	11.08	$B \parallel a$
Cs_2CuCl_4		28.40, 52.03	$B \parallel a$
		28.40, 52.03	$B \parallel b$
		52.03	$B \parallel c$
Cs_2CoCl_4		28.05, 17.90, 35.65	$B \parallel a$
		17.90	$B \parallel b$
		35.65, 28.05	$B \parallel c$

Table 7.1: Overview of the single–crystalline samples investigated.

Acknowledgement

debted to Professor Julián G. Sereni, the external examiner of my dissertation for his thorough reading of the thesis and valuable suggestions for its improvement. I am grateful to Professor Joachim Wosnitza for useful discussions of experimental data of low dimensional systems.

The members of the crystal–growth group Julia Ferstl, Nubia Caroca–Canales, and Dr. Zakir Hossain have been invaluable in providing excellent samples.

Particulary, I wish to thank Dr. Thomas Lühmann for his help and strenuous support, for his advice on many different technical problems during my research. From him I learned a lot about low temperature calorimeters.

From the beginning of my graduate studies, Miclea Corneliu, Dr. Yoshifumi Tokiwa, and Edith Lengyel have been the most supportive colleagues, from those experience I have greatly benefited. Dr. Yoshifumi Tokiwa have read parts of my thesis and provided me valuable comments. The working environment at MPI has been made enjoyable by the many colleagues and friends Gabriel Dionicio, Adriana Sanchez, Jeevan Hirale, Franziska Weickert, Rober Küchler, Tanja Westerkamp, Jan Wykhoff, Ulrike Schmidt, Cornelius Krellner, Dr. Ivica Zerec, Dr. Micha Deppe, Dr. Niels Oeschler, Dr. Tomasz Cichorek . Their help on various occasions is gratefully acknowledged. Special thanks go to Ivan Liu, Ionutz Georgescu, Dr. Izabella Benczik, Dr. George Kalosakas and Dr. Doru Bodea, from the neighboring institute (MPI PKS) for valuable discussions and suggestions related to the work presented in this thesis. In addition, Dr. Michael Nicklas and Dr. Nakanishi Takeshi have been both good colleagues and reliable basketball players.

Finally, my deepest gratitude goes to my husband and my parents who have given me everything.

Author's declaration

I declare that the work described in this dissertation was carried out in accordance with the regulations of the Technology University of Dresden. No part of this work has been submitted previously for a degree or other qualification at this or any other university. The research reported herein is original, except where specific reference is acknowledged to the work of others. All the research was carried out under the supervision of Prof. Frank Steglich and Dr. Heribert Wilhelm in Max-Planck-Institute for Chemical Physics of Solids between September 2001 and Juni 2005.

Maria Teodora Radu

Dresden, Germany

8th June 2005

Versicherung

Hiermit versichere ich, dass ich die vorliegende Arbeit ohne unzulässige Hilfe Dritter und ohne Benutzung anderer als der angegebenen Hilfsmittel angefertigt habe; die aus fremden direkt oder indirekt übernommenen Gedanken sind als solche kenntlich gemacht. Die Arbeit wurde bisher weder im Inland noch im Ausland in gleicher oder ähnlicher Form einer anderen Prüfungsbehörde vorgelegt.

Die vorliegende Dissertation wurde am Max-Planck-Institut für Chemische Physik fester Stoffe in Dresden unter der wissenschaftlichen Betreuung von Herrn Prof. Dr. Frank Steglich und Dr. Heribert Wilhelm angefertigt.

Ich erkenne die Promotionsordnung an.

Bibliography

[1] C.N. Yang and C.P. Yang. *Phys. Rev. B*, **150**:321–327, 1966.

[2] S. Sachdev. *Quantum phase transitions*. Cambridge University Press, Cambridge, UK, 1999.

[3] D. Bitko, T.F. Rosenbaum, and G. Aeppli. *Phys. Rev. Lett.*, **77**:940–943, 1996.

[4] M. Kenzelmann, R. Coldea, T.A. Tenannt, D. Visser, M. Hofmann, P. Smeibidl, and Z. Tylczynski. *Phys. Rev. B*, **65**:144432–1–14, 2002.

[5] T. Matsubara and H. Matsuda. *Prog. Theor. Phys.*, **16**:569, 1956.

[6] E. Batyev and L. Braginskii. *Sov. Phys. JETP*, **60**:781, 1984.

[7] S. Gluzman. *Phys. Rev. B.*, **50**:6264, 1994.

[8] T. Nikuni, M. Oshikawa, A. Oosawa, and H. Tanaka. *Phys. Rev. Lett.*, **84**:5868, 2000.

[9] M. Matsumoto, B. Normand, T.M. Rice, and M. Sigrist. *Phys. Rev. Lett*, **89**:077203, 2002.

[10] G. Misguich and M. Oshikawa. *cond.–mat/0405422*, 2004.

[11] E.S.R Gopal. *Specific heat at low temperatures*. Plenum, New York, 1966.

[12] C. Kittel. *Quantum theory of solids*. John wiley & Sons, Inc., 1987.

[13] B. Bleaney. *Magnetic properties of Rare Earth Metals*. Plenum Publishing Company Ltd., London, 1972.

[14] B. Bleaney. *Handbook on the Physics and Chemistry of RE*. K.A. Gschneidner Jr. and L. Eyring, North–Holand, 1977. Chapter 77.

[15] Frank Pobell. *Matter and Methods at Low Temperatures*. Springer Verlag, 1999.

[16] B. Bernu and G. Misguich. *Phys. Rev. B*, **63**:134409, 2001.

[17] Minoru Takahashi. *Thermodynamics of one–dimensional solvable models.* Cambridge Univ. Press, 1999.

[18] Daniel C. Mattis. *The Theory of Magnetim I.* Springer–Verlag, 1988.

[19] J.S. Caux. Private Communication, 2004.

[20] L.D. Landau. *Sov. Phys JETP*, **3**:920–925, 1956.

[21] G.R. Stewart. *Phys. Rev. Lett.*, **52**:679–685, 1984.

[22] S. Doniach. *Physica B & C*, **91**:231–234, 1977.

[23] G.R. Stewart. *Rev. Mod. Phys.*, **73**.

[24] A.J. Schofield. *Rev. Mod. Phys.*, **40**:95–105, 1999.

[25] C.M.K. Varma, Z. Nussinov, and Wimvan Saarloos. *Phys. Rep.*, **361**:267–295, 2002.

[26] P. Nozières. *Eur. Phys. J. B.*, **6**:447–457, 1998.

[27] E. Miranda, V. Dobrosavljevic, and G. Kotliar. *Physica B*, **230–232**:569–571, 1997.

[28] B. Bernu, D.E. MacLaughlin, and H.G. Lukefahr. *Phys. Rev. Lett.*, **75**:2023–2026, 1995.

[29] J.A. Hertz. *Phys. Rev. B*, **14**:1165–1184, 1976.

[30] A.J. Millis. *Phys. Rev. B*, **48**:7183–7196, 1993.

[31] T. Moriya and T. Takimoto. *J. Phys. Soc. Jpn.*, **64**:960–969, 1995.

[32] G.G. Lonzarich. *Electron.* Cambridge Univ. Press, 1997. Chapter 6.

[33] A. Rosch. *Phys. Rev. B*, **62**:4945–4962, 2000.

[34] H. v. Löhneysen, A. Neubert, T. Pietrus, A. Schröder, O. Stockert, U. Tutsch, M. Loewenhaupt, A. Rosch, and P. Wölfle. *Eur. Phys. J. B*, **5**:447–455, 1998.

[35] A. Schröder, G. Aeppli, R. Coldea, M. Adams, O. Stockert, H. v. Löhneysen, E. Bucher, R. Ramazashvili, and P. Coleman. *Nature*, **407**:351–355, 2000.

[36] O. Trovarelli, C. Geibel, S. Mederle, C. Langhammer, F.M. Grosche, P. Gegenwart, M. Lang, G. Sparn, and F. Steglich. *Phys. Rev. Lett.*, **85**:626–629, 2000.

[37] P. Gegenwart, J. Custers, C. Geibel, K. Neumaier, T. Tayama, K. Tenya, O. Trovarelli, and F. Steglich. *Phys. Rev. Lett.*, **89**:056402–1–4, 2002.

[38] Q. Si, S. Rabello, K. Ingersent, and J.L. Smith. *Nature*, **413**:804–808, 2001.

[39] P. Coleman, C. Pépin, Q. Si, and R. Ramazashvili. *J. Phys.: Condens. Matter*, **13**:R723–R738, 2001.

[40] H. v. Löhneysen, A. Neubert, T. Pietrus, A. Schröder, O. Stockert, U. Tutsch, M. Loewenhaupt, A. Rosch, and P. Wölfle. *Eur. Phys. J. B*, **5**:447–455, 1998.

[41] O. Trovarelli, C. Geibel, C. Langhammer, S. Mederle, P. Gegenwart, F.M. Grosche, M. Lang, G. Sparn, and F. Steglich. *Physica B*, **281–282**:372–373, 2000.

[42] P. Gegenwart, J. Custers, C. Geibel, K. Neumaier, T. Tayama, K. Tenya, O. Trovarelli, and F. Steglich. *Phys. Rev. Lett.*, **89**:056402–1–4, 2002.

[43] R. Bachmann, F.J. Disalvo Jr., T.H. Geballe, R.L. Greene, R.E. Howard, C.N. King, H.C. Kirsch, K.N. Lee, R.E. Schwall, H.U. Thomas, and R.B. Zubeck. *Rev. Sci. Instrum.*, **43**:205, 1972.

[44] J.F. Cochran, C.A. Shiffman, and R.B. Zubeck. *Rev.Sci.Instrum.*, **37**:499, 1966.

[45] P. F. Sullivan and G. Seidel. *Phys. Rev.*, **173**:679, 1968.

[46] R.E. Schwall, R.E. Howard, and G.R. Stewart. *Rev. Sci. Instrum.*, **46**:1054, 1975.

[47] E. Gmelin. *Thermochimica Acta*, **29**:1, 1979.

[48] G.R. Stewart. *Rev. Sci. Instrum.*, **54**:1, 1983.

[49] Y. Kraftmakher. *Phys. Reports*, **356**:1, 2002.

[50] R.A. Fisher, P. Radhakrishna, N.E. Phillips, J.V. Badding, and A.M. Stacy. *Phys. Rev. B*, **52**:13519–13525, 1995.

[51] R. Caspary, P. Hellmann, M. Keller, G. Sparn, C. Wassilew, R. Köhler, C. Geibel, C. Schank, F. Steglich, and N.E. Phillips. *Phys. Rev. Lett.*, **71**:2146–2149, 1993.

[52] P. Hellmann. Darmstadt, 1993. *PhD thesis (unpublished).*

[53] H.J. Schink and H.v. Lohneysen. *Cryogenics*, pages 591–592, 1981.

[54] D.S. Betts. *An introduction to millikelvin technology.* Cambridge University Press, 1989.

[55] H.R. O'Neal and N.E. Phillips. PhD thesis, 1965.

[56] J. Custers, P. Gegenwart, H. Wilhelm, K. Neumaier, Y. Tokiwa, O. Trovarelli, C. Geibel, F. Steglich, C. Pépin, and P. Coleman. *Nature*, **424**:524–527, 2003.

[57] H. Wilhelm, T. Lühmann, T. Rus, and F. Steglich. *Rev. Sci. Instrum.*, **75**:2700–2705, 2004.

[58] W.W. Kim, J.S. Kim, B. Andraka, and G.R. Stewart. *Phys. Rev. B*, **47**:12403, 1993.

[59] I.R. Walker, F.M. Grosche, D.M. Freye, and G.G. Lonzarich. *Physica C*, **282–287**:303–306, 1997.

[60] D. Jaccard, H. Wilhelm, , K. Alami Yadri, and E. Vargoz. *Physica B*, **1–7**:259–261, 1999.

[61] F.M. Grosche, S.R. Julian, N.D. Mathur, and G.G. Lonzarich. *Physica B*, **223–224**:50–52, 1996.

[62] J.S. Kim, D. Hall, K. Heuser, and G.R. Stewart. *Solid State commun.*, **114**:413, 2000.

[63] M.A. Continentino. *Eur. Phys. J. B*, **13**:31–35, 2000.

[64] P. Coleman. *Physica B*, **259–261**:353–358, 1999.

[65] P. Coleman, C. Pépin, Q. Si, and R. Ramazashvili. *J. Phys.: Condens. Matter*, **13**:R723–R738, 2001.

[66] Q. Si, S. Rabello, K. Ingersent, and J.L. Smith. *Nature*, **413**:804–808, 2001.

[67] T. Moriya and K. Ueda. *Adv. Physics*, **49**:555–606, 2000.

[68] M.A. Continentino. *Phys. Rep.*, **239**:179–213, 1994.

[69] Q. Si, S. Rabello, K. Ingersent, and J.L. Smith. *Nature*, **413**:804–808, 2001.

[70] O. Stockert, H. v. Löhneysen, A. Rosch, N. Pyka, and M. Loewenhaupt. *Phys. Rev. Lett.*, **80**:5627–5630, 1998.

[71] R. Küchler. T. U. Dresden, 2005. *PhD thesis* (unpublished).

[72] R. Küchler, N. Oeschler, P. Gegenwart, T. Cichorek, K. Neumaier, O. Tegus, C. Geibel, J.A. Mydosh, F. Steglich, L. Zhu, and Q. Si. *Phys. Rev. Lett.*, **91**:066405–1–4, 2003.

[73] F. Steglich, J. Aarts, C.D. Bredl, W. Lieke, D. Meschede, W. Franz, and H. Schäfer. *Phys. Rev. Lett.*, **43**:1892–1896, 1979.

[74] P. Gegenwart, M. Lohmann, M. Lang, R. Helfrich, C. Langhammer, M. Köppen, C. Geibel, F. Steglich, and W. Assmus. *Physica B*, **572**:230–232, 1997.

[75] H. Kadowaki, B. Fåk, T. Fukuhara, K. Maezawa, K. Nakajima, M. A. Adams, S. Raymond, and J. Flouquet. *Phys. Rev. B*, **68**:140402–140406, 2003.

[76] O. Trovarelli, C. Geibel, S. Mederle, C. Langhammer, F.M. Grosche, P. Gegenwart, M. Lang, G. Sparn, and F. Steglich. *Phys. Rev. Lett.*, **85**:626–629, 2000.

[77] S. Mederle, R. Borth, C. Geibel, F.M. Grosche, G. Sparn, O. Trovarelli, and F. Steglich. *J. Phys.:Condens. Matter*, **14**:10731–10736, 2002.

[78] S. Mederle. PhD thesis, T. U. Dresden (unpublished), 2002.

[79] O. Trovarelli, J. Custers, P. Gegenwart, C. Geibel, P. Hinze, S. Mederle, G. Sparn, and F. Steglich. *Physica B*, **312–313**:401–402, 2002.

[80] T. Moriya and T. Takimoto. *J. Phys. Soc. Jpn.*, **64**:960–969, 1995.

[81] J. Plessel. Univ. of Cologne, 2001, *PhD thesis*, (unpublished).

[82] G.C. Carter, L.H. Bennet, and D.J. Kahan. *Metallic shifts in NMR*, volume **20** of *Progress in Materials Science.* Pergamon Press, Oxford, 1977.

[83] P. Coleman and C. Pépin. *Physica B*, **312–313**:383–389, 2002.

[84] Y. Tokiwa, P. Gegenwart, T. Radu, F. Weickert, G. Sparn, C. Geibel, and F. Steglich. *Phys. Rev. Lett.*, **94**:226402–1–4, 2005.

[85] J. Ferstl. *private communication*, 2004.

[86] Z. Hossain, C. Geibel, F. Weickert, T. Radu, Y. Tokiwa, H. Jeevan, P. Gegenwart, and F. Steglich. **72**:094411–1–4, 2005.

[87] F. Weickert. *private communication*, 2004.

[88] K. D. Schotte, W.A.C. Erkelens, J. Rossat-Mignod, P. Lejay, and J. Flouquet. *Phys. Rev. B*, **38**:4481–4487, 1988.

[89] H.F. Braun, N. Engel, and E. Parthé. *Phys. Rev. B*, **28**:1389–2149, 1983.

[90] Y. Tokiwa. *private communication*.

[91] J. Custers, P. Gegenwart, H. Wilhelm, K. Neumaier, Y. Tokiwa, O. Trovarelli, C. Geibel, F. Steglich, C. Pépin, and P. Coleman. *Nature*, **424**:524–527, 2003.

[92] J. Lawrence. *Phys. Rev. B*, **20**:3770–3782, 1979.

[93] R.A. Elenbaas, C.J. Schinkel, and C.J.M. v. Deudekom. *J. Magn. Magn. Mater.*, **15–18**:970–981, 1980.

[94] N.D. Mathur, F.M. Grosche, S.R. Julian, I.R. Walker, D.M. Freye, R.K.W. Haselwimmer, and G.G. Lonzarich. *Nature*, **394**:39–43, 1998.

[95] J.M. Lawrence and S.M. Shapiro. *Phys. Rev. B*, **22**:4379–4388, 1980.

[96] I.R. Harris and G.V. Raynor. *J. Less–Common. Met.*, **9**:7–19, 1965.

[97] A. Benoit, J.X. Boucherle, P. Convert, J. Flouquet, J. Pellau, and J. Schweizer. *Solid State Commun.*, **34**:293–295, 1980.

[98] J.G. Sereni. *J. Alloys and Compounds*, **207–208**:229–236, 1994.

[99] J.G. Sereni. *J. Phys. Soc. Jpn*, **67**:1767, 1998.

[100] P. Pedrazzini, M. Gómez Berisso, N. Caroca–Canales, M. Deppe, C. Geibel, and J.G. Sereni. *Eur. Phys. J. B*, **38**:445, 2004.

[101] J.G. Sereni. *Physica B*, **206–207**:246–248, 1995.

[102] P. Pedrazzini, M. Gómez Berisso, N. Caroca–Canales, M. Deppe, C. Geibel, and J.G. Sereni. *Physica B*, **312–313**:406–407, 2002.

[103] J. Custers. T. U. Dresden, 2004. *PhD thesis*, unpublished.

[104] G. Knebel, D. Braithwaite, P.C. Canfield, G. Lapertot, and J. Flouquet. *Phys. Rev. B*, **65**:024425–1–10, 2001.

[105] N.D. Mathur, F.M. Grosche, S.R. Julian, I.R. Walker, D.M. Freye, R.K.W. Haselwimmer, and G.G. Lonzarich. *Nature*, **394**:39–43, 1998.

[106] P. Pedrazzini, M. Gómez Berisso, J.G. Sereni, N. Caroca–Canales, M. Deppe, and C. Geibel. *Acta Physica Polonica B*, **34**:363–366, 2003.

[107] J. Custers, T. Cichorek, P. Gegenwart, N. Caroca–Canales, O. Stockert, C. Geibel, F. Steglich, P. Pedrazzini, and J.G. Sereni. *Acta Phys. Pol. B*, **34**:379–382, 2003.

[108] A. Rosch, A. Schröder, O. Stockert, and H. v. Löhneysen. *Phys. Rev. Lett.*, **79**:159–162, 1997.

[109] L. Zhu, M. Garst, A. Rosch, and Q. Si. *Phys. Rev. Lett.*, **91**:066404–1–4, 2003.

[110] T. Rus, H. Wilhelm, O. Stockert, T. Lühmann, N. Caroca-Canalesa, J.G. Sereni, C. Geibel, and F. Steglich. *Physica B*, **359–361**:62–64, 2005.

[111] G. Knopp and A. Loidl. *J. Magn. Magn. Mat.*, **74**:341–346, 1988.

[112] R. Coldea, D.A. Tennant, R.A. Cowley, D.F McMorrow, and Z. Tylczynski. *J. Phys. Condens. Matter*, **8**:7473–7491, 1996.

[113] Ae Ran Lim, Jae Kap Jung, and Se Young Jeong. *Phys. Rev.B*, **65**:134423, 2002.

[114] H. Yoshizawa and G. Shirane. *Phys. Rev. B*, **28**:3904–3908, 1983.

[115] B.N. Figgis, P.A. Reynolds, and A.H. White. *J. Chem. Soc. Dalton Trans.*, **7**:1737–1745, 1987.

[116] R. Coldea, D.A. Tennant, K. Habicht, P. Smeibidl, C. Wolters, and Z. Tylczynski. *Phys. Rev. Lett.*, **88**:137203, 2002.

[117] R. Coldea, D.A. Tennant, and Z. Tylczynski. *Phys. Rev. B*, **68**:134424, 2003.

[118] R. Coldea, D.A. Tennant, R.A. Cowley, D.F McMorrow, B. Dorner, and Z. Tylczynski. *Phys. Rev. Lett.*, **79**:151–154, 1997.

[119] R. Coldea, D.A. Tennant, A.M. Tsvelik, and Z. Tylczynski. *Phys. Rev. Lett.*, **86**:1335–1338, 2001.

[120] P.W. Anderson. *Mater. Res. Bull*, **8**:153–158, 1973.

[121] A. Klümper and D.C. Johnston. *Phys. Rev. Lett.*, **84**:4701–4704, 2000.

[122] R. Coldea. *private communication*, 2003.

[123] W. Zheng. *private communication.*

[124] T. Radu, H. Wilhelm, V. Yushankhai, D. Kovrizhin, R. Coldea, Z. Tylczynski, T. Lühmann, and F. Steglich. *Phys. Rev. Lett.*, **95**:127202, 2005.

[125] M.Y. Veillette, J.T. Chalker, and R. Coldea. *cond–mat/0501347*, 2005.

[126] S. Bailleul, J. Hölsä, and P. Porscher. *Eur. J. Solid State Inorg. Chem.*, **31**:431–447, 1994.

[127] A. Abrikosov, L. Gorkov, and T. Dzyaloshinskii. *Methods of quantum field theory in statistical physics.* New York, Dover Publ., 1975.

[128] O. Nohadani, S. Wessel, B. Normand, and S. Haas. *Phys. Rev. B*, **69**:220402–1–4, 2004.

[129] J.N. McElearney, S. Merchant, G.E. Shankle, and R.L. Carlin. *J. Chem. Physics*, **66**:450–458, 1975.

[130] H.A Algra, L.J. de Jongh, H.W.J Blöte, and W.J. Huiskamp. *Physica B. Magn. Magn. Mater.*, **82**:239–246, 1976.

[131] S. Katsura. *Phys. Rev.*, **129**:1508–1518, 1963.

[132] J. Kurmann, H. Thomas, and G. Müller. *Physica A*, **112**:235–255, 1982.

[133] D.V. Dmitriev and V.Ya. Krivnov. *Phys. Rev. B*, **70**:144414–1–10, 2004.

[134] D. Allen, P. Azaria, and P. Lecheminant. *J. Phys.A Mathematical and General*, **34**:L305–L310, 2001.